Tropical Cyclone Risk Assessment Using Statistical Models

Emmi Yonekura

Submitted in partial fulfillment of the
requirements for the degree of
Doctor of Philosophy
in the Graduate School of Arts and Sciences

COLUMBIA UNIVERSITY

2013

ABSTRACT

Tropical Cyclone Risk Assessment Using Statistical Models

Emmi Yonekura

Tropical cyclones (TC) in the western North Pacific (WNP) pose a serious threat to the coastal regions of Eastern Asia when they make landfall. The limited amount of observational data and the high computational cost of running TC-permitting dynamical models indicate a need for statistical models that can simulate large ensembles of TCs in order to cover the full range of possible activity that results from a given climate change. I construct and apply a statistical track model from the 1945-2007 observed "best tracks" in the IBTrACS database for the WNP. The lifecycle components—genesis, track propagation, and death—of each simulated track is determined stochastically based on the statistics of historical occurrences. The length scale that dictates what historical data to consider as "local" for each lifecycle component is calculated objectively through optimization. Overall, I demonstrate how a statistical model can be used as a tool to translate climate-induced changes in TC activity into implications for risk.

In contrast to other studies, I show that the El Niño/Southern Oscillation (ENSO) has an effect on track propagation separate from the genesis effect. The ENSO effect on genesis results in higher landfall rates during La Niña years due to the shift in genesis location to the northeast. The effect on tracks is more geographically and seasonally varied due to local changes in the mid-level winds. I use local regression techniques to capture the relationship between ENSO, cyclogenesis, and track propagation. Stationary climate simulations are run for extreme ENSO states in order to better understand changes in TC activity and their implication for regional landfall. Additionally, Several diagnostics are performed on model realizations of the historical

period, confirming the model's ability to capture the geographical distribution and interannual variability of observed TCs.

Lastly, as a step to connect synthetic TC track simulations to economic damage risk assessment, I use a Damage Index and total damage data for U.S. landfalling hurricanes and fit generalized Pareto distributions (GPD) to them. The Damage Index uniquely separates out the effects of the physical damage capacity of a TC and the local economic vulnerability of a coastal region. GPD fits are also performed using covariates in the scale parameter, where bathymetric slope and landfall intensity are found to be useful covariates for the Damage Index. Using the Damage Index with covariates model, two examples are shown of assessing damage risk for different climates. The first takes landfall data input from a statistical-deterministic TC model downscaled from GFDL and ECHAM model current and future climates. The second takes landfall data from a fully statistical track model with different values of relative sea surface temperature given as a statistical predictor.

TABLE OF CONTENTS

LIST OF FIGURES

LIST OF TABLES

ACKNOWLEDGMENTS

There are many people I would like to acknowledge for helping and supporting me on the way to completing my dissertation over the last five years. First, I would like to thank Tim Hall for all the advice, support, and patient teaching he has offered as my thesis adviser from the start. I would also like to thank Tony Del Genio, Suzana Camargo, and Adam Sobel for offering comments on this work as well as general advice for reaching my goals. I am also grateful for comments on this work from Upmanu Lall, who also served on my dissertation committee. For their fellowship and support, I thank my colleagues and Columbia classmates Elizabeth Pierce, Alison Hartman, Meg Reitz, Anna Foster, Kat Allen, Christina Karamperidou, Colin Kelley, Jason Jweda, Rafael Almeida, Marc Vankeuren, Daniel Ruiz-Carrascal, Sonali Shukla, Jing Li, Jen Alltop Aminzade, Kirk Knobelspiesse, Jimmy Booth, Xiaojun Yuan, and Doug Martinsen.

The impetus for the fourth chapter of this thesis came from a wonderful workshop, the National Center for Atmospheric Research (NCAR) 2011 Advanced Study Program (ASP) Summer Colloquium on the Statistical Assessment of Extreme Weather Phenomena under Climate Change. For their great guidance, I thank Rick Katz, Eric Gilleland, and Asuka Suzuki-Parker. For their hard work, honey badger-esque tenacity, and camaraderie, I thank my collaborators, Christina Karamperidou, Dan Chavas, Katy Serafin, and Nick Cavanaugh.

A huge thanks goes to my parents and sisters, Ai-ris, Kiyomi, and Satori, for their continued support and encouragement. And finally, thanks to my friends, Joe Hall, Tiffany Kwan, Carey Chen, Ama Awotwi, Shirley Matthews, Mai Huynh, Vanna Wong, Angie Cheng, Mimi Wang, Anna Wong, Meghan Jackson, Shashank Sundareshan, Priya Sundareshan, and Andrew Allison, for helping me keep a happy, balanced life.

to Ai-ris, my sister

Chapter 1:

Introduction and Background

The focus of this dissertation is to make risk assessments for tropical cyclones with the specific aim of evaluating how risk changes with climate influences. This topic requires knowledge about tropical cyclones, the Earth's climate system, risk assessment, and statistical modeling. In this chapter, I provide a background on each of these areas. Therein, I also present a literature review of the specific tropical cyclone-climate interactions that this thesis examines as well as a review of statistical models that have been used in risk assessment. The chapter closes with an outline of the objectives of each chapter of this dissertation.

1.1 Tropical cyclones

Tropical cyclones (TC) are known to humans as some of the most damaging storms to affect coastal areas and are associated with some of the world's worst natural disasters in history. TCs are also known as hurricanes in the North Atlantic, typhoons in the western North Pacific, and cyclones in Australia. TCs have a characteristic cyclonic spiral structure and are on the order of 1000km (synoptic scale) in size. They typically form from low surface pressure disturbances over warm tropical oceans, where humid air is drawn inward at the air-sea boundary, gaining energy from sensible and latent heat. In an unstable atmosphere, the moist air rises, forming a system of deep convection up to the tropopause. The basic requirements for TC formation and intensification are warm sea surface temperature (above 26.5°C), high relative humidity air, atmospheric instability, low vertical wind shear (large differences in wind velocities at different levels in the atmosphere impede deep convection), the Coriolis force, and an initial low pressure disturbance (Gray 1968).

The strongest deep convection and often the most powerful winds can be found in the eyewall, which is nearest to the center, or eye. The intensity of a TC is measured either by the low sea level pressure at the center or the maximum sustained winds in the eyewall. In the big picture of

the Earth's climate system, TCs play a crucial role in transporting heat from the tropics toward the poles.

After formation, TCs move across their respective oceans with the background steering winds that are typically westward in the tropics and eastward in the mid-latitudes. TCs are also steered right in the Northern Hemisphere and left in the Southern Hemisphere by the Coriolis force and beta drift, a result of the Coriolis force changing with latitude (Elsberry 1995). Given this, TC tracks are prone to intersect with several coastlines around the world (landfall), including the Gulf of Mexico, the Eastern U.S. coast, and the East Asian coast. Once TCs make landfall or reach cooler waters in higher latitudes, they lose their energy source and dissipate.

a. TCs in the western North Pacific

Relative to other ocean basins, the western North Pacific (WNP) is large and warm. TCs in the WNP, due to their environment have a few differences in comparison to the other basins. WNP TCs have longer average lifetimes and are able to traverse closer to the equator. They reach the highest intensities and occur the most frequently due to favorable conditions for formation and intensification. Warm sea surface temperatures (SST) of the WNP provide energy to storms, and the wide basin allows for storms to travel longer over warm ocean waters before recurving northward to cooler waters or hitting land and dissipating. Also, seasonally, the WNP stays relatively warm, so TCs may occur any month of the year, though peak season is June through November. The peak season is mostly due to the seasonally warmed upper ocean, which supplies energy for TC formation and intensification. (Neumann 1993)

The main development region for WNP TCs is less well defined than in the North Atlantic, but a rough definition is 5° to 15°N and 130° to 180°E (Emanuel 2005). Similar to

other basins, the mean track pattern is westward in the tropical low latitudes. Some continue straight into the East Asian coast, some curve northward, and some eventually travel eastward in subtropical midlatitudes. The most affected coastal regions that will be considered here are on East Asia. We cut our domain off at 100˚E in order to distinguish from the South Asian TCs. The East Asian regions we consider here are Vietnam, China, the Korean Peninsula, Kamchatka, Japan, the Philippines, Malaysia, and Cambodia, which include many densely populated cities with high vulnerability.

b. TCs in the North Atlantic

TCs in the North Atlantic (NA) are of large interest in the United States because they make landfall on the East and Gulf Coasts. Though NA TCs are the same natural phenomenon, there are some differences in their behavior, as the two ocean basins are not identical. In the NA, the initial disturbance, or low pressure system, that leads to a TC genesis often results from African Easterly Waves, though they also originate from other equatorial waves. The main development region is at 10°N to 20°N and 20°W to 85°W (Emanuel 2005). Track shapes are similar to those described in the WNP except the NA is less wide, resulting in shorter life spans. Further, the NA has cooler SSTs, which means that TCs do not normally reach intensities as high as those observed in the WNP and the season is more confined to summer and fall months (Neumann 1993).

1.2 Tropical cyclones and Climate

One of the most publicized areas of TC research is the relationship of TC activity to natural climate variability and anthropogenic climate change, often referred to as global warming. This thesis will examine TC hazard as a function of both natural climate variability and anthropogenic

climate trends. Chapters 2 and 3 will focus on natural climate variability due to the El Niño/Southern Oscillation (ENSO), and Chapter 4 will address the hazard impact of anthropogenic climate change, as projected by GCMs.

a. ENSO

The El Niño/Southern Oscillation is a 3-7 year period climate oscillation that is characterized by a warming of the SST anomalies in the eastern equatorial Pacific as well as a change in the East-West pressure difference across the Pacific (Sarachik and Cane 2010). There are two main phases of ENSO, El Niño and La Niña, as well as a neutral state in between. During an El Niño event, the region of surface air convergence shifts eastward, bringing large convective systems with it. The thermocline (ocean layer of rapid temperature decrease with depth below the top mixed layer) becomes deeper in the eastern Pacific and the wind anomalies reverse eastward. The opposite occurs for a La Niña. There are several indices that measure the strength and phase of ENSO, either by measuring the pressure difference or the SST anomalies of regions in the equatorial Pacific. Recent work has started to characterize the different patterns of ENSO SST anomalies, eastern equatorial and central Pacific warming (Ashok et al. 2007), but the focus of this thesis is on the traditional eastern equatorial Pacific warming characterized by the Niño3.4 region (5°N-5°S, 120-170°W) index of SST anomalies (Barnston et al. 1997).

b. Relationship of ENSO and TCs in the WNP

The first part of this thesis focuses on the influence of ENSO on TCs in the WNP. It is well established that there is a strong relationship between ENSO and TC activity in the WNP, and here I provide a review of the previous literature documenting it.

The predominant location of TC formation, or genesis, in the WNP shifts depending on the phase of ENSO. The main formation region tends to be in the southeastern part of the WNP ocean basin during an El Niño year, and there is a northwestern shift during a La Niña year toward the South China Sea. This is explained by changes in relative humidity and low-level vorticity, which favor genesis, that shift eastward during the El Niño phase of ENSO (Camargo et al. 2007a). Dong (1988) also suggests that changes in the Walker Circulation with ENSO cause the genesis region shift. In a more recent study, Kim et al. (2011) show that an eastern Pacific warming is accompanied by strong westerly wind shear in the northwest extension of the monsoon trough, and weaker shear over the central Pacific, which causes the changes in TC activity. The frequency, or number of TCs per year, has been found to be unaffected by ENSO state, though Lander (1994) found that for extreme ENSO events, there is a marginal difference.

The track shape and lifetime duration of TCs changes with ENSO state in part due to the changes in genesis. For instance, during an El Niño year, TCs form farther southeast and thus can travel westward over more open ocean before making landfall and dissipating. With more time before making landfall, these TCs are more affected by beta drift that steers them to the right, resulting in a re-curving or northward-pointing shape. When the TCs form closer to the East Asian coastline in a La Niña year, the TCs tend to move straight westward and have shorter life spans (Elsner and Liu 2003; Camargo et al. 2007b). Aside from the genesis region shift explaining these effects, changes in the mid-level steering winds with ENSO may also explain changes in track shapes and life spans. Whether there are track and life span changes that are not due to genesis changes is a question that will be addressed in this thesis.

An added implication to TCs that have more time to travel across the warm tropical Pacific is that they also have more opportunity to intensify. Chan and Liu (2004) used various

measures of TC activity in the WNP (including intensity) and found little relationship between TCs and local SST warming. They did find, however, a strong relationship showing higher accumulated cyclone energy (ACE, the sum of the squares of maximum wind speed at each time step) during El Niño phases. In a further investigation of the ENSO effect on WNP TC lifetime and intensity, Camargo and Sobel (2005) used to determine that there is a shift toward more intense typhoons (higher ACE per year and higher ACE per storm) with El Niño. There is also a definite tendency for longer TC lifetimes during El Niño, due to the shift in genesis location further southeast.

c. TCs and Climate Change

The fourth chapter of this thesis shifts focus to the climate change due to anthropogenic greenhouse gases in the last few decades that is projected to escalate into the next century. Many studies have been conducted in attempt to understand the behavior of TCs with climate change with much uncertainty in results and a few areas of agreement. In a recent assessment of the state of work on the effect of global warming on TCs, Knutson et al. (2010) state that most modeling and theoretical studies agree that the intensity of TCs will increase and the frequency will decrease on a globally averaged basis. However, there is still much uncertainty in these projections and even more differences appear when looking at specific basins of TC activity. When it then comes to connecting these changes to landfall risk, there have been conflicting results in the WNP. Weinkle et al. (2012) state that climate change will bring no significant change to landfall in any basin. In contrast, given the expected increase in intense TCs in combination with increases in coastal vulnerability, it is projected that economic damage and mortality due to TC landfall will rise (Mendelsohn et al. 2012; Peduzzi et al. 2012).

1.3 Risk Assessment

TCs throughout history have caused tremendous amounts of damage when they make landfall on a populated coastal region. One of the best known recent landfalls was Hurricane Katrina on New Orleans on August 29, 2005, costing approximately $108 billion in damages in all affected areas, the highest in US history, and causing 1833 fatalities (Knabb et al. 2006). A TC landfall is associated with several potential hazards. The most common hazards include flooding, wind damage, and storm surge (Lin et al. 2010; Iman et al. 2005; Rogers et al. 2009). In turn, these hazards can have a great economic effect on areas by stopping business, damaging facilities, destroying property, and causing loss of lives of people and animals.

One step toward hazard mitigation for TC landfall is to perform a risk assessment. This involves looking at a situation and deciding how likely it is that a hazard will occur. The other part of a risk assessment is to examine the vulnerability of a region of interest, meaning quantifying what exactly may be lost in the event of a hazard occurring. The commonly used equation is: Risk = Hazard * Vulnerability. Risk assessments can then be used to inform those vulnerable and parties responsible for dealing with the hazard fallout. In TC landfall risk assessment, this could be a resident of coastal property and an insurance company. An important question for regions where, historically, TC landfall has been rare, is whether the same behavior can be expected in the near and long-term future. For instance, will TC landfall risk increase in a warmer climate? Is a lack of recent landfalls simple luck, which cannot be expected to last?

A natural hazard does not necessarily have to become a natural disaster with careful risk management. High vulnerability can arise from having regions of dense population, lack of mitigation efforts, or both. The hope is that using risk assessments, both individuals and larger organizations can make informed decisions about mitigation plans.

1.4 Statistical Analysis and Modeling of Landfall Data and Track Modeling

One way to study TC landfalls is to look at the recorded data for landfalls over a region, usually spanning back 50-150 years. However, landfall risk varies greatly with region. If it is desired to assess risk at high spatial resolution, or for regions of historically low activity, this approach suffers from data limitations. There are a few ways around this problem. Elsner et al. (2006) performed Bayesian regression on the U.S. landfall record (over 150 years) using different climatological predictors to form a predictive model. The advantage of using regression is that it does not require the data to be broken down into smaller subsets to study behavior changes. Extreme value theory has also been used, which makes use of sparse data, or extreme events, to create a probability distribution. Examples of this are Katz (2002) and Jagger et al. (2008; 2010), where generalized Pareto distributions (a type of extreme value distribution) are fit to U.S. landfalling hurricane data using large-scale climate indices as covariates. Another solution is to try to uncover more data. Several paleotempestology studies (e.g., Liu and Fearn 2000; Donnelly et al. 2004; Donnelly and Woodruff 2007) have been performed to extend the landfall record thousands of years using overwash sand in coastal lakes and marshes as a proxy for an intense hurricane landfall. For a landfall analysis on the Guangdong Province in China, the record was extended by hundreds of years using government records (Chan and Shi 2000). From studies of landfall data, return period estimates can be made of regional landfall.

Many landfall data studies still suffer from data sparseness. An alternative solution to the problem of sparse landfall data is to use a model to simulate a large number of synthetic TCs to

calculate the risk. There are a wide variety of models that are used for these purposes. Dynamical models use the physical understanding of TCs in a specified environment and climate to simulate storms. However, most dynamical models do not have high enough resolution to accurately depict TCs (Meehl et al. 2007), and they are still very computationally expensive to run if the goal is to create a large ensemble of thousands of years. This provides motivations for using models that are fully statistical and based on the historical observations.

There has been a lot of work done in statistical TC track modeling that use similar methods. James and Mason (2005) model TC central pressure, latitude, and longitude location as an autoregressive process, meaning the next simulated step depends on the previous steps. Similar studies (Vickery et al. 2000; Graf et al. 2009; Yin et al. 2009; Hall and Jewson 2007) take this further and use additional storm characteristics, location, and climatological variables as predictors for stochastic simulations of TC trajectory and intensity based on the known physical relationships and behaviors of TCs in theory and observations. Along each track step, there is a calculation that looks like the following:

$$Y_{i+1} = b_0 Y_i + b_1 X_1 + b_2 X_2 + \ldots + \varepsilon,$$

where Y_{i+1} is the next step (i+1) in latitude, longitude, or intensity, Y_i is the previous value of that quantity, each b is a previously calculated regression coefficient usually specific to the storm location, the X's are predictor variables such as SST or ENSO, and ε is an error term.

An alternative method that has been used is to perform Monte Carlo simulations along tracks, or at a specific landfall site, where the local observations of track propagation step or intensity, form a PDF that is sampled to determine the next step (Chu and Wang 1998; Rumpf et al. 2007). The advantage of this is that it will closely follow observed behavior, though this can also act to constrain model capabilities.

A popular method for simulating TC genesis is to use Poisson regression, because genesis is a discrete count process. Basin-wide Poisson regression using large-scale climate variables or local environmental conditions as predictors to simulate annual TC counts has been widely practiced (Sabbatelli and Mann 2007; Chu and Zhao 2007; Kozar et al. 2012). Using the regression results, genesis counts can be predicted, given predictor values. To simulate genesis location and time, local Poisson regression is used, where the regression of observed genesis counts on predictors is done over specified grid boxes in space and time (McDonnell and Holbrook 2004).

1.5 Dissertation Objectives

There is a great practical importance to understand the risk that TCs pose to coastal regions. While a vast quantity of research has been done to determine the relationship between basic TC behavior in different background climate states, there is a disconnect between that and the implications for landfall risk. This thesis aims to close this gap by constructing a TC track model and exploring new methods to predict damage from TC landfall. This thesis is organized in the following way:

Chapter 1: Introduction to the topic of tropical cyclones and risk assessment, including a review of the current literature.

Chapter 2: Construction of a statistical model that realistically simulates TC behavior in the WNP and captures the effect of ENSO in the genesis component.

Chapter 3: Examine whether the ENSO effect on tracks has a significant effect on TC risk aside from and that due to the genesis effect. Also, add the complexity of seasonality in the genesis and track components to improve the model.

Chapter 4: Analyze economic damage data and its relationship to the physical characteristics of individual storms to create a way to predict damage from statistical track model output for different climates.

Chapter 5: Discusses the results of this thesis as well as future directions that this work will take.

The statistical track model for the WNP (Chapters 2 and 3) can be used to make a climatological assessment of landfall risk on a regional scale, i.e. it can give a regional risk estimate for the next year given that the climate will likely be similar to the past sixty years. It can also give a risk assessment for different values of its statistical predictors, such as ENSO. Combining its information with a model to predict ENSO states, regional landfall risk can be inferred. Statistical models of this type are most commonly used in the insurance industry, where risk assessments are used to set insurance premiums for the next year.

In approaching the construction and use of the model from an academic perspective, we have extended the normal use of the model by using it to study various aspects of the TC life and the effects that different large-scale climate predictors have on them. These methods improve upon observational studies and dynamical model studies because it makes the most out of limited data and provides a fairly straightforward tool for examining the effects of changes in its predictors.

Also important to note is that the model is not intended to make day-to-day, or operational, predictions of currently existing TCs. The model output is still in the form of 6-hourly track locations, however it is really the behavior of the large ensemble of simulations that is considered rather than individual tracks. Further, a climatological risk assessment model uses climatological variables as predictors because hourly, high-resolution data for the environment of

each TC in the past six decades is not available for building the model. Even if it were available, many of those quantities are not predictable a year in advance as input for a risk projection. We choose our predictors based on what is most likely to be available to use, such as large-scale climate variables and climatological variables that behave in relatively consistent cycles.

Regarding the work in Chapter 4, the generalized Pareto distribution of economic damage and use of a Damage Index improves upon previous work by deconvolving the physical damage potential of individual TCs and the large variability in economic value (vulnerability) along coastlines in the path of TCs. This has never been done before, and it is hoped that this could be used to assess future climate damage risk as well as how landfall risk changes with physical climate changes that affect TC behavior. This will help connect the work that has been done relating TC behavior and landfall to different climates to quantities that are important to coastal inhabitants and policymakers.

The three main body chapters (2-4) are based on two published papers—Yonekura and Hall (2011) in *Journal of Applied Meteorology and Climatology* (Chapter 2) and Chavas et al. (2012) in *Natural Hazards Review* (Chapter 4)—and a submitted paper, Yonekura and Hall (2012) for Chapter 3. Because of the chapter origins as peer-reviewed papers, they each can be read as stand-alone documents. However, Chapter 3 describes an extension of the work of Chapter 2, and so it is the most natural to read them in order.

References

Ashok, K., S. K. Behera, S. A. Rao, H. Weng, and T. Yamagata, 2007: El Niño Modoki and its possible teleconnection. *J. Geophys. Res.*, **112**, C11007.

Barnston, A. G., M. Chelliah, and S. B. Goldenberg, 1997: Documentation of a highly ENSO-related SST region in the equatorial Pacific. *Atmos.-Ocean*, **35**, 367-383.

Camargo, S.J. and A.H. Sobel, 2005: Western North Pacific tropical cyclone intensity and ENSO. *J. Climate,* **18**, 2996-3006.

Camargo, S.J., K.A. Emanuel and A.H. Sobel, 2007a: Use of a genesis potential index to diagnose ENSO effects on tropical cyclone genesis. *J. Climate*, **20**, 4819-4834.

Camargo, S.J., A.W. Robertson, S.J. Gaffney, P. Smyth, and M. Ghil, 2007b: Cluster analysis of typhoon tracks. Part II: Large-scale circulation and ENSO. *J. Climate,* **20,** 3654–3676.

Chan, J.C.L., 2005: Interannual and interdecadal variations of tropical cyclone activity over the western North Pacific. *Meteor. Atmos. Phys.*, **89**, 143-152.

Chan, J.C.L. and J. Shi, 2000: Frequency of typhoon landfall over Guangdong Province of China during the period 1470-1931. *Int. J. Climatology*, **20**, 183-190.

Chan, J.C.L. and K.S. Liu, 2004: Global warming and western North Pacific typhoon activity from an observational perspective. *J. Climate*, **17**, 4590-4602.

Chu, P., and J. Wang, 1998: Modeling return periods of tropical cyclone intensities in the vicinity of Hawaii. *J. Appl. Meteor.,* **39**, 951-960.

Chu, P.-S., and X. Zhao, 2007: A Bayesian Regression Approach for Predicting Seasonal Tropical Cyclone Activity over the Central North Pacific. *J. Climate*, **20**, 4002–4013.

Dong, K., 1988: El Niño and tropical cyclone frequency in the Australian region and the North-western Pacific. *Aust. Meteor. Mag.,* **36**, 219–255.

Donnelly, J.P., J.D. Woodruff, 2007: Intense hurricane activity over the past 5,000 years controlled by El Niño and the West African Monsoon. *Nature*, **447**, 465–468.

Donnelly, J.P., J. Butler, S. Roll, M. Wengren, T. Webb, III, 2004: A backbarrier overwash record of intense storms from Brigantine, New Jersey. *Marine Geology*, **210**, 107–121.

Elsberry, R. L., 1995: "Tropical cyclone motion." *Global Perspectives on Tropical Cyclones*, R. L. Elsberry (ed.). World Meteorological Organization, Geneva, Switzerland, Report No. TCP-38.

Elsner, J.B. and K.B. Liu, 2003: Examining the ENSO-Typhoon Hypothesis. *Climate Research*, **25**, 43-54.

Elsner, J.B., R.J. Murnane, and T.H. Jagger, 2006: Forecasting U.S. hurricanes 6 months in advance. *Geophys. Res. Lett.*, **33**, L10704.

Emanuel, K., 2005: Increasing destructiveness of tropical cyclones over the past 30 years. *Nature,* **436,** 686–688.

Graf, M., K. Nishijima, and M. H. Faber, 2009: A probabilistic typhoon model for the Northwest Pacific region. Proc. The 7th Asian-Pacific Conf. on Wind Engineering, Taipei, Taiwan, International Assoc. for Wind Eng., M2-B.

Gray, W.M., 1968: A global view of the origin of tropical disturbances and storms. *Mon. Wea. Rev.*, **96**, 669-700.

Hall, T.M., and S. Jewson, 2007: Statistical modeling of North Atlantic tropical cyclone tracks. *Tellus*, **59A**, 486-498.

Iman, R. L., M. E. Johnson, and C. C. Watson, 2005: Sensitivity analysis for computer model projections of hurricane losses. *Risk Analysis*, **25(5)**, 1277-1297.

Jagger, T., J. Elsner, and R. Burch, 2010: Climate and solar signals in property damage losses from hurricanes affecting the United States. *Natural Hazards*, **58(1)**, 541-557.

Jagger, T., J. Elsner, and M. Saunders, 2008: Forecasting U.S. insured hurricane losses. Climate Extremes and Society, H. Diaz and R. Murnane, eds., Cambridge University Press,189-208.

James, M.K. and L.B. Mason, 2005: Synthetic tropical cyclone database. *J. Waterway, Port, and Ocean Eng.*, **131(4)**, 181-192.

Katz, R. W., 2002: Stochastic modeling of hurricane damage. *J. Appl. Meteor.*, **41(7)**, 754-762.

Kim, H.-M., P. J. Webster, and J. A. Curry, 2011: Modulation of North Pacific Tropical Cyclone Activity by Three Phases of ENSO. *J. Climate*, **24**, 1839–1849.

Knabb, R. D., J. R. Rhome, and D. P. Brown, 2011: "Tropical cyclone report: Hurricane Katrina: 23-30 August 2005." *National Hurricane Center.* http://www.nhc.gov/pdf/TCR-AL122005_Katrina.pdf. Accessed September 30, 2012.

Knutson,T.R., J. L. McBride, J. Chan, K. Emanuel, G. Holland, C. Landsea, I. Held, J. P. Kossin, A. K. Srivastava, and M. Sugi, 2010: Tropical cyclones and climate change. *Nature Geoscience*, **3**, 157-163.

Kozar, M. E., M. E. Mann, S. J. Camargo, J. P. Kossin, and J. L. Evans, 2012: Stratified statistical models of North Atlantic basin-wide and regional tropical cyclone counts. *J. Geophys. Res.*, **117**, D18103.

Lander, M. A., 1994: An Exploratory Analysis of the Relationship between Tropical Storm Formation in the Western North Pacific and ENSO. *Mon. Wea. Rev.*, **122**, 636–651.

Lin, N. E., E. Vanmarcke, and S. C. Yau, 2010: Windborne debris risk analysis: Part II. Application in structural vulnerability modeling. *Wind and Structures*, **13**, 207-220.

Liu, K.-b., and M. L. Fearn, 2000: Reconstruction of prehistoric landfall frequencies of catastrophic hurricanes in NW Florida from lake sediment records. *Quaternary Research*, **54**, 238–245.

McDonnell, K. A., and N. J. Holbrook, 2004: A Poisson regression model of tropical cyclogenesis for the Australian-southwest Pacific Ocean region. *Weather and Forecasting*, **19(2)**, 440-455.

Meehl, G.A. et al., 2007: Global Climate Projections, in *Climate Change 2007: The Physical Science Basis. Contribution of Working Group I to the Fourth Assessment Report of the Intergovernmental Panel on Climate Change*, edited by Solomon, S., D. Qin, M. Manning, Z. Chen, M. Marquis, K.B. Averyt, M. Tignor and H.L. Miller. Cambridge University Press, Cambridge, United Kingdom and New York, NY, USA.

Mendelsohn, R., K. Emanuel, S. Chonabayashi, and L. Bakkensen, 2012: The impact of climate change on global tropical cyclone damage. *Nature Climate Change*, **2**, 205-209.

Neumann, C.J., 1993: "Global Overview" - Chapter 1" Global Guide to Tropical Cyclone Forecasting, WMO/TC-No. 560, Report No. TCP-31, World Meteorological Organization; Geneva, Switzerland.

Peduzzi, P., B. Chatenou, H. Dao, A. De Bono, C. Herold, J. Kossin, F. Mouton, and O. Nordbeck, 2012: Global trends in tropical cyclone risk. *Nature Climate Change*, **2**, 289-294.

Rumpf, J., H. Weindl, P. Höppe, P., E. Rauch, and V. Schmidt, 2007: Stochastic modeling of tropical cyclone tracks. *Math. Meth. Oper. Res.,* **66(3)**, 475-490.

Rogers, R., F. D. Marksand, and T. Marchok, 2009: Tropical cyclone rainfall. *Encyclopedia of Hydrological Sciences.*

Sabbatelli, T.A. and M.E. Mann, 2007: The influence of climate state variables on Atlantic Tropical Cyclone occurrence rates. *J. Geophys. Res.,* **112**, D17114.

Sarachik, E. S. and M. A. Cane, 2010: The El Niño-Southern Oscillation Phenomenon. Cambridge University Press, ISBN 978-0-521-84786-5

Vickery, P.J., P.F. Skerlj, and L.A. Twisdale, 2000: Simulation of hurricane risk in the US using an empirical track model. *J. Structural Eng.,* **126**, 12222-1237.

Wang, B. and J.C.L. Chan, 2002: How strong ENSO events affect tropical storm activity over the western North Pacific. *J. Climate*, **15**, 1643-1658.

Weinkle, J., R. Maue, and R. Pielke, 2012: Historical Global Tropical Cyclone Landfalls. *J. Climate*, **25**, 4729–4735.

Yin, J., M. B. Welch, H. Yashiro, and M. Shinohara, 2009: Basinwide typhoon risk modeling and simulation for western North Pacific basin. *Proc. The 7th Asian-Pacific Conf. on Wind Engineering,* Taipei, Taiwan, International Assoc. for Wind Eng., M2-B.

Yonekura, E. and T.M. Hall, 2011: A statistical model of tropical cyclone tracks in the western North Pacific with ENSO-dependent cyclogenesis. *J*. *Appl*. *Meteor*. *Climatol*., **50,** 1725-1739.

Chapter 2:

A Statistical Model of Tropical Cyclone Tracks in the Western North Pacific with ENSO-Dependent Cyclogenesis

Emmi Yonekura[1] and Timothy M. Hall[2]

[1] Department of Earth and Environmental Sciences, Columbia University, New York, New York, U.S.A.

[2] NASA Goddard Institute for Space Studies, New York, New York, U.S.A.

Expanded from a paper published in *Journal of Applied Meteorology and Climatology*, v. 50, 1725-1793, doi: 10.1175/2011JAMC2617.1, 2011

Abstract

A new statistical model for western North Pacific tropical cyclone genesis and tracks is developed and applied to estimate regionally-resolved tropical cyclone landfall rates along the coasts of the Asian mainland, Japan, and the Philippines. The model is constructed on IBTrACS 1945-2007 historical data for the western North Pacific. The model is evaluated in several ways, including comparing the stochastic spread in simulated landfall rates to historic landfall rates. Although certain biases have been detected, overall the model performs well on the diagnostic tests, for example, reproducing well the geographic distribution of landfall rates. Western North Pacific cyclogenesis is influenced by the El Niño/Southern Oscillation (ENSO). This dependence is incorporated in the model's genesis component to project the ENSO-genesis dependence onto landfall rates. There is a pronounced shift southeastward in cyclogenesis and a small but significant reduction in basin-wide annual counts with increasing ENSO index value. On almost all regions of coast landfall rates are significantly higher in a negative ENSO state (La Niña).

1. Introduction

Typhoons in the western North Pacific Ocean (WNP) have potential to cause great damage on populated coastal areas in China, Taiwan, Japan, and the Philippines. The Pacific's high sea surface temperatures (SST) provide a fertile environment for tropical cyclogenesis. Consequently, the Pacific has the highest annual storm count of any ocean basin, averaging about 35 storms per year (from the IBTrACS 1945-2007 averaged annual rates). The landfall rate of tropical cyclones (TC) is one convenient diagnostic of the impact of TCs on coastal regions. Assessing the risk of landfall and its variation with climate is important for coastal land use policy, disaster management, and financial decisions for insurers. Here, we describe a new statistical model for WNP typhoon genesis and tracks and apply the model to estimate landfall rates as a function of the state of the El Niño/Southern Oscillation (ENSO).

Our approach is to develop and apply a basin-wide statistical track model that simulates the full lifecycle of a TC, following and expanding on the model of Hall and Jewson (2007) for the North Atlantic. The model is constructed on a basin-wide data set, which is at least two orders of magnitude larger than data alone. A data set of synthetic TCs many times larger than the historical set is generated, and the synthetic TC tracks are used to determine landfall rates. The major components of the model are genesis, track propagation, and lysis (death). The primary application is the effect of ENSO on cyclogenesis and how this effect influences landfall rates.

Thus, a key feature of the model is the sensitivity of the genesis component to ENSO state. Previous studies that have explored the relationship in the WNP between ENSO and cyclogenesis (Chan 1985, 2000; Saunders et al. 2000; Chia and Ropelewski 2002; Wang and

Chan 2002; Camargo and Sobel 2005; Camargo et al. 2007a, 2007b; Dong 1988) have found that during an El Niño year, more TCs form in the northeastern part of the basin, while during a La Niña year, more TCs form in the southwestern part of the basin, concentrating nearer to the continent. Early studies indicate that this change is due to the change in the Walker circulation (Dong 1988). More recently, Camargo et al. (2007a) used a Genesis Potential Index to find that El Niño influences on relative humidity and low-level vorticity are responsible for the shift.

The shift in genesis location has implications on the rest of the TC lifecycle. Tracks in the WNP tend to re-curve farther North (above 35°N) during El Niño years, resulting in more landfalls on Japan and the Korean peninsula. La Niña years tend to have more straight moving tracks that make landfall on South China, the Philippines, and Vietnam (Camargo et al. 2007b; Wang and Chan 2002; Elsner and Liu 2003; Wu et al. 2004; Fudeyasa et al. 2006; Saunders et al. 2000). Further, TC lifetime and intensity is also affected by ENSO state in the WNP. Studies (Camargo et al. 2007a; Camargo and Sobel 2005; Wang and Chan 2002; Chan and Liu 2004; Chan 2005, 2006) agree that El Niño years produce TCs that are both more intense and last longer. The genesis location is partly accountable for this change as TCs that form in the southeastern part of the WNP have more time to intensify before making landfall and dissipating. Here, local Poisson regression is applied to model the shift in the geographic distribution of genesis with ENSO. Basin-wide Poisson regression on ENSO state is used to model the basin-wide TC frequency. The track model then allows these ENSO-genesis features to be projected onto East Asian landfall.

We begin by describing the data employed and follow with descriptions of the statistical methodology for each model component. Then the results are shown for track simulation and

evaluation of the model using several diagnostics. Finally, the changes in regional landfall rates with ENSO state are examined.

2. Data

The model is built on data from the International Best Track Archive for Climate Stewardship, or IBTrACS (Knapp et al. 2010). IBTrACS was constructed as an effort to compile the data from multiple observational records from institutions across the globe. It is especially useful for the WNP where there are many databases with overlapping and sometimes conflicting records. The advantage of using these "best tracks" is that they consider the records from all institutions and reconcile storm omission and repetition. All of the WNP data from 1945 to 2007 is used to incorporate data from the beginning of routine aircraft reconnaissance. The data is in the form of six-hourly storm center position coordinates and maximum sustained wind speeds, however, we only use the latitude and longitude coordinates to construct the track model. The output of the model is also in 6-hourly position and time steps.

The WNP has a high annual TC occurrence rate, totaling 2295 storms on which this analysis is based. These TC tracks are shown in Fig. 2.1. There is a clear overall pattern of storm tracks, with westward motion at low latitudes, recurvature, and eastward motion at mid- and high latitudes (Harr and Elsberry 1991). It is also clear that the historical tracks display large deviations from this mean path, which can be mimicked well stochastically.

For the genesis model, the Niño 3.4 Index averaged over July-October (JASO) is used to indicate the ENSO state. This data is derived from the monthly sea surface temperature anomaly in the 5°S-5°N, 170°-120°W region (Barnston et al. 1997) and is obtained from the NCEP Climate

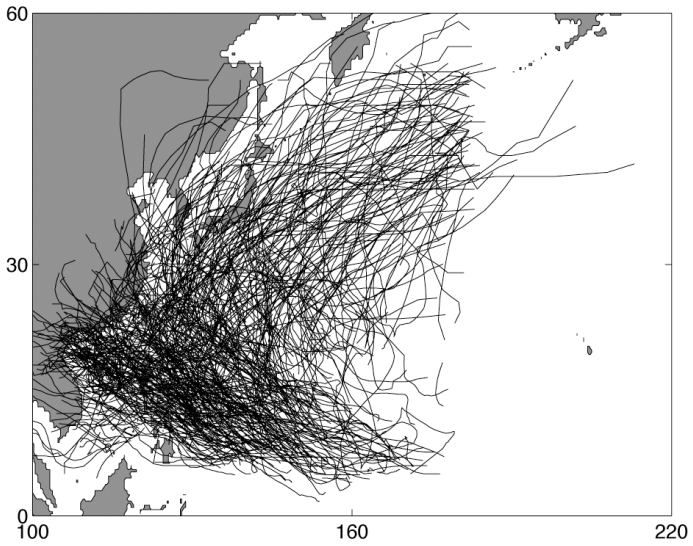

FIG. 2.1. Randomly selected 20% of the IBTrACS 2295 historical TC tracks from 1945-2007.

Prediction Center. In model simulations of the historical period, the JASO Niño 3.4 Index is used as input.

The model is relies on observed data that have some shortcomings. Regarding the TC observations, early in the record, there may have been TCs that were missed by the observation techniques used at the time. The observational methods have also changed over time in the WNP as routine aircraft reconnaissance was stopped in 1987 and heavy reliance was placed on using the Dvorak method from satellite observations, and the Dvorak method has also been evolving over time. It has also been observed that the behavior or ENSO changes, and the climate change seen post-1980 has been associated with more frequent and intense El Niño events. Because of this, there may be some model biases as we construct our model from all 1945-2007 years of observations.

One way we account for the uncertainty associated with our choice of observation years is to perform jackknife uncertainty tests for model diagnostics (i.e. landfall rates, track shifts), where a random 20% of the observed years are dropped out of the model construction repeatedly and the diagnostic quantity is then computed. The spread of the resulting estimates is then

considered in analysis. This accounts for the uncertainty that arises from choosing a particular sample of data.

3. Methods

The goal is to estimate TC landfall rates on WNP Asian coastlines and their sensitivity to ENSO state. Our approach is to construct a WNP-wide genesis-to-termination statistical model of TCs. Other approaches to landfall risk assessment are possible, for example, models based solely on landfall data (Chan and Shi 2000; Elsner et al. 2006). One advantage to a basin-wide model is the use of the much larger full-basin data set. Landfall rates depend on the statistical properties of TCs, and these can be estimated by using historical TC data over the entire basin, in addition to the actual TC segments making landfall. Another advantage to a basin-wide model is the increased physicality: the influence of climate state on different components of TCs (e.g., genesis location, track propagation, intensification) can be determined independently. A disadvantage is the increased complexity of the model, and the consequent increased possibility for model bias. Hall and Jewson (2007) explored quantitatively for a North Atlantic track model the trade offs between increased precision (use of more data) and the potential loss of accuracy (increases chances for bias), compared to a model use solely landfall data.

Previous statistical track models include Drayton (2000) from the private sector and Darling (1991), Chu and Wang (1998), Vickery et al. (2000), Emanuel et al. (2006), James and Mason (2005), Rumpf et al. (2007), and Hall and Jewson (2007) from academic research. Not all employ a full statistical track model, and most focus on hurricanes in the North Atlantic. The basic approach to the model construction is local regression, closely following the work of Hall and Jewson (2007) for the North Atlantic. Local regression acknowledges that data geographically close to a location in question is most appropriate for estimating TC properties at

the location. The length scale defining "close" is determined objectively in a manner to maximize the predictive skill of the model. Many features of our model are identical to those of Hall and Jewson (2007). These components are reviewed briefly in the following sub-sections. Two components, genesis and the modeling of track errors, are distinct from Hall and Jewson (2007) and are described in more detail.

a. Genesis

The genesis model component determines how many TCs form in a year and where these TCs originate. The genesis model component from Hall and Jewson (2007) determined the number of storms forming annually in the North Atlantic by sampling a Poisson distribution whose mean is the historical average formation rate over the basin in the time period they analyzed. Where the TCs originated was determined by random sampling of an empirical kernel-density function. The Hall and Jewson (2007) genesis has no climate state sensitivity.

Because ENSO has been shown to influence TC formation in the WNP, it is included in this model. Genesis is still modeled as a Poisson process, but now the mean rate is dependent on ENSO state. Poisson regression is employed, which is the appropriate form of regression for count data (Sabbatelli and Mann 2007). The dependent variable is the annual formation rate (the mean Poisson rate) over the full domain, and it is related to the independent variable, the ENSO index, using a log-link function: $\lambda_j = \exp(\beta_0 + \beta_1 * \mathrm{ENSO}_j)$, where the β are regression parameters and ENSO_j is the value of the ENSO state index for a specific year j. (β_1 is analogous to the slope and β_0 the y-intercept of linear regression.) The regression parameters are chosen numerically to maximize the likelihood of the observed annual count time series, given the historical ENSO state index time series. In any particular year, the Poisson distribution associated with λ_j is sampled to obtain a simulated TC count for the year.

Next we need to model where in the basin the TCs form. Local Poisson regression is used to simulate the local influence of ENSO on genesis. At each point on a one-degree grid the time series of annual TC formation counts within L = 370km (see below for an explanation of the length scales) of the grid-box center is Poisson-regressed against the time series of ENSO state index. The rates are divided by the area of the 370km circle and multiplied by the grid-box area to obtain the mean rate on the grid box. In data-sparse regions regression is omitted, and the annual mean count is used for the Poisson rate. (If too few non-zero annual values are available, then the regression is unstable and subject to large sampling error. The threshold value of five is somewhat arbitrary, striking a balance between avoiding local "hot spots" induced by sampling error and avoiding sensitivity to the threshold of the integrated basin-wide rate.) Symbolically, then, in data-rich regions the one-degree Poisson rate is $\lambda'_j(r) = A_g \exp(\beta'_0(r) + \beta'_1(r) * \mathrm{ENSO}_j)$, where r is the location, A_g is the ratio of the area of the local one-degree grid box area to the area of the local 370km circle, and the primes on λ and β indicate that the variables are now spatially variable.

Fig. 2.2 illustrates the procedure. The IBTrACS genesis sites are shown on the map, along with several of the overlapping 370km data circles. Inset are one circle's time series of ENSO values, the independent variable, and the annual TC formation count in the circle, the dependent variable. A probability density function (pdf) is then calculated by dividing the gridded local Poisson rates by the integrated sum of all local Poisson rates. Given N total TCs from the basin-wide genesis model, the pdf is sampled N times to obtain the genesis location of storms in a simulated year with a given ENSO state.

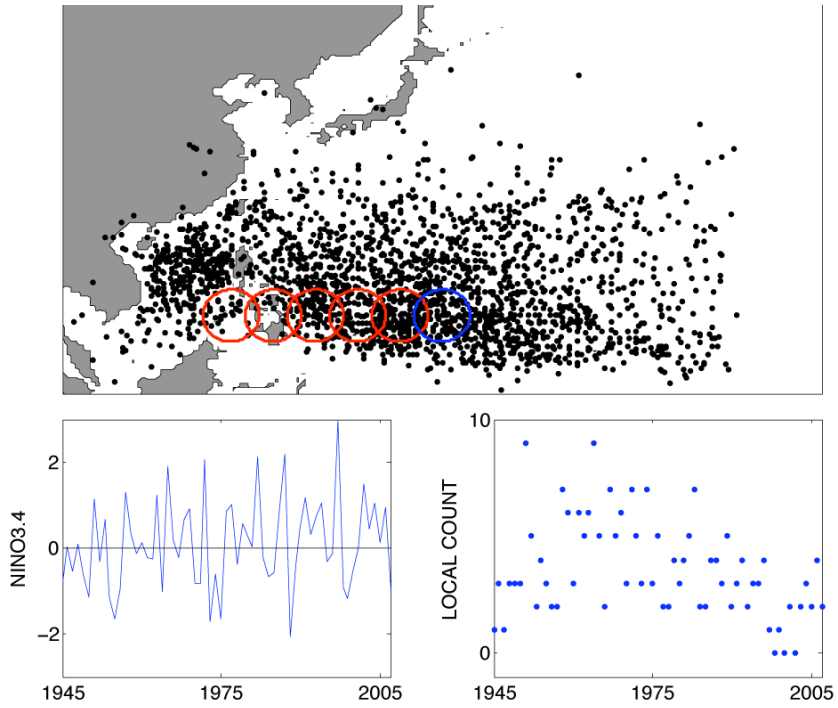

FIG. 2.2. Illustration of the local Poisson regression procedure for the genesis model. (top) Map of the historical genesis sites with examples of overlapping 370km circles. (bottom) Time series of the JASO Niño 3.4 index and annual genesis counts in the blue circle.

b. Track Propagation

TC propagation occurs by successive simulation of 6-hour track displacements. The model for the 6-hour increment is similar to that of Hall and Jewson (2007). The mean increment and the variance about the mean are computed locally by a weighted average of nearby historic increments, with the weighting length scale determined by out-of-sample minimization of forecast error (the mean) and maximization of likelihood (the variance). Also, as in Hall and Jewson (2007) the standardized errors are modeled as lag-one auto-regression, AR(1), with autocorrelation coefficients computed by distance-weighted averaging of historical data.

The difference between our analysis and Hall and Jewson (2007) is the procedure to standardize the errors on which the AR(1) is applied. The AR(1) is applied independently to the vector components of the standardized track error, under the assumption that the components are uncorrelated. The Hall and Jewson (2007) standardized errors are in a frame of reference

parallel and perpendicular to the local mean track increment, but we have found that this does not always result in independent error components. Here, the scatter about the mean increment is allowed to determine the principal axes of the local error ellipse, and standardize the error in this local frame. Using the data-determined error ellipse frame better ensures the components of the 2-D standardized errors are uncorrelated.

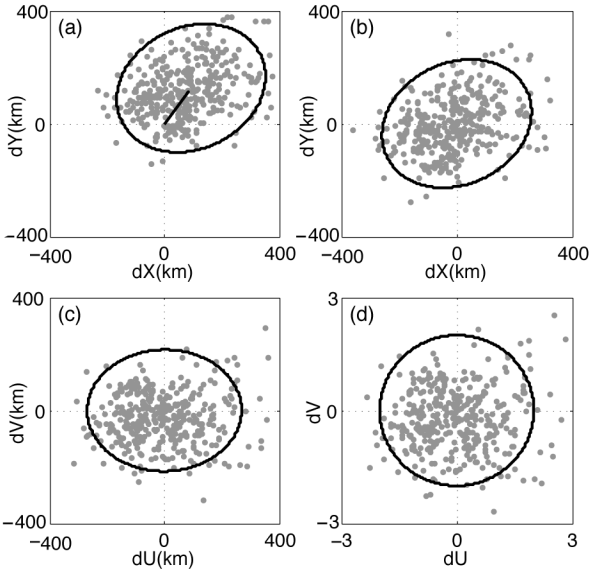

FIG. 2.3. (a) The x and y displacement values near grid point (34˚N, 133˚E) are plotted against each other. The mean track increment vector is in black as well as the error ellipse defined by the principal axes. (b) As in the first panel, but now with the mean x and y increments removed. (c) As in the second panel, but now rotated to the covariance-ellipse principal axes. (d) As in the third panel, but now with the residuals divided by the rms variances along the major (u) and minor (υ) covariance-ellipse axes. In this final panel the deviations, u and υ, are now uncorrelated, and comprise the standardized anomalies to be modeled independently.

The standardizing procedure is illustrated in Fig. 2.3. In the scatter plots of Figs. 3a and 3b (with and without means, respectively) it is clear that the x and y errors are correlated and, therefore, cannot be modeled independently. The errors are modeled with a generalized two-dimensional normal distribution, in which the variances in each dimension are allowed to be distinct and the motions in the two dimensions can co-vary (termed a "bivariate anisotropic correlated normal distribution"). The 2-D scatter of such a distribution can be characterized by an error ellipse, whose major axis makes an angle

$$\alpha = \frac{1}{2}\tan^{-1}\left(\frac{c_{xy}\sigma_x\sigma_y}{\sigma_x^2 - \sigma_y^2}\right)$$

with respect to the *x* axis (line of constant latitude), where σ_x and σ_y are the rms error variances in the *x* and *y* (longitudinal and latitudinal directions) and c_{xy} is the *x*-*y* error correlation. Rotating the *x*-*y* error into the principal axes frame of reference (Fig. 2.3c) results in transformed errors, *u* and υ, that are independent and can be modeled as such. Finally in Fig 3d the errors are divided by the rms variances in the principal axes to standardize them. Note that the degree of *x*-*y* error correlation varies spatially, and can be as high as 0.8 in some regions, illustrating the importance of accommodating it.

As in Hall and Jewson (2007) for the North Atlantic, here for the WNP we have checked for evidence of higher order lags and for non-normality in the errors. Higher lags are tested by performing multiple-variable regression of standardized errors against themselves at a number of lags, *i*-1, *i*-2, *i*-3, etc. Only lag one was found to be significant. Normality was checked with quantile-quantile analysis. In both the *u* and υ directions there are deviations from normality beyond two standard deviations. It was a concern that these "fat tails" might compromise the results, since normality is assumed in several stages of the analysis, most importantly in the random forcing (step six above). To test sensitivity simulations are performed in which archived historical errors are randomly sampled rather than using normal distribution forcing. If fat tails in the errors played a large role in track propagation then one would expect a noticeable difference in simulation behavior between normal distribution forcing and archived-error sampling. In fact, there was no significant difference in track behavior according to the diagnostics described below.

c. Lysis

Lysis (the termination of tracks) is identical to Hall and Jewson (2007). The probability, P, for track lysis (termination) in a six-hour time step at position r is the ratio of the weighted sum of all terminal historical track points to the weighted sum of all track points. Over-ocean and over-land lysis are separated using a 0.25-degree mask to obtain different rates, as the physical processes on land and ocean are different.

d. Optimized Averaging Scales

In using historical data for each of the model components the weight applied to a datum increases with geographic proximity to a simulation location in question (potential genesis site, current track location, potential lysis site). The length scale of the weight determines the balance between the desire to use as much data as possible (a large scale) and the desire to resolve geographic structure as well as possible (a small scale). Hall and Jewson (2007) described year-by-year jackknife out-of-sample procedures to determine the length scales objectively, and we use their procedure here. The out-of-sample nature of the procedure (use of one data subset to build the model and use of the remainder subset to evaluate the model) ensures that the model is optimized for prediction.

Because we are working here in a different basin with different data volumes and different geographic distributions of statistical TC properties, the length scales obtained are not identical to those of Hall and Jewson (2007). We obtain 370km for the local Poisson regression for genesis, 220km for ocean lysis, 830km for land lysis, 220km for the mean track, and 260km for the track variance. As illustrated in Hall and Jewson (2007), use of scales smaller than the optimal scale results in simulations whose features have unwarranted fine spatial structure. Use of scales larger than optimal results in excessive smoothing of true geographic structure. An

optimal length scale for the track-error autocorrelations was not obtained. We used 500km and found little sensitivity to varying this.

e. Simulation

The steps to simulate the historical period (1945-2007) is as follows:

- For each of the 63 years, both the basin-wide Poisson rate and a grid of local Poisson rates are calculated using the historical ENSO state of the respective year. The associated Poisson distribution for the basin-wide Poisson rate is sampled to give an annual count, N, for the basin. The local Poisson rates are used to calculate a normalized pdf that is sampled N times to give the locations of genesis.
- Tracks propagate from the genesis in 6-hour time steps. At each position the AR(1) model gives the standardized error $u_i = c_u\, u_{i-1} + s\varepsilon$ where c_u is the autocorrelation coefficient, ε is the standard normal random, and $s = \left(1 - c_u^2\right)^{1/2}$ is the magnitude of the random term (Hall and Jewson 2007). A similar expression holds for the v_i, the perpendicular component of the error. (For the first step $c_u = c_v = 0$). The errors are then multiplied by the variances in the local principle component reference frame, rotated back to the longitude-latitude frame, and the means are added, resulting in the next track increment. The simulated TC position is updated.
- At each position lysis is checked by comparing the local lysis probability P to a uniform random draw, R, from zero to one. The track is terminated if $P > R$.
- The procedure is repeated for all storms produced by the genesis model for each simulated year, and then for the desired number of simulations of the 1945-2007 period.

In the analysis that follows, 500 such simulations were used. This constitutes the ensemble of simulations of the 1945-2007. The model is stochastic, so each simulation is distinct.

4. Results

a. Model Diagnostics

Fig. 2.4 shows the historical tracks and three realizations of the 63-year simulations; e.g., three members of the ensemble of simulations. Qualitatively, the simulated tracks reproduce the large-scale features of the historical tracks, propagating westward in the subtropics and eastward in mid-latitudes. We aim to evaluate the model more quantitatively. The model performs "well" on a diagnostic to the extent that the historical value of the diagnostic falls inside some confidence band of the range of simulated values of the diagnostic (e.g., the middle 95%). That is, a historical value should appear to be a typical draw from the ensemble of simulated values, rather than an outlier. Where this is not the case, the model is biased with regard to the diagnostic. Here, the model is evaluated in this way with respect to three diagnostics: (1) track crossings of lines of constant longitude, (2) spatial maps of track density; and (3) landfall rate and its geographic distribution.

It is important to note that the model is not fit, or trained, to these diagnostics. The large-scale behavior of simulated tracks emerges from the point-by-point stochastic modeling of genesis and the step-by-step stochastic modeling of six-hourly track increments. The model parameters (the averaging length scales) are chosen objectively to optimize the point- and step-processes.

Fig. 2.5 shows eastward and westward track crossings over lines of constant longitude (counts in five-degree latitude bins) from the historical record and the simulations. Shown are

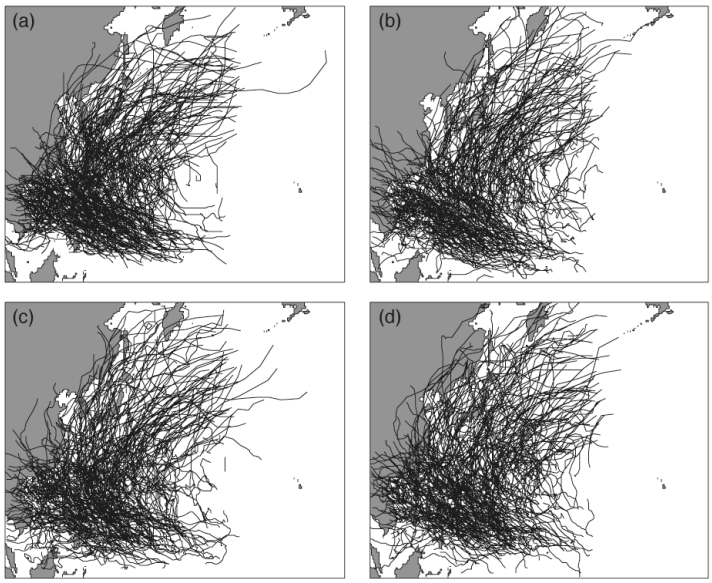

FIG. 2.4. (a) Historical tracks from 1945-2007 in IBTrACS archive. (b)-(d) Three independent model realizations of the historical period. For all panels, a random 20% of the tracks were selected in order to better see the individual track shapes.

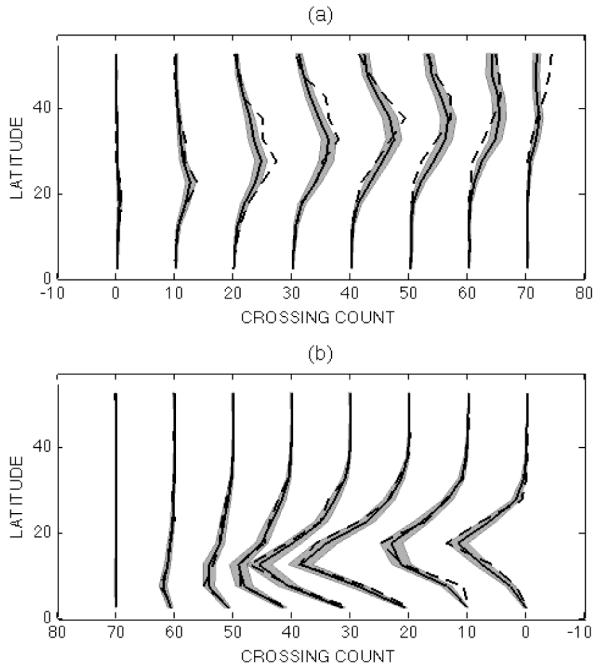

FIG. 2.5. Number of TCs crossing longitude lines (110ºE to 180ºE equally spaced left to right) as a function of latitude. Unit increments on x-axis are crossings per 5º latitude. The lower panel is westward crossings and the upper panel is eastward crossings. Dashed lines are historical, and solid lines are ensemble mean simulation with shaded gray area indicating ± one standard deviation.

means across the 500-member simulation ensemble and the inner 95% range about these means. This range about the model mean is used as the measure of significant difference between modeled and historical track crossings. Where the historical curve falls outside the spread about the model mean, the model is biased, according to this confidence standard. The behavior of the mean track is to move westward between 5°-20°N and eastward between 20°-45°N. As can be seen in the figure, the distribution of east and west track crossings closely follows that of the historical crossings, except for a few scattered regions where the historical curves lie outside the model spread.

Track density (number of six-hour TC points per unit area) is also used as a diagnostic. Fig. 2.6a and b show the historical and ensemble mean track density, respectively. The overall density distribution is well reproduced by the model, but the model overestimates the maximum in density around the Philippines and underestimates it from Southeast Asia to Japan. Fig. 2.6c shows the spread of the simulation ensemble; e.g., the difference between the model's 2.5% and 97.5% percentile track density value at each grid point. This range has a maximum where the observed track density maximum appears. Fig. 2.6d shows a measure of the significance of the model-observation difference: regions where the observed track density is above the 97.5% simulation percentile level are red, and regions where the observed track density is below the 2.5% level are blue. The regional model disagreements and the difference in magnitude of the maximum track density are significant by this standard. We are currently exploring the reasons for these biases. In other regions the model shows no coherent bias.

Landfall risk assessment is the ultimate application of the model, so examining landfall rates of the simulations is a key diagnostic. The coastline is divided into segments approximately 1000km long, covering the Asian mainland, Japan, the Philippines, Indonesia and Malaysia, and

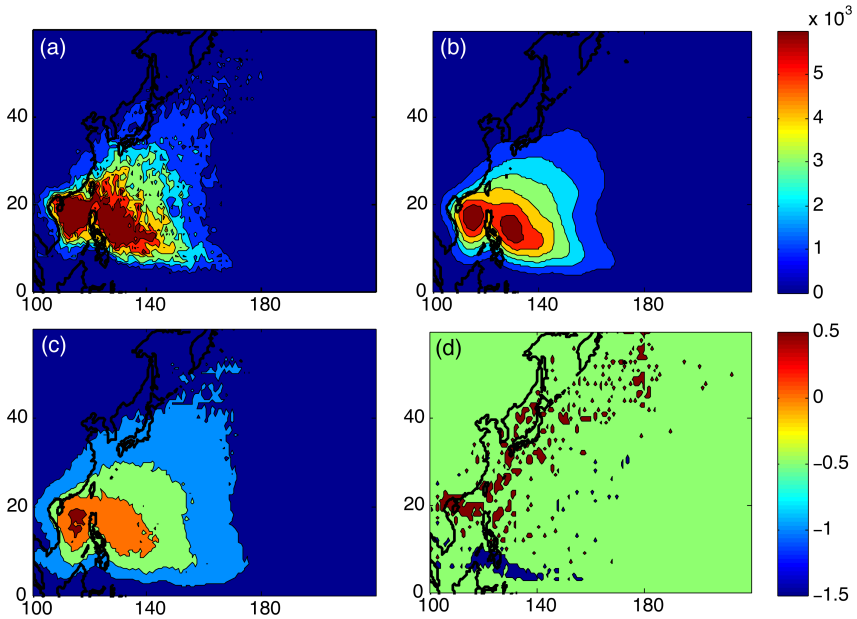

FIG. 2.6. (a) Historical track density (points per one-degree box in 1945-2007 period) (b) 500-realization ensemble average track density. (c) Spread of the ensemble, shown by ordering track density values at each grid point and taking the difference between the 97.5% and 2.5% percentile values. (d) Red regions show where the historical track point density is above the 97.5% percentile level for that grid point. Blue shows where it is below the 2.5% percentile level. Green is where the historical values are bounded by the inner 95% of the ensemble.

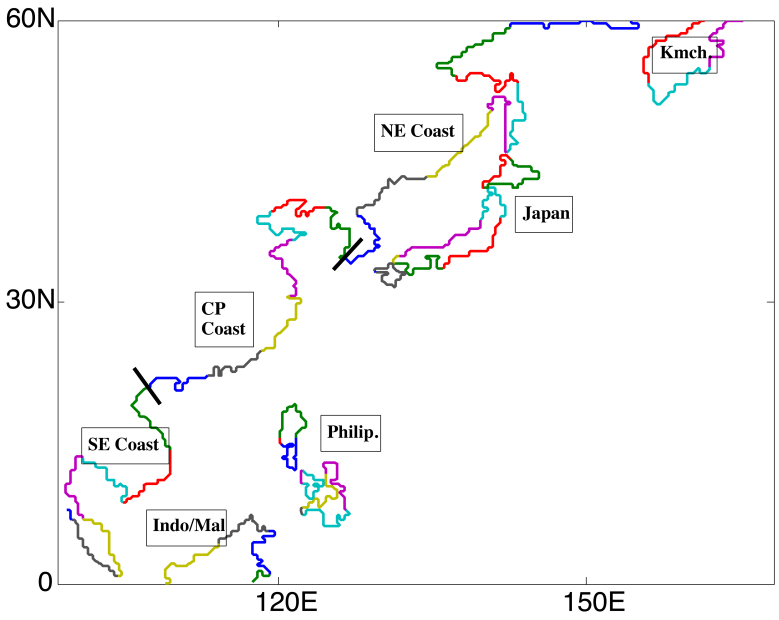

FIG. 2.7. Map of the 47 segments lining the main coast and significant other landmasses. Political regions are also marked for landfall analysis.

Kamchatka, as illustrated in Fig. 2.7. A landfall occurs on a segment if a track crosses the segment heading from ocean to land. The landfalls are accumulated and plotted as a function of

distance along the coastlines in units of landfalls per year per 100km of segmented coastline. Shown in Fig. 2.8 are the historical landfall rates, the model ensemble mean landfall rate, and the middle 95% range of simulated rates across the ensemble.

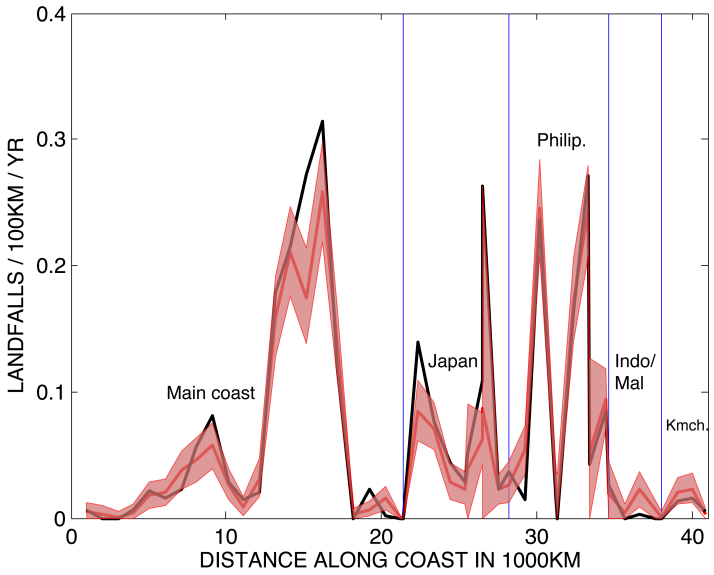

FIG. 2.8. Landfall rates along the East Asian coast. The figure shows the historical (black) and ensemble mean (red) with red shading for the inner 95% of the simulated landfalls. Units are counts per 100km per year.

There is a high degree of structure in the geographical distribution of landfall rates, even within regions of high track density, much of which can be understood in terms of the relative orientation of coastline segment and the direction of the mean track. If a coastline segment is parallel to the local mean track then a landfall is relatively unlikely, though not impossible, given random motions about the mean. If a coastline segment is perpendicular to the local mean track direction then a landfall is relatively likely. Overall, the model captures the geographical distribution: the local maxima and minima of the landfall rate are well matched. However, the model exhibits low landfall biases in certain regions, consistent with behavior seen in the track density. Historical landfall counts are above 97.5% of the model simulations on the coast of China as well as Japan; e.g., the model displays a low landfall bias on these regions. The model

performs well in matching the historical landfalls for the Philippines, and it performs well on other less active regions.

Finally, 1000 simulations of 2008-2009, two out-of-sample years, are performed using the observed values of the JASO Niño3.4 index. The landfall rates are computed for political regions defined in Fig. 2.7, and the distributions are compared to observed landfall rates for 2008-2009 (Fig. 2.9). Results show that the observed rates occur within the modeled distribution.

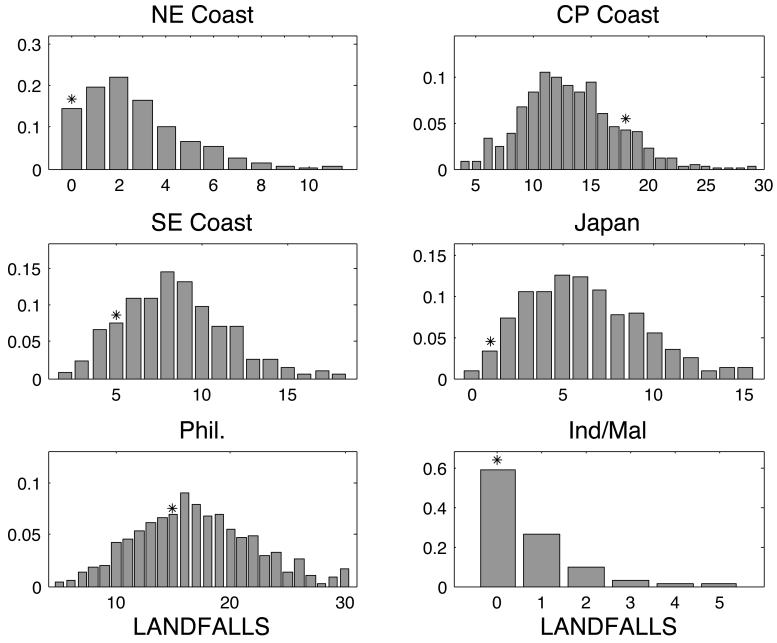

FIG. 2.9. Out-of-sample test using landfall data from 2008-2009. For each political region, the bars represent the distribution of landfalls resulting from 1000 model simulations of the out-of-sample period. The star represents the historical (IBTrACS) values for landfalls in 2008 and 2009.

b. ENSO Dependence

We now turn to the role of ENSO in WNP TC genesis and, through genesis, its impact on landfall rates. The results for ENSO's influence on total genesis and its geographic distribution confirm those of previous studies (Chan 1985, 2000; Chia and Ropelewski 2002; Wang and Chan 2002; Camargo et al. 2007a). The coefficients from the local Poisson regression are shown in Fig. 2.10. Notice the coefficient that multiples the ENSO state variable, β_1, changes sign from positive in the southeast part of the basin to negative in the northeast. The implication on genesis

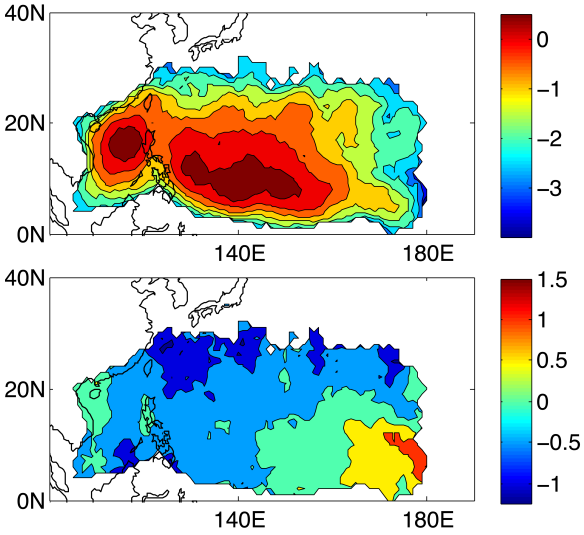

FIG. 2.10. Map of the local beta coefficients, β_0 (top) and β_1 (bottom), calculated from local Poisson regression of genesis points and ENSO state.

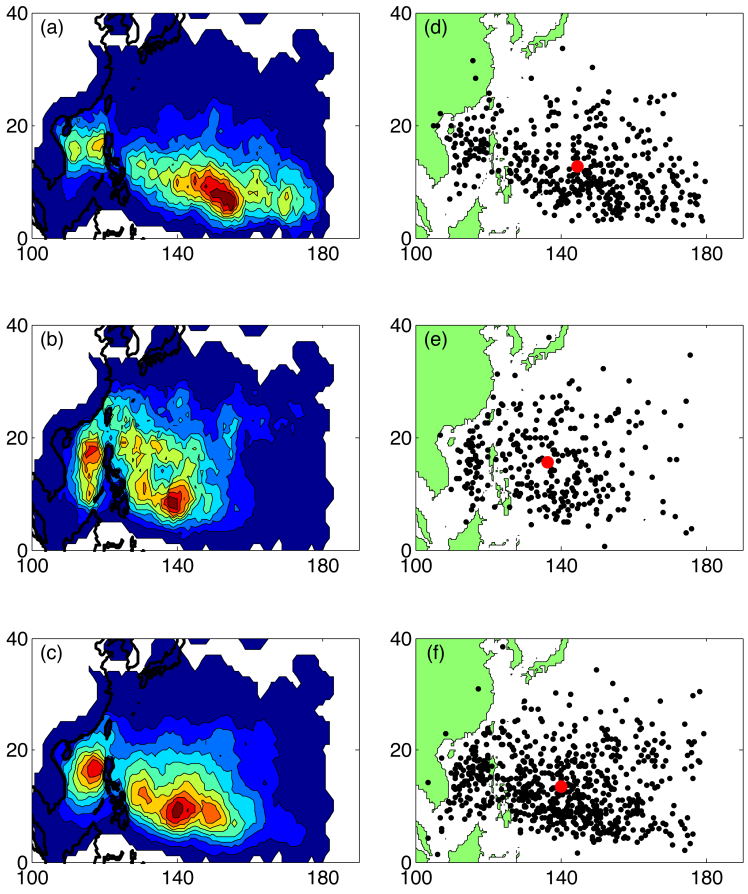

FIG. 2.11. Maps of normalized probability distribution function from local Poisson rates, given the JASO Niño 3.4 index values of (a) 2, (b) -2, and (c) 0. Panels (d)-(f) show the corresponding IBTrACS genesis sites for years with JASO Niño 3.4 index values (d) greater than 1σ, (e) less than -1σ, and (f) less than 1σ but greater than -1σ. The red point marks the mean genesis location.

rates is further elucidated in Fig. 2.11a, b and c, which show the normalized pdf's produced using the distribution of annual formation rates from the Poisson regression for three values of ENSO state index: $+2\sigma$, 0, and -2σ. There is a northwestward shift in formation and an increase in the region west of 140°E and south of 30°N from El Niño to La Niña states. The historical genesis sites at corresponding ENSO states are shown in Fig. 2.11d, e and f, and the shifting behavior is evident. This shift is seen most clearly in Fig. 2.12, a map of the difference, El Niño ($+2\sigma$) minus La Niña (-2σ).

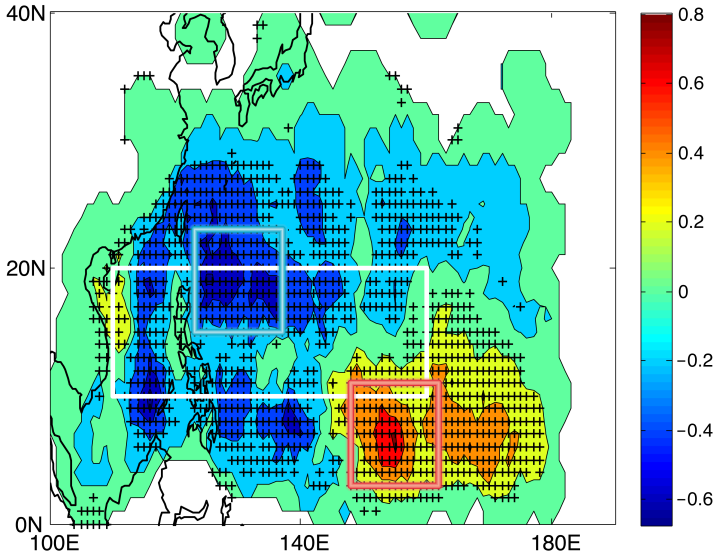

FIG. 2.12. Pdf difference of using ENSO state anomaly of 2 and -2. The crosses mark the regions where the sign of the difference remains the same for the inner 95% of the bootstrap reconstructions of the genesis model that dropped out a random 20% of the data. The white box defines the "main development region", the red box denotes the "warm" region, and the blue box denotes the "cool" region.

The dependence of the basin-wide annual count on ENSO (drawn from the Poisson distribution for the entire basin) is shown in Fig. 2.13a. The annual count decreases from 39 to 34 per year with a -2σ to $+2\sigma$ shift in ENSO. Given the indicated 95% range of the annual counts, this change is barely significant. Figs. 12b, c and d show the annual counts as functions of ENSO state for sub-regions of the basin indicated in Fig. 2.12: the main development region, or "MDR" (10-20°N, 110-160°E); the "cool" region; and the "warm" region. In the MDR an

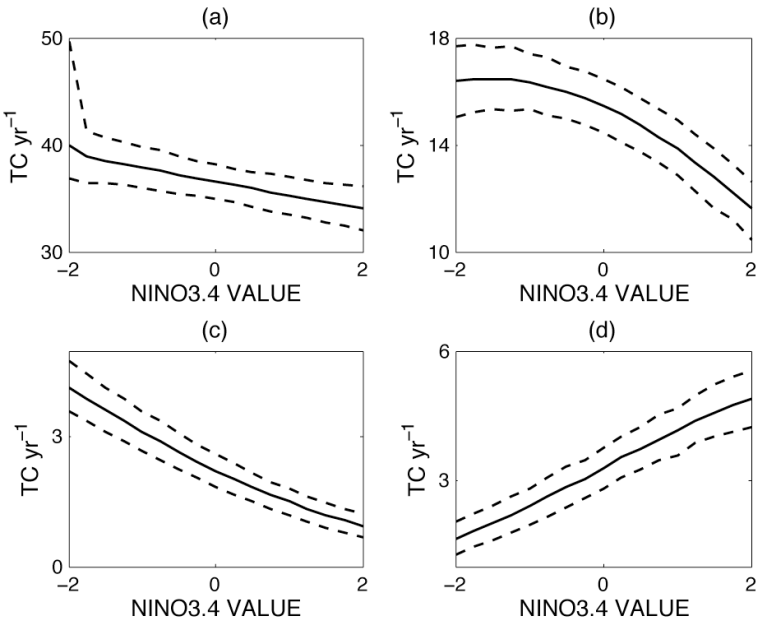

FIG. 2.13. Annual formation counts for different phases of ENSO for the (a) entire domain, (b) main development region, (c) "cool" region, and (d) "warm" region as defined in Fig. 2.12. Dashed lines indicate the inner 95% range from jackknife method, and the solid line is the mean of 1000 jackknife versions of the genesis model.

ENSO change from -2σ to +2σ decreases the Poisson rate by five storms per year. In the "cool" region, the same +4σ ENSO change decreases the Poisson rate by roughly three storms per year. By contrast "warm" region has statistically more genesis activity during El Niño conditions: a -2σ to +2σ ENSO shift causes an increase of about three storms per year. It should be noted that the Poisson regression model is not linear; genesis sensitivity to a specified change in ENSO depends on the absolute ENSO value about which the change occurs.

To determine significance of these ENSO-genesis sensitivities a jackknife test is performed. The counts are Poisson-regressed on ENSO over the basin 10,000 times, in each case randomly dropping 13 (20%) of the data years used in the regression. In "delete-d jackknife" the point is to choose a d > 1 to increase the number of data subsets across which a statistic can be computed. For d=1 there would be 63 (1945-2007) subsets of 62 years each, which is not enough to examine the tails of the distribution; e.g., to estimate the 2.5% and 97.5% confidence bounds. For d=13 there are 63!/[13!(63-13)!] ~ 10^{12} subsets of 50 years each. On the other hand

d should not be chosen so large that each subset is too small to perform regression. The value d=13 is a compromise.

In Fig. 2.12, El Niño minus La Niña differences are deemed significantly different than zero at a given location if the inner 95% of the differences across the jackknife set have the same sign. Locations where this is true are indicated in Fig. 2.12 with plus symbols. The regions of largest ENSO sensitivity are all significant by this measure. The same jackknife test is used to put confidence bounds (middle 95%) on formation rates as a function of ENSO (Fig. 2.13). These bounds suggest that ENSO sensitivity is significant on a regional basis. The basin-wide decline in formation rates with increasing ENSO state (Fig 13a) is fractionally smaller than the regional changes because of cancellation due to opposing sensitivities in the "warm" and "cool" regions. In order to test the significance of basin-wide sensitivity, the distribution of β_1 coefficients (the coefficient multiplying the ENSO value) is examined across the set of jackknife basin-wide regressions. The 2.5% and 97.5% percentile values of these β_1 are roughly -0.06 and -0.01, respectively, indicating that the basin-wide formation decline with ENSO is significant. Thus, although we agree with the findings of Camargo and Sobel (2005) and Wang and Chan (2002) that basin-wide formation sensitivity to ENSO is fractionally miniscule compared to regional sensitivity, we find the small sensitivity to be significant.

Both the change in basin-wide rates and the shift in distribution with ENSO have consequences for landfall rates. During a La Niña event more TCs form in the basin and they form closer to the Asian coast. The impact of ENSO on landfall rates is shown in Fig. 2.14. Fifty model simulations of 1945-2007 are performed, each with a different fixed value of ENSO. The ensemble mean landfall profile is computed for each ENSO value. For most regions La Niña results in higher landfall than El Niño. This is illustrated in Table 1, where the landfall rates of

TABLE 2.1. Landfall rates, in units of landfalls yr^{-1} $100km^{-1}$, for specific political regions given different Niño3.4 JASO values. The bottom row shows the change from a +2 to -2 phase of ENSO. The last column also gives the genesis rates, in TC yr^{-1}, for each ENSO state.

ENSO state	SE Asia	CP Asia	NE Asia	Japan	Phil.	All	Genesis rates
2	0.06	0.08	0.01	0.04	0.12	0.05	34.04
0	0.07	0.10	0.02	0.05	0.14	0.06	36.53
-2	0.07	0.11	0.02	0.06	0.13	0.07	39.21
% change*	17.82	40.80	47.58	40.82	9.51	26.26	15.19

* For rate *r*, % change is [*r*(ENSO=-2) – *r*(ENSO=+2)] / *r*(ENSO=+2).

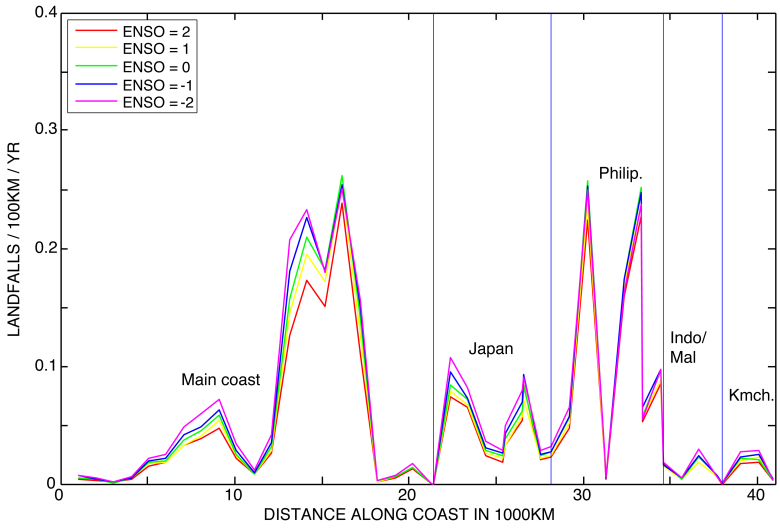

FIG. 2.14. Landfall rates from 50-realization model runs of the historical period given a stationary value of JASO Niño3.4 anomaly. Positive anomalies are El Niño years, and negative anomalies are La Niña years.

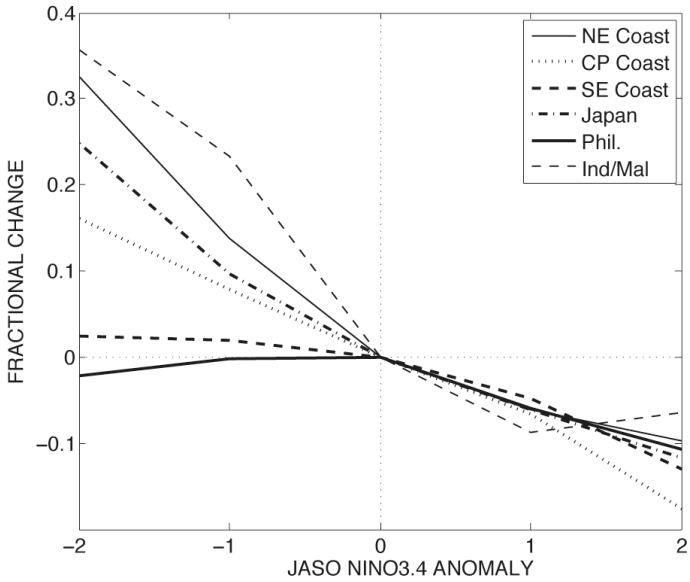

FIG. 2.15. Fractional change in landfall for political regions given a stationary value of ENSO anomaly.

several political regions defined in Fig. 2.7 are shown for different ENSO states. For example, the Central Pacific Asia coastline has a landfall rate increase of 40% for a -2σ to +2σ ENSO change. For the same change, the Philippines show a 9.5% landfall rate increase.

To better highlight the regional effects of ENSO state on landfall rates, Fig. 2.15 shows the fractional change in landfall rates for regions defined in Fig. 2.7. All regions show a decrease in fractional change with increasing value of ENSO state index. The change is most drastic from a strong La Niña event to a neutral state for Indonesia/Malaysia, the northeast mainland coast, and Japan. This does not agree with previous work (Wu et al. 2004; Saunders et al. 2000; Elsner and Liu 2003) that finds increased landfalls on Japan, Korean peninsula, and northern China during El Niño events.

5. Discussion

We have developed a new statistical model for WNP typhoon tracks and genesis based on IBTrACS data. The primary application is estimating Asian typhoon landfall rates on a regional scale and their sensitivity to ENSO. Model parameters (length scale in the local regression) are determined by an out-of-sample procedure to maximize the model's ability to forecast. The model captures well the overall features of WNP typhoon genesis and propagation, realistically reproducing both mean structure and pseudo-random variation about the mean. The geographic distribution of landfall rates is reproduced well in both historically active and less active regions. The realistic behavior in less active regions (e.g., Indonesia and Malaysia) is encouraging: a track model should be most advantageous over a model based solely on historical landfalls in regions where landfalls are rare.

The analysis reveals some model biases whose sources remain to be isolated and corrected. The discrepancy in track point density indicates that the model may be moving the storms too slowly to reach the coastal areas. This gives storms more chance to suffer lysis before making landfall, resulting in the low landfall biases seen on certain regions. The model also places roughly five degrees too far south the latitude of maximum eastward storm propagation in mid-latitudes (Fig. 2.5a). Many of the historic storms in this region have undergone extratropical transition, which may affect their propagation, but has not been explicitly considered here.

The overall decrease in fractional change with increasing ENSO Index, which disagrees with some previous studies, is likely due to a combination of things. On one side, the previous studies could be affected by sampling bias as they are based off of a limited number of observed ENSO events and TCs. The previous work is also subject to uncertainty in the ENSO-TC relationship due to the climate and ENSO not being stationary as well as observational inconsistencies. On the other side, our model only has ENSO dependence in the genesis component for this chapter, but adding ENSO dependence in the track propagation component may result in more regional landfall agreement with other studies, which will be investigated in the next chapter. Further, there is a large seasonal effect in TC activity in the WNP that has not been accounted for, which may also account for some differences in the results of this chapter.

The genesis model has been constructed to be sensitive to ENSO. Regions of peak formation shift southeastward during El Niño and northwestward during La Niña, in agreement with results of previous studies. The combined effects of a marginally significant increase in overall storms and formation closer to land result in more landfalls during La Niña. However, important ENSO effects remain to be included in the model, which may modify these results. Other studies (Wang and Chan 2002; Elsner and Liu 2003; Camargo et al. 2007b) argue that TC

track shapes are sensitive to ENSO. Some of this effect is included in the sensitivity of the genesis distribution, as TCs forming in different regions will follow different trajectories according to the model. However, there may be additional influence not included that could be introduced by explicitly adding ENSO sensitivity to the track propagation component of the model. This may help account for the differences in landfall sensitivity to ENSO found in this study compared to previous studies. Crucially, and intensity model has not yet been implemented, and all landfalls are treated equally. TCs in El Niño years form farther from the coast and, therefore, have more time to intensify before making landfall (Wang and Chan 2002; Chan and Liu 2004; Chan 2005, 2006; Camargo and Sobel 2005; Camargo et al. 2007a). Thus, even though La Niña years have more overall landfalls, El Niño years produce more intense landfalls, which dominate risk assessment considerations. This idea will be explored further once an intensity model is implemented.

Acknowledgments.

The authors are grateful to Suzana Camargo and Anthony Del Genio for helpful comments on this work.

References

Barnston, A. G., M. Chelliah, and S. B. Goldenberg, 1997: Documentation of a highly ENSO-related SST region in the equatorial Pacific. *Atmos.-Ocean*, **35**, 367-383.

Camargo, S.J. and A.H. Sobel, 2005: Western North Pacific tropical cyclone intensity and ENSO. *J. Climate,* **18**, 2996-3006.

Camargo, S.J., K.A. Emanuel, and A.H. Sobel, 2007a: Use of a genesis potential index to diagnose ENSO effects on tropical cyclone genesis. *J. Climate*, **20**, 4819-4834.

Camargo, S.J., A.W. Robertson, S.J. Gaffney, P. Smyth, and M. Ghil, 2007b: Cluster analysis of typhoon tracks. Part II: Large-scale circulation and ENSO. *J. Climate,* **20,** 3654–3676.

Chan, J.C.L., 1985: Tropical cyclone activity in the Northwest Pacific in relation to the El Nino/Southern Oscillation phenomenon. *Mon. Wea. Rev.,* **113**, 599-606.

Chan, J.C.L., 2000: Tropical cyclone activity over the western North Pacific associated with El Niño and La Niña Events. *J. Climate*, **13**, 2960-2972.

Chan, J.C.L., 2005: Interannual and interdecadal variations of tropical cyclone activity over the western North Pacific. *Meteor. Atmos. Phys.*, **89**, 143-152.

Chan, J.C.L., 2006: Comments on "Changes in tropical cyclone number, duration, and intensity in a warming environment". *Science*, **311**, 1713b.

Chan, J.C.L. and K.S. Liu, 2004: Global warming and western North Pacific typhoon activity from an observational perspective. *J. Climate*, **17**, 4590-4602.

Chan, J.C.L. and J. Shi, 2000: Frequency of typhoon landfall over Guangdong Province of China during the period 1470-1931. *Int. J. Climatology*, **20**, 183-190.

Chia, H.-H. and C.F. Ropelewski, 2002: The interannual variability in the genesis location of tropical cyclones and the northwest Pacific. *J. Climate*, **15**, 2934-2944.

Chu, P., and J. Wang, 1998: Modeling return periods of tropical cyclone intensities in the vicinity of Hawaii. *J. Appl. Meteor.,* **39**, 951-960.

Darling, R., 1991: Estimating probabilities of hurricane wind speeds using a large-scale empirical model. *J. Climate,* **4**, 1035-1046.

Dong, K., 1988: El Niño and tropical cyclone frequency in the Australian region and the North-western Pacific. *Aust. Meteor. Mag.,* **36**, 219–255.

Drayton, M., 2000: A stochastic basin-wide model of Atlantic hurricanes, *Proc. 24th Conf. on Hurricanes and Tropical Meteorology*, Ft. Lauderdale, FL, Amer. Meteor. Soc., 12797.

Elsner, J.B. and K.B. Liu, 2003: Examining the ENSO-Typhoon Hypothesis. *Climate Research*, **25**, 43-54.

Elsner, J.B., R.J. Murnane, and T.H. Jagger, 2006: Forecasting U.S. hurricanes 6 months in advance. *Geophys. Res. Lett.*, **33**, L10704.

Emanuel, K., S. Ravela, E. Vivant, and C. Risi, 2006: A statistical deterministic approach of hurricane risk assessment. *Bull. Amer. Meteor. Soc.*, **87(3)**, 299-314.

Emanuel, K., R. Sundararajan, and J. Williams, 2008: Hurricanes and global warming: results from downscaling IPCC AR4 simulations. *Bull. Amer. Meteor. Soc.*, **89(3)**, 347-367.

Hall, T.M., and S. Jewson, 2007: Statistical modeling of North Atlantic tropical cyclone tracks. *Tellus*, **59A**, 486-498.

Harr, P.A. and R.L. Elsberry, 1991: Tropical cyclone track characteristics as a function of large-scale circulation anomalies. *Mon. Wea. Rev*, **119**, 1448-1468.

James, M.K. and L.B. Mason, 2005: Synthetic tropical cyclone database. *J. Waterway, Port, and Ocean Eng.*, **131(4)**, 181-192.

Knapp, K. R., M. C. Kruk, D. H. Levinson, H. J. Diamond, and C. J. Neumann, 2010: The International Best Track Archive for Climate Stewardship (IBTrACS): Unifying tropical cyclone best track data. *Bull. Amer. Meteor. Soc.*, **91**, 363-376.

Rumpf, J., H. Weindl, P. Höppe, P. E. Rauch, and V. Schmidt, 2007: Stochastic modeling of tropical cyclone tracks. *Math. Meth. Oper. Res.,* **66(3)**, 475-490.

Sabbatelli, T.A., and M.E. Mann, 2007: The influence of climate state variables on Atlantic Tropical Cyclone occurrence rates. *J. Geophys. Res.,* **112**, D17114.

Saunders, M.A., R.E. Chandler, C.J. Merchant, and F.P. Roberts, 2000: Atlantic hurricanes and NW Pacific typhoons: ENSO spatial impacts on occurrence and landfall. *Geophys. Res. Lett.*, **27**, 1147–1150.

Vickery, P.J., P.F. Skerlj, and L.A. Twisdale, 2000: Simulation of hurricane risk in the US using an empirical track model. *J. Structural Eng.,* **126**, 12222-1237.

Wang, B. and J.C.L. Chan, 2002: How strong ENSO events affect tropical storm activity over the western North Pacific. *J. Climate*, **15**, 1643-1658.

Wu, M.C., W.L. Chang, and W.M. Leung, 2004: Impacts of El Niño–Southern Oscillation events on tropical cyclone landfalling activity in the western North Pacific. *J. Climate*, **17**, 1419–1428.

Chapter 3:

ENSO Effects on Tropical Cyclone Tracks and Genesis in the Western North Pacific

Emmi Yonekura[1] and Timothy M. Hall[2]

[1] Department of Earth and Environmental Sciences, Columbia University, New York, New York, U.S.A.

[2] NASA Goddard Institute for Space Studies, New York, New York, U.S.A.

Abstract

We use a statistical tropical cyclone (TC) track model based on the IBTrACS database for 1945-2007 to study the effect of the El Niño-Southern Oscillation (ENSO) on western North Pacific TC landfall. The model employs optimized local regression of TC formation rates and track increments on Niño3.4 and seasonal predictor variables. A comparison of simulations of the 1945-2007 period concludes that having both the genesis and track propagation components of the model depend on ENSO improves our model's skill in simulating TCs.

Changes in TC tracks and genesis are analyzed both separately and cumulatively using simulations in constant extreme ENSO states. In this way we are able to attribute ENSO effects to changes in genesis and tracks. The influence of ENSO on genesis and tracks both have signatures at landfall. While the effect of ENSO on genesis is predominantly a shift in genesis location, resulting in higher landfall rates during strong La Niña states, the effect of ENSO on track propagation varies seasonally and spatially. In August and October, there is a significant change in the mean tracks due to changes in ENSO state. In the Philippines, the combined genesis and track effects on landfall cancel out, while in Vietnam, China, Korea, and Japan, the combined effects enhance each other.

1. Introduction

There are many densely populated coastal regions that are susceptible to high fatalities and costly damages every year due to the frequent landfall of tropical cyclones (TC) that occur in the western North Pacific (WNP). Studies have shown that the El Niño/Southern Oscillation (ENSO) strongly influences TC activity in the WNP. The most important change of WNP TCs with ENSO appears to be the shift in genesis location to the southeast during strong El Niño events and the shift in genesis location to the northwest during strong La Niña events (Chan 1985, 2000; Dong 1988; Lander 1994; Saunders et al. 2000; Wang and Chan 2002; Chia and Ropelewski 2002). This shift results in changes in the tracks of the subsequent TCs: those that form in the southeast have longer lifetimes and tend to re-curve northward compared to those that form in the northwest that move straight westward into land (Wang and Chan 2002). Elsner and Liu (2003) further studied the ENSO effect on tracks and implications for landfall location, finding that strong El Niño years correspond with re-curving northward TC tracks, which are likely to make landfall on Japan, the Korean Peninsula, and northern China. During La Niña years, TC tracks move in a straighter westward path, putting the Philippines, southern China, and Vietnam at higher risk. The track type cluster analysis performed by Camargo et al. (2007b) for the WNP confirms that the different genesis regions associated with El Niño (La Niña) years are also associated with longer (shorter) tracks. Given a genesis location closer to the equator and farther eastward, El Niño year TC tracks in the WNP have more of an opportunity to reach higher intensities as they travel over the warm tropical ocean. They may also reach higher latitudes when they curve northward, before making landfall (Camargo and Sobel 2005; Chan and Liu 2004; Camargo et al. 2007b). The last two effects are important when making a landfall risk assessment in terms of landfall location and severity of the hazard.

The ENSO-track relationship has been primarily explained by shifts in genesis location. One thing that has not been examined extensively is the direct effect of ENSO on tracks. For instance, independent of genesis location, will a TC tend to move in a different direction, given different ENSO states? In this study, we investigate this effect, as well as the combined result with shifts in genesis location, in order to attribute the results on landfall. In doing so, we fill a key gap in documenting the TC-ENSO relationship and its landfall implications. As much work has been done on improving ENSO prediction (e.g., Cane 1991; Fedorov et al. 2003; Goddard et al. 2010), a fuller understanding of the ENSO-TC relationship would allow for improved long-range probabilistic predictions of TC activity (Vitart 2006; Vitart et al. 2007; Camargo et al. 2010).

Many previous studies have analyzed correlations between aspects of TC activity and climate states. For example, recent work (Kossin et al. 2007; Vecchi et al. 2008; Knutson et al. 2010) has shown that changes in TC frequency and intensity may occur with global warming. However, Weinkle et al. (2012) find that there is no trend in observed TC landfall frequency or intensity globally or for any ocean basin. They further indicate that the increasing trend in global damage is due to the upward trend in wealth on coastal areas. This leads us to first focus on developing a statistical track model that can simulate the way landfall changes with natural climate variability.

An advantage of using statistical models is their ability to translate what the TC activity-climate state relationships mean in terms of risk to humans. Observational studies have used track shape (Elsner and Liu 2003; Camargo et al. 2007a, 2007b) or track density (Wang and Chan 2002) changes as a proxy for risk of TC landfall because data become sparse when considering the only the observed landfalls on small coastal regions. Statistical models (Darling

1991; Drayton 2000; Vickery et al. 2000; James and Mason 2005; Emanuel et al. 2006; Rumpf et al. 2007; Hall and Jewson 2007; Graf et al. 2009; Yin et al. 2009; Yonekura and Hall 2011) can explicitly simulate landfalls, which are commonly used to inform insurance hazard and risk assessments.

In previous work, Yonekura and Hall (2011)—later referred to as YH11—use a statistical track model to simulate the full lifecycle of TCs in the WNP, including an ENSO-dependent genesis component. Here, we use the same model and add ENSO-dependence into the track propagation component. In YH11, the details of statistical model construction, validation, and simulation procedures are presented. The genesis component depends on ENSO using local Poisson regression of the local genesis count time series on the JASO Niño 3.4 Index. The model was able to capture the geographic characteristics of landfall in its simulations of the historical period, as well as replicate the spatial distributions of the observed track trajectories and track densities.

One important aspect that was missing from the YH11 model is the seasonality of WNP TCs. Chan (2000) has shown that the effect of ENSO on WNP TC tracks varies by month. For instance, in October of a strong El Niño event, tracks will move more northward, avoiding Japan, due to mid-level westerlies around 40°N. In the same month for a strong La Niña, it is shown that tracks move westward in a straight path at lower latitudes due to easterly mid-level wind anomalies. Chia and Ropelewski (2002) documented the seasonality in the mean genesis location in the WNP, which moves from the southeast in March (5ºN, 158ºE) to the west in June (135ºE), to the northeast in the boreal summer (17ºN), then back south-southeast in December (8ºN). The movement of the monsoon trough, especially in the peak typhoon season and also in regard to ENSO effects, explains the genesis location shift. In the Camargo et al. (2007a; 2007b) WNP

track cluster analysis, it is also shown that there the different clusters have different seasonal occurrence rates as well as different seasonal periods of positive or negative correlation with ENSO. In this study we include the effects of seasonality in the genesis and track components of our model by using seasonally varying predictors.

In the following section, we describe the methods used to incorporate ENSO-dependence into the model, run simulations, and evaluate the model uncertainty. Then, in section 3, we evaluate the model and describe the effect of ENSO on TC tracks and examine simulations to attribute track and genesis effects on landfall rates. Section 4 concludes with a summary and discussion of the results.

2. Methods

a. Data

As in YH11, the TC track data used to construct the statistical track model is from the International Best Track Archive for Climate Stewardship (IBTrACS; Knapp et al. 2010) database of 6-hourly storm positions. The storms from 1945-2007 are used for consistency with YH11. To define the state of ENSO for a given year, the Niño 3.4 Index (Barnston et al. 1997) averaged over JASO is used and will be hereafter referred to as the ENSO Index. We acknowledge the recent studies of the central equatorial Pacific warming type of ENSO—an El Niño Modoki event (Ashok et al. 2007)—and would like to distinguish here that we are considering the conventional El Niño phenomenon (eastern equatorial Pacific warming).

Seasonally varying predictors are used in both the genesis and track propagation component of the model. For the genesis component we use the monthly annual-cycle climatology of sea surface temperature (SST) from the NOAA ERSST V3 data (Smith and

Reynolds 2004), provided by the NOAA/OAR/ESRL PSD in Boulder, Colorado. The data can be found at http://www.esrl.noaa.gov/psd. In the track propagation component of the model, the 500mb daily annual-cycle climatology of zonal winds is used from the NCEP/NCAR Reanalysis years 1948-2007 (Kalnay et al. 1996). The choice of 500mb zonal winds as a predictor for the track component is motivated by Chan and Gray (1982), who studied which wind levels most influence track displacement and speed. They found that the mid-level winds (700, 600, and 500mb) have the most influence. Chan (2000) then uses 500mb wind anomalies to explain changes in WNP TC tracks associated with different ENSO phases. An alternative to choosing one wind level would be to take a weighted average of different levels to avoid issues such as the sign change in zonal winds at approximately 500mb between the Philippines and Vietnam. Here, we choose to use the 500mb as a first effort of incorporating a physics-based predictor for track propagation.

The main purpose of adding SST as a predictor in the genesis component and mid-level winds in the track propagation component is to include the effect of seasonality on WNP TCs, thus we use climatological predictors. The interaction term between the climatological predictor and ENSO Index represents any existing correlation between the two that affects the TC model component, e.g. if ENSO state affects seasonality or if the season affects the ENSO impact on TC activity. ENSO has known effects on the atmospheric circulation and sea surface temperatures (SST) in the WNP. At the mid-level troposphere, an El Niño event is associated with a cyclonic anomaly over Southeast Asia, which enhances the westerly jet along the coast (Wang et al. 2000). WNP SST, especially in 5°– 20°N, 130°–155°E, is negatively correlated with the Niño 3.4 Index though its variability is considerably less than the index region (Chan and Liu 2004). We believe that our model is still able to capture these effects on TCs indirectly.

The fact that SST and mid-level winds change during different phases of ENSO and physically affect TC activity is captured through the ENSO Index predictor. We assume the physical environmental changes are implicit in the observed TC behavior.

We choose a small number of statistical predictors for a couple of reasons. The first is to keep the model simple and interpretable without over-fitting. The second reason goes back to the purpose of the model being to estimate climatological risk. We could add predictors such as vertical wind shear, ocean heat content, and relative humidity, but they are left out to focus mainly on the large-scale climate predictors that we have better ability to predict at longer lead times.

b. Genesis

The genesis component of the model simulates the number of TCs per year and the date and formation location of each TC, all of which may be sensitive to ENSO. The total number is simulated by a random draw from a WNP-wide Poisson distribution whose rate is determined by Poisson regression of WNP-wide annual counts on the ENSO index (Sabbatelli and Mann 2007, YH11). The determination of a genesis-event's location is the same as YH11: local Poisson regression is performed using annual formation count data inside data circles whose size is determined by out-of-sample likelihood maximization. The spatial field of Poisson rates is normalized to create a 1-by-1 degree spatial probability density function (PDF), and a random draw from the PDF determines the location for each simulated TC. Further details can be found in YH11.

Compared to the genesis model of YH11, here we have added seasonality. We add the local monthly annual-cycle climatology of SST as an independent predictor variable in the regression. We randomly select a date, and the SST value of that date fixes a Poisson rate for a

formation event. Then we sample the probability and repeat until an event is realized. An ENSO-SST interaction term is also used as a predictor to account for the effect of yearly ENSO state on seasonality. Eq. (1) shows how to calculate a local Poisson rate, λ:

$$\lambda(r,y,m) = \exp\left(\beta_0(r) + \beta_1(r)\cdot ENSO(y) + \beta_2(r)\cdot SST(r,m) + \beta_3(r)\cdot ENSO(y)\cdot SST(r,m)\right), \quad (1)$$

where r stands for a grid location, y specifies a year, m specifies a month, each β is a local regression coefficient at r, ENSO(y) is the ENSO Index for year y, and SST(r,m) is the SST at location r and month m. The overall effect of shifting dominant genesis region to the southwest part of the WNP for El Niño events and northeast for La Niña events (YH11) is still present, but it is now seen to be most prominent in June-October. There are also subtle seasonal shifts in predominant genesis location that follow the seasonal cycle of mean genesis location as described in Chia and Ropelewski (2002).

c. Tracks

The track component of the model simulates the 6-hourly increment of a TC position as a function of location, date, and ENSO state. The basic methodology is identical to that described in YH11, but here we have added seasonality and ENSO dependence. Our incorporation of ENSO and seasonality is guided by the work of Chan and Gray (1982) and Chan (2000), who analyzed ENSO-track relationships month by month, and attributed the ENSO effect to anomalies in the 500mb winds. They demonstrated that the effect of ENSO on TCs in the WNP evolves through the season. Thus, as predictor variables we use the ENSO state and an annual-cycle of 500mb winds to incorporate seasonality in track propagation. The wind data comes from NCEP/NCAR Reanalysis daily climatological zonal winds interpolated to a 1-degree grid. We found the meridional winds to be insignificant as a predictor based on a Student's T-test. The

predictor is not used to avoid using a relationship with a high degree of uncertainty in the observations, which could introduce a model bias. The lack of significance may be due to the meridional displacement being governed more by TC size and latitude.

The IBTrACS 6-hourly zonal and meridional displacement values are linearly regressed locally on ENSO Index and the local 500mb wind values. The distance weight determining the locality of regression is a Gaussian kernel with a length scale of 300km. The length scale is determined objectively by out-of-sample likelihood maximization. At each 1-degree grid point, we archive values of the regression coefficients from the equations:

$$\begin{aligned}\overline{dX}(r,t) = \beta_{0x}(r) + \beta_{ENSOx}(r)\cdot ENSO(t) + \beta_{u500x}(r)\cdot u_{500}(r,t) \\ +\beta_{ENSO\cdot u500x}(r)\cdot ENSO(t)\cdot u_{500}(r,t).\end{aligned} \tag{2}$$

$$\overline{dY}(r,t) = \beta_{0y}(r) + \beta_{ENSOy}(r)\cdot ENSO(t), \tag{3}$$

where $\overline{dX}(r,t)$ and $\overline{dY}(r,t)$ are the mean displacements in the zonal and meridional directions, respectively, at grid point r and time t, ENSO(t) is the ENSO Index for the year specified by time t, and $u_{500}(r,t)$ is the 500mb zonal wind at grid point r and day specified by time t. Note that ENSO is only included as an effect for the mean track increment. In full simulations TCs propagate according to Eqs. (2) and (3) in the mean, and the residuals about the mean are modeled stochastically, as described in YH11: a bivariate anisotropic correlated normal, with lag-one autocorrelation for the standardized errors.

The resulting fields of coefficients from regression Eqs. (2) and (3) are shown in Fig. 3.1. Where the contours are color filled the coefficients are significantly different than zero at a 95% confidence level according to a Student T-test at every grid point. Fig. 3.1a shows β_{ENSOx}. The most important region for landfall consideration is the center of the negative values near 150˚E, 20˚N and 45˚N, indicating that in this high-density storm region positive (negative) ENSO tends

to enhance (inhibit) the westward motion of TCs. In this region, as well as in the rest of the basin, positive (negative) ENSO tends to inhibit (enhance) the northward motion of TCs (Fig. 3.1d). Fig. 3.1b shows β_{u500x}, which not surprisingly shows a positive relationship between the steering mid-tropospheric zonal wind and TC motion. Finally, $\beta_{\mathrm{ENSO}*u500x}$ (Fig. 3.1c) reveals some coupling between ENSO and u_{500} winds, particularly at midlatitudes. For positive (negative) ENSO the TC motion enhances (inhibits) the relationship between TC motion and the seasonal steering winds.

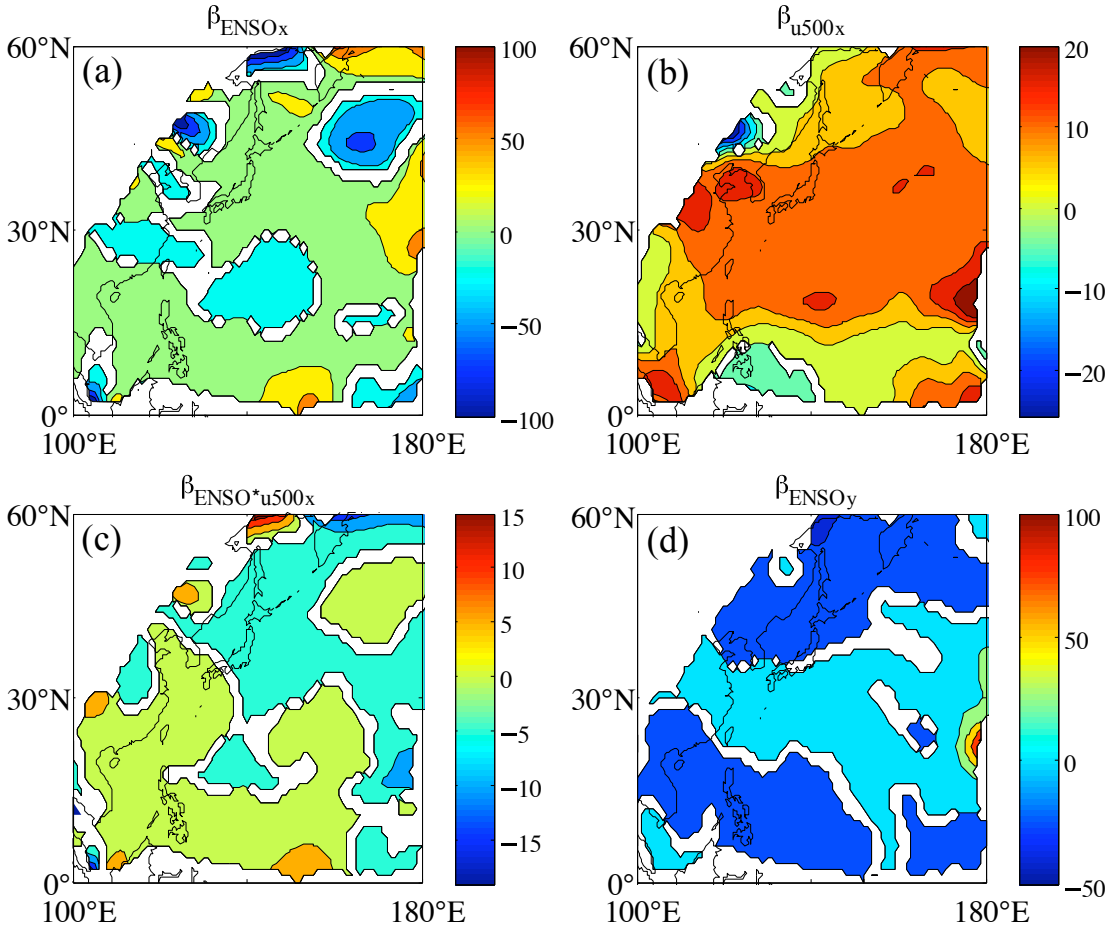

FIG. 3.1. Local regression coefficients used in the track propagation model in the zonal (x) and meridional (y) directions. White areas indicate where the regression coefficient is not significant. $\beta_{\mathrm{ENSO}x}$ and $\beta_{\mathrm{ENSO}y}$ are the coefficients that relate the mean track to current year ENSO Index. β_{u500x} relates the zonal mean track component to the climatological daily 500mb zonal winds, and $\beta_{\mathrm{ENSO}*u500x}$ accounts for the correlated components of the ENSO Index and 500mb zonal winds that explains behavior in the zonal mean track components.

d. Lysis

Lysis, or death, of each TC is determined by comparing a random uniform draw to a predetermined PDF of historical lysis probability at every track step. Land and ocean lysis is strictly separated according to a 0.25-degree land-ocean mask. See YH11 for details.

e. Simulations

Our goal is to estimate the effects of ENSO on East Asian TC landfall via genesis and track propagation. Separation of the ENSO-landfall effects via genesis and propagation is investigated by running 10,000-year simulations at stationary values of extreme ENSO Index, +2 and –2, using different model versions. The 10,000-year duration is required to converge on mean landfall rates at high-geographic resolution. The four model versions are: (1) No dependence on ENSO; (2) Genesis dependence on ENSO, "Just Genesis"; (3) Track dependence on ENSO, "Just Tracks"; and (4) Genesis and Track dependence on ENSO, "Both".

We also evaluate each of the four model versions against historical landfalls. For this purpose a separate set of simulations is performed: 500 realizations of the historical period 1945-2007 for each model version using the historical time series of the ENSO Index. The mean and spread of each ensemble is compared to the historical landfall rates. The model is unbiased to the extent that the historical landfall rates appear as a typical member of the 500-member synthetic set.

f. Uncertainty and Significance

There are two types of uncertainty to document. One is the uncertainty due to the stochastic nature of our simulations. For example, a single 1-year simulation in a +2 ENSO state will have

landfalls along the coast that differ from those of another 1-year +2 ENSO simulation, mimicking the chaotic nature of TCs. When we perform a multi-year simulation we compute the mean value of a diagnostic (e.g., landfall rate) and the spread about the mean. How well do we know the mean? We perform long simulations for a fixed ENSO state to reduce the mean's uncertainty due to finite simulation length. We find that 10,000-year simulations are required to converge on mean model landfall rates at high resolution along the coast. We cannot, however, reduce the uncertainty due to the finite historical data on which the model is constructed. This is the second type of uncertainty, and it is crucial to document this uncertainty in order to say whether the relationships we uncover between ENSO and a mean diagnostic value are significant.

In order to determine the uncertainty of a mean diagnostic value to the underlying data, we perform a generalized jackknife significance test. We reconstruct the genesis and track models 100 times, each time using a random ~80% of the IBTrACS years (50 years out of 63). For each of the 100-jackknife members we run 10,000-year simulations at extreme ENSO states and compute the mean of the diagnostic (e.g., landfall rates along the coast). We then take the difference between +2 and -2 ENSO mean values for each jackknife member. If at least 97.5% of the difference values are all positive or all negative, then we call the ENSO effect significant for that diagnostic.

3. Results

In this section we first evaluate the model by comparing simulation results in extreme ENSO states as well as historical simulations to direct observations. We then examine the impact of ENSO on WNP TC tracks and landfall, first by illustrating the ENSO effect on mean tracks, and

then by performing full stochastic simulations with landfall rates. We use three different model versions in order to isolate the effects of ENSO on landfall via genesis and tracks.

a. Model evaluation and comparison

We now evaluate the model by comparing simulation results to direct observations using two diagnostics: (1) life spans at extreme ENSO states, and (2) landfall rates over the historical period. We calculate TC life spans from IBTrACS and find an average of 9.3 days for years when the ENSO Index is greater than 1 (El Niño) and 6.8 days when the ENSO index is less than -1 (La Niña). Using the "Both" model version (ENSO-dependent tracks and genesis) we obtain a mean life span of 8.6 days during El Niño and 6.8 days during La Niña, in close agreement with the direct observations. Repeating the calculation with Just Genesis and Just Tracks model versions indicates that the ENSO dependence of genesis causes the change in life span. (Just Genesis has a mean life span of 8.3 (6.3) days for El Niño (La Niña). Just Tracks has one of 7.5 (7.7) days.) La Niña TCs originate, on average, closer to the coast and, thus, have a shorter life span before making landfall. We note that others (Wang and Chan 2002; Camargo and Sobel 2005) find the same sign in ENSO-life span change, though they use slightly different ENSO thresholds. Combining the findings of Camargo et al. (2007a; 2007b), which uses the track clustering method, the clusters that occur more during El Niño states have higher median lifetimes than our average El Niño lifetime by about 2-4 days. The median lifetime for the cluster occurring most with La Niña has almost the same value as our La Niña average.

In order to evaluate the model's landfall characteristics we perform 500 full stochastic simulations of the historical period 1945-2007. We define a landfall as when a track crosses a 100-km coastal segment from ocean to land for the East Asian regions shown in Fig. 3.2. Fig. 3.3 shows the average annual landfall rates per 100 km over the 500-member ensemble, the inner

95% spread about the mean, and the rates directly computed from IBTrACS. Landfall rates vary enormously by region, depending on the orientation of the coast with respect to mean tracks and the proximity of the coast to regions of high activity. Peak landfall rates occur in Southeast Asia, the southern China coast, and the Philippines.

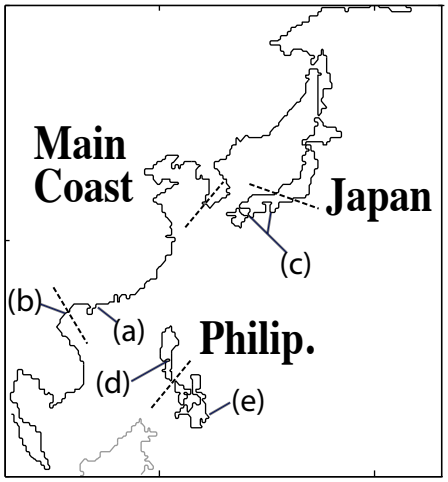

FIG. 3.2. 100-km coastline segments used in the landfall diagnostic, separated into larger regions. The dashed lines correspond to the dashed lines in Fig. 3.3, and the letters highlight the specific coastal segments where the model exhibits bias.

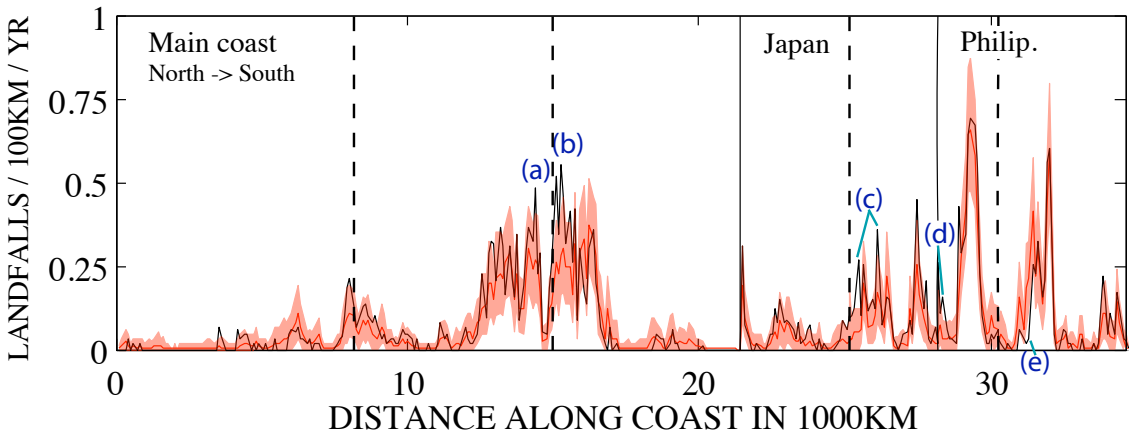

FIG. 3.3. Ensemble mean landfall rates for 100km segments along the East Asian coast (see Fig. 3.2) from simulations of the historical period (1945-2007) are shown with the solid red line. The red shading indicates the inner 95% spread of landfall rates over the 500-member ensemble. The Both model configuration was used, having ENSO-dependent genesis and tracks. Landfall rates from IBTrACS are in black. Letters indicate regions of note that correspond to the letters in Fig. 3.2.

The model is in close agreement with observed landfall rates. In most regions the historical landfall rate falls inside the 95% spread about the mean, indicating no model bias. There are, however, a few scattered regions of bias that are identified with letters on Fig. 3.3. The corresponding coastal segments are highlighted on the Fig. 3.2 map. Just north (a) and south (b) of the Vietnam-China border there are local landfall peaks where the model is biased low. Small regions of low bias also occur on the southeast coast of Japan (c) and the west coast of the northern Philippines (d). The east coast of the southern Philippines (e) displays a small region of high bias. Despite these small biases, overall the analysis confirms that the model is able to capture the geographically complex behavior of TC landfall in the WNP. Furthermore, the inclusion of ENSO reduces model bias compared to a model version with no ENSO sensitivity (not shown).

b. ENSO effect on mean tracks

We examine the modulation of TC tracks in the WNP due to ENSO by looking at mean tracks for ENSO Index values of +2 and -2. Mean tracks are the trajectory followed as a result of the local regression of Eqs. (2) and (3), without any stochastic modeling of residuals. This is, in effect, the average trajectory that a TC would follow as it moves through the basin starting from a specified location and date. We compare mean tracks that are specified to originate from the same point, to exclude the indirect influence of ENSO on tracks via shifts in genesis site.

Fig. 3.4 shows the local mean displacement vectors for opposite ENSO states at two dates. In August at low latitudes (below 15°N), El Niño (red) and La Niña (blue) vectors are nearly parallel, pointing westward, with a small northward component. The most pronounced difference is the larger vector magnitude (faster translational speed) for La Niña. In the zonal band 15-30°N El Niño and La Niña vectors are more northward oriented, but the westward

component is stronger for El Niño vectors. This westward El Niño shift corresponds to the region of negative $\beta_{\mathrm{ENSO}x}$ seen in Fig. 3.1a, and it results in El Niño tracks that are more likely to make Asian landfall. In midlatitudes the vectors point northeastward. Here, the ENSO differences in vector orientation vary spatially, but there is an overall tendency for greater magnitude (faster tracks) during La Niña. In October there is less ENSO-track difference below 20°N. The El Niño and La Niña vectors are roughly parallel, pointing northwestward, with only small differences in magnitude. The region between 20˚N and 30˚N still displays more westward pointing El Niño vectors, but its zonal extent is smaller than in August. In both months north of 30°N, vectors have a higher magnitude. TCs propagate with higher translational speed in midlatitudes. Examining observed ENSO event 500mb wind composites (not shown) for the same time of year shows some indication that the winds influence the mean track vectors especially in the mid-latitudes.

In order to better visualize the cumulative effect these space- and time-dependent ENSO dependencies we launch mean tracks of 10-day durations in +2 and -2 ENSO states from a set of fixed locations in July, August, September, and October. Figs. 3.5 and 3.6 show the tracks for August and October, respectively, while Table 3.1 in addition documents results for July and September. As a diagnostic of the ENSO effect we use the location where tracks cross lines of constant latitude and longitude. The ENSO difference in the location (degrees of latitude or longitude) is deemed to be significant or not according to our jackknife uncertainty tests described above. An asterisk by the genesis point in each figure indicates that the ENSO effect is significant at the 90% confidence level. Fig. 3.7 provides examples of the jackknife test for the case of an insignificant ENSO effect and a significant ENSO effect.

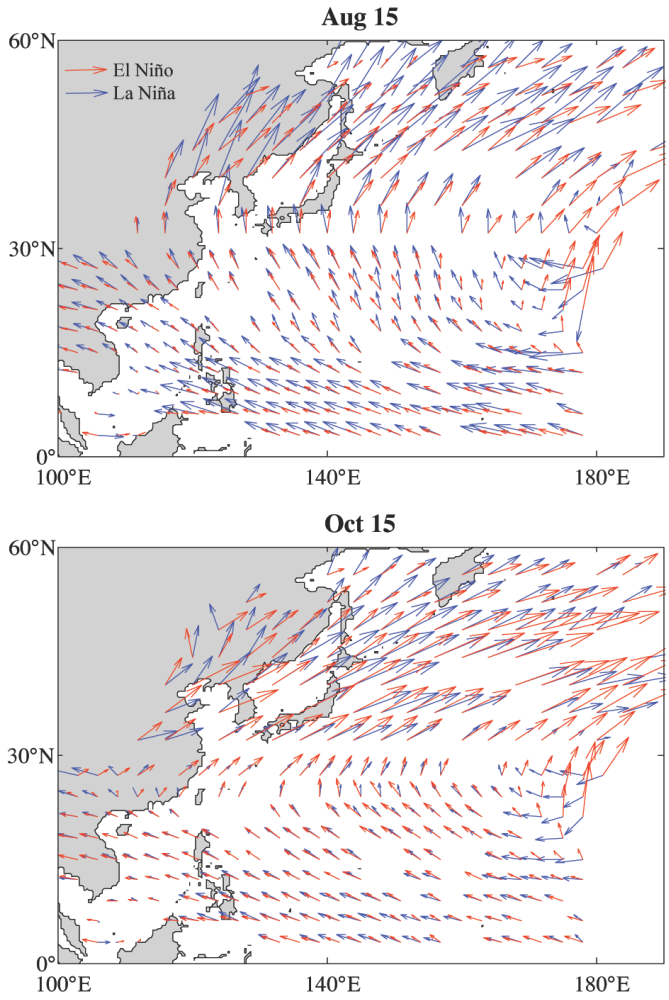

FIG. 3.4. Local mean track displacement vectors for ENSO Index values of 2 (red) and -2 (blue) shown for two different dates, August 15 and October 15, which provide different inputs for climatological daily 500mb zonal winds. Vectors are only shown where the local regression coefficients are significant.

TABLE 3.1. Mean track significance testing results for each genesis point and starting date. An "M" signifies that the mean track shift from opposite ENSO states was significant for a starting date on the fifteenth day of the given month. An "F" signifies the same but for a starting date on the first day of the month.

	GENESIS POINT										
	1	2	3	4	5	6	7	8	9	10	11
JUL	MF	F				#				#	M
AUG	F	F		*	M		MF				M
SEP	F	*	*				F				
OCT	*	*	*	M	*		F				

These 10-day tracks can be divided into two broad categories, those that re-curve, ultimately heading northeastward, and those that remain on a comparably straight northwestward trajectory. We find that both track categories occur in both ENSO states, and that there is little variation from one category to another through the season from a given genesis site. Genesis points 1-5 had straight-moving tracks through the whole season, while genesis points 6-11 had re-curving tracks through much or all of the season. The only variations occurred for genesis points 6 and 10, which had straight-moving tracks in July and re-curving tracks in August through October.

ENSO influences the trajectory of both the straight-moving and re-curving tracks. We summarize this influence by the shift with ENSO of the latitude that tracks cross specified lines of longitude and the longitude that tracks cross specified lines of latitude, as shown in Figs. 3.5 and 3.6. The sign of mean-track shifts with ENSO changes through the season for the straight-movers, but stays constant for re-curving tracks. The ENSO shift for straight-moving tracks from genesis points 1-5 (Figs. 3.5 and 3.6) reverses from August to October: in August, El Niño (La Niña) mean tracks move more westward (eastward) and northward (southward), and the effect reverses in October. However, most of the shifts of either sign are insignificant. Most of the re-curving mean tracks from genesis points 6-11 propagate farther westward during El Niño before re-curving. However, it is only tracks from points 7 and 11 whose shifts are significant.

The straight-moving tracks pose the biggest landfall threat on the Philippines, Vietnam, and southern China. The shifts with ENSO result in changes in landfall location within these regions. However, the ENSO effect reverses throughout the season resulting in some cancellation of the net annual ENSO-track influence for these tracks. Re-curving tracks threaten the coasts of

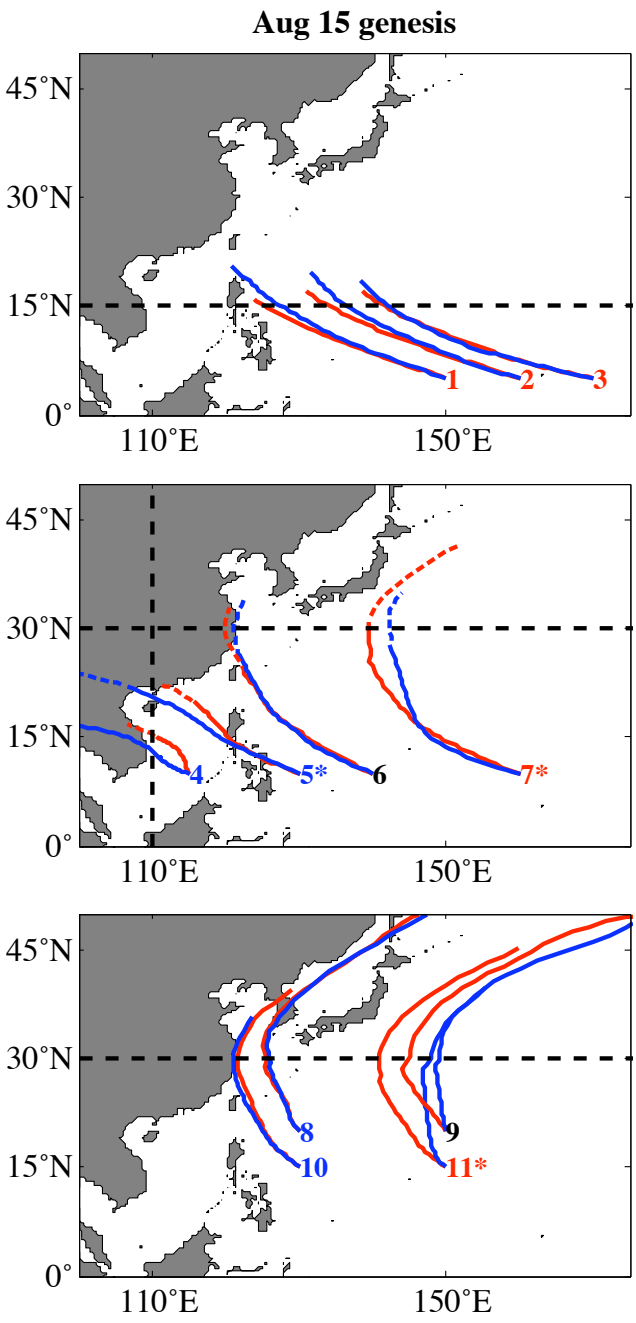

FIG. 3.5. Mean tracks initiated on August 15 from numbered genesis locations with ENSO Index of 2 (red lines) and -2 (blue lines) for extreme El Niño and La Niña years, respectively. The dashed portions of the red and blue lines indicate where the 40-step mean tracks were extended in order to reach the diagnostic line. The dashed black lines are used for a diagnostic that measures the difference in crossing location between ENSO states. The asterisks by genesis point numbers indicate that the resulting mean tracks have a significant shift when they cross the black dashed line, and the number colors indicate whether the genesis site is more likely to occur during an El Niño (red) or La Niña (blue) year.

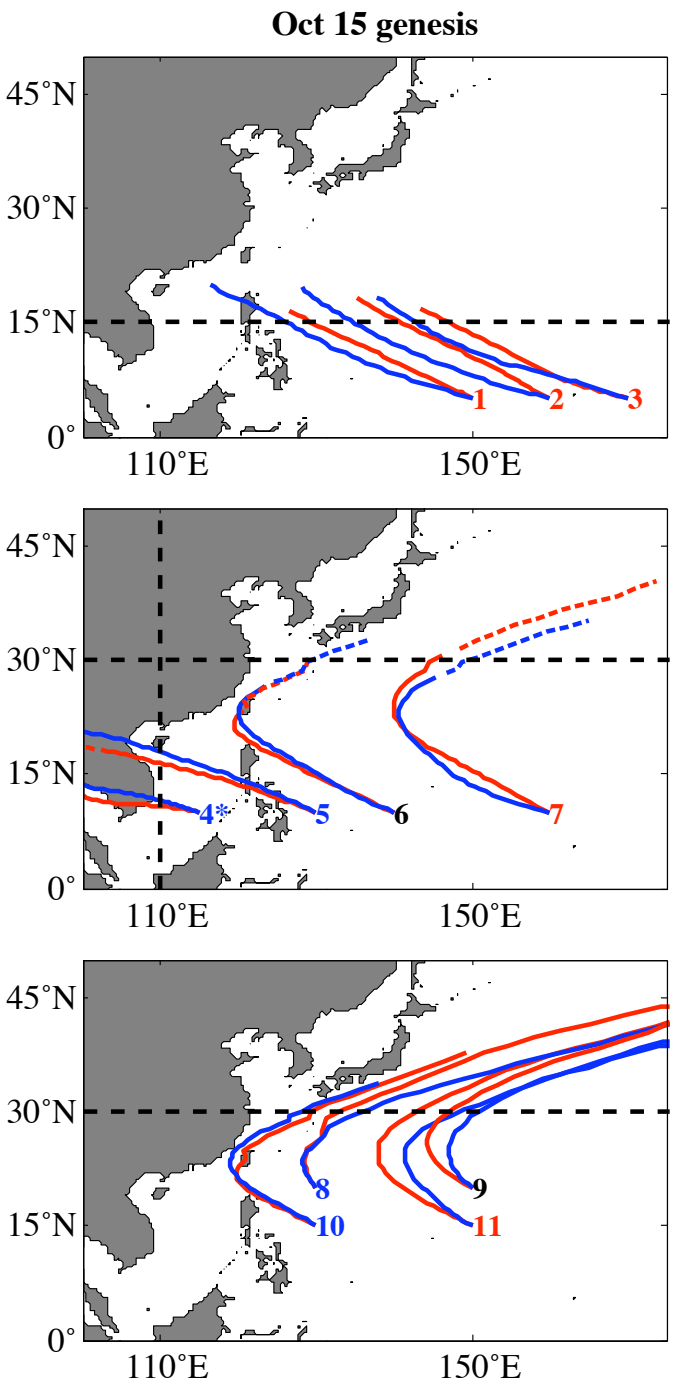

FIG. 3.6. As in Fig. 3.5 but with TCs initiated on October 15.

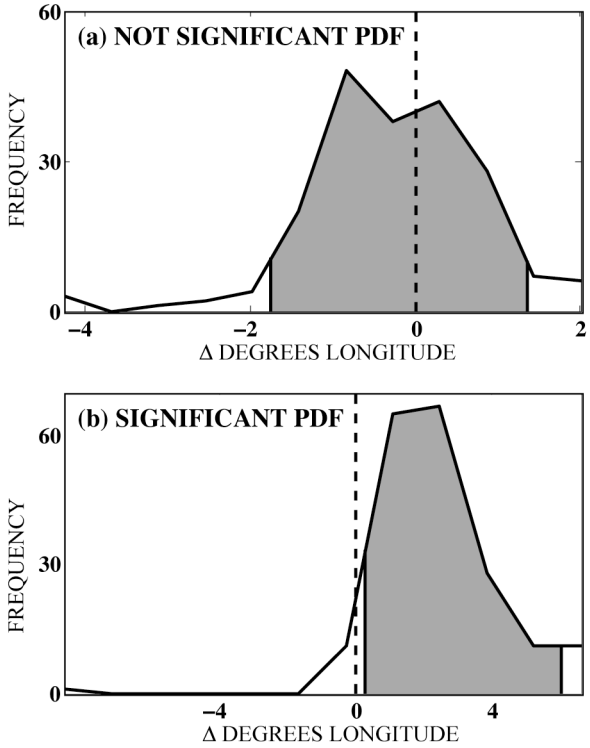

FIG. 3.7. Illustration of the significance test for the mean track shift when comparing two extreme ENSO states. (a) The distribution of mean track crossing location differences from a genesis site that results in an insignificant track shift: the inner 90% spread bounds zero. (b) A similar distribution from another genesis site that produces a significant track shift.

Japan, Korea, and northern China. The El Niño westward shift of re-curvature point enhances the chance of a landfall.

Before running full stochastic simulations, we first consider the combined landfall effect of ENSO on genesis and tracks by using the mean tracks and the known shift in genesis region. On Figs. 3.5 and 3.6, genesis points 1, 2, 3, 7, and 11 have a higher likelihood of genesis during an El Niño year (indicated by red numbers), while genesis points 4, 5, 8, and 10 have a higher likelihood during a La Niña year (blue numbers) determined from Fig. 3.11 in YH11. Looking at combined effects by following the red (blue) tracks for likely El Niño (La Niña) genesis points, results are similar to those of Elsner and Liu (2003): landfall rates increase in the northern Philippines and Japan during an El Niño and increase on Vietnam, China, Korea, and the Philippines during La Niña.

c. ENSO and landfall rates

We now turn to landfall rates using the fully stochastic model. As shown by YH11, the Just Genesis model produces higher landfall rates everywhere along the coast during La Niña (Fig. 3.8a). The effect of genesis-ENSO on landfall rates is most pronounced on the Main Coast near the China-Vietnam border, where there are higher landfall rates during La Niña (blue) than El Niño (red). The result is expected; the region of primary genesis is shifted to the northeastern WNP during La Niña, closer to the coast. The genesis-ENSO effect is less pronounced for regions of low landfall rates, such as Indonesia/Malaysia and Kamchatka (not shown).

The Just Tracks model shows more spatially varied ENSO effects at landfall (Fig. 3.8b). The ENSO-track effect is similar to the ENSO-genesis effect for southern China, Vietnam and the northern Philippines, having higher rates during La Niña. However, Japan, the southern Philippines, and Thailand have higher rates during El Niño, with the most pronounced increase in the Philippines. There is no longer a difference in Korea and northern China. Furthermore, landfall rates overall are higher using Just Tracks than Just Genesis.

The landfall rates resulting from the inclusion of both track- and genesis-ENSO effects (the Both model) closely resemble those of the Just Genesis model. Fig. 3.8c shows that the ENSO effect on China, Vietnam, and the northern Philippines is enhanced due to the genesis and track effects combining. There is a less pronounced effect on Japan and little effect on the low-landfall regions. For the southern Philippines, there is virtually no difference between ENSO states, showing that the track effect offsets the genesis effect for this area. The red and blue shading show the 95% confidence, or uncertainty, on the mean landfall rates from the generalized jackknife significance test. In nearly all regions, the jackknife uncertainty overlaps for the two ENSO states.

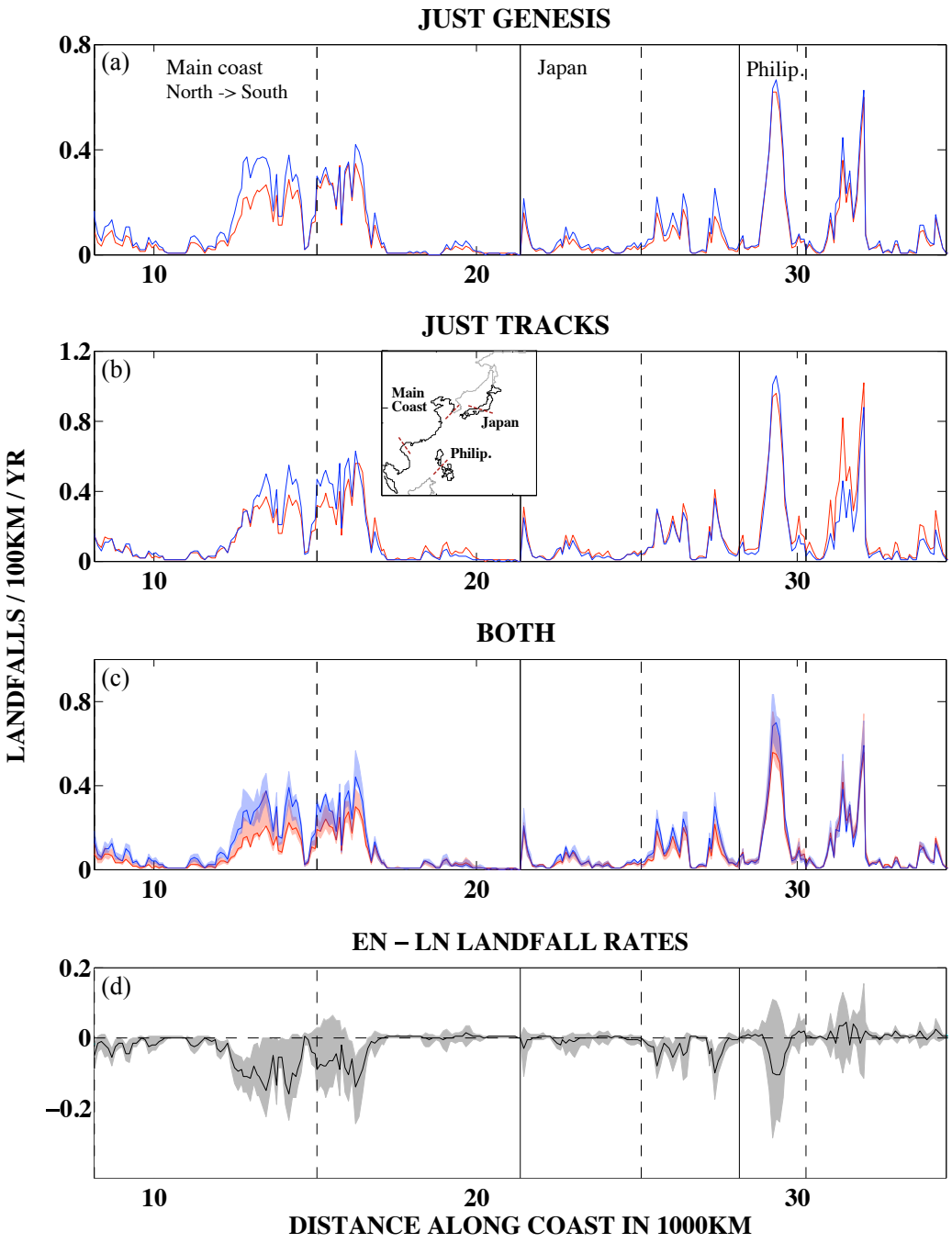

FIG. 3.8. Ensemble mean landfall rates along the East Asian coast for 1-year model runs at extreme ENSO states, ENSO Index of 2 (red) and -2 (blue). The analyzed regions are indicated in black on the panel (b) inset. Each panel represents a different model configuration: (a) Just Genesis, only ENSO dependence in the genesis component; (b) Just Tracks, only ENSO dependence in the track propagation component; (c) Both, ENSO dependence in both and shading indicates the jackknife uncertainty at the 95% confidence level. (d) The difference between ENSO states' landfall rates from the Both model with shading to indicate the jackknife uncertainty for the difference.

To further examine the significance of the ENSO effect for the Both model, the difference in landfall rates from El Niño to La Niña is plotted in Fig. 3.8d, including the jackknife uncertainty of this difference. The regions where the uncertainty excludes zero have a significant ENSO effect to 95% confidence level. Korea, parts of southern China, part of Vietnam, and southern Japan meet this condition. In these regions we can say with 95% confidence that there are more landfalls on average in La Niña than El Niño. These results differ slightly from Saunders et al. (2000), who use a different type of statistical model to determine the ENSO effect on East Asian landfall. They find that the only significant difference is an increase in landfall for La Niña that occurs in the Philippines (around Manila) and Vietnam. The former contrasts with our result, though it is in an area where our model exhibits a low bias. Saunders et al. (2000) also find an increase in landfall on Japan for El Niño and an increase in landfall on South Korea for La Niña, though it is not a significant change.

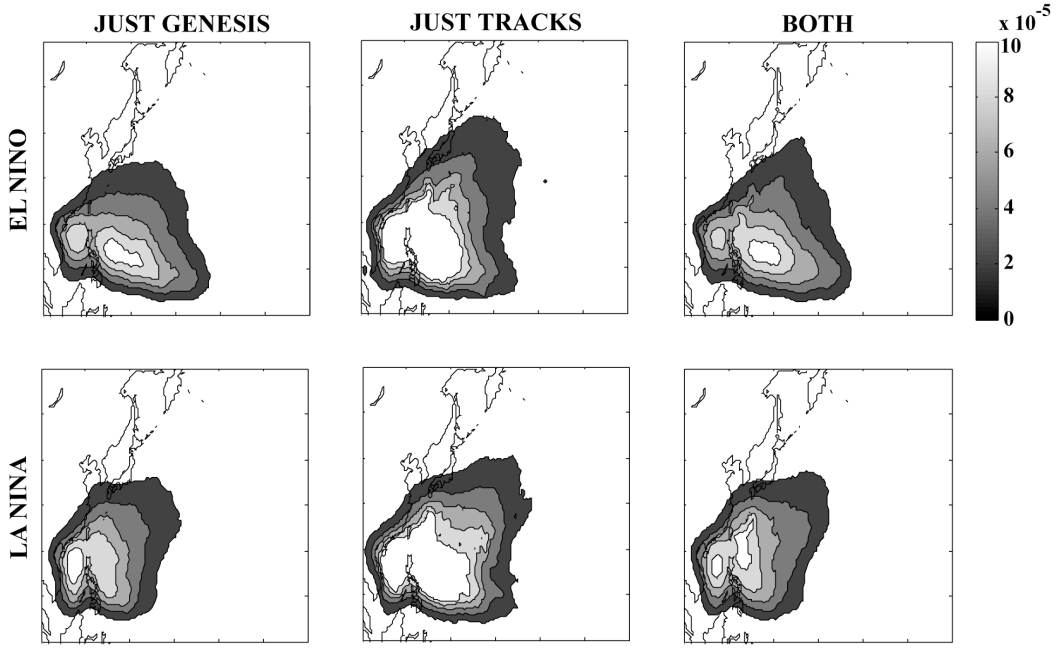

FIG. 3.9. Track densities in units of 6-hourly track points per square kilometer for the three different versions of the model at the two different extreme ENSO states. Note the effects of the genesis region shift for the Just Genesis and Both versions and the high track density in the South China Sea for the Just Tracks version that agrees with the higher landfall rates in simulations.

We now examine track density to help interpret these landfall-ENSO results. We define density as the number of 6-hour track points per unit area, calculated by counting the track points in every 1-degree grid box. The track densities for the two ENSO states for each version of the model at are shown in Fig. 3.9. The results show large similarities between the simulations from the Just Genesis and Both model versions: the southeastern peak in density during El Niño moves to the northwest during La Niña. This shift in track density is consistent with the increased La Niña landfall rates on Vietnam, China, Korea, and Japan seen in Fig 8. This density shift is consequence of shifting genesis regions, and is not observed in the Just Tracks model. However, the Just Tracks model shows higher track density overall in either ENSO state, with a notable northward increase in track density, especially during El Niño states.

4. Discussion

We have constructed a statistical track model for TCs in the WNP with seasonal- and ENSO-dependence in the genesis and track-propagation components with the goal of estimating the ENSO influence on Asian landfall rates. The model implements local regression using seasonally varying climate variables and the JASO Niño3.4 Index as predictors. The advantage of a basin-wide track model such as this compared to analysis of landfalls directly is that it brings to bear orders of magnitude more data to landfall estimation, essentially projecting information from the entire basin onto coastal regions of interest and climate states of interest.

Stochastic simulations of TCs in extreme ENSO states reveal that ENSO affects landfall locations and rates. We compute mean landfall rates and uncertainties about the means for strong El Niño and La Niña states. There are significantly higher landfall rates in Korea southern China, Vietnam, and southern Japan during La Niña. The majority of the ENSO-landfall relationship is mediated by the influence of ENSO on genesis rates and geographic distribution. However,

ENSO influence on TC tracks adds to, and subtracts from, the genesis-landfall effect in various coastal regions.

We also evaluate the model by comparing simulated landfall rates to direct historical landfalls. Overall, the model performs well; in most regions historical landfall rates fall inside the spread of model results across large ensemble simulations, indicating a lack of bias. There are a few regions where the model has biased landfall rates. These biases have been reduced, however, compared to the YH11 model version, which had no seasonality and no ENSO-track effects.

Future directions for this work include developing a model component for the intensity and size of each TC, similar to Vickery and Twisdale (1995) and Vickery et al. (2000), in order to make a more complete risk analysis. Studies such as Irish et al. (2008) and Weisberg and Zheng (2006) show that it is the complex relationship between factors such as translational speed, storm size, intensity, bathymetry, and orientation that determines damage. Further, modeling of other TC-climate relationships may also be explored in the future where the model is dependent on other climate states such as the Madden-Julian Oscillation or other TC-favoring climate conditions.

References

Ashok, K., S. K. Behera, S. A. Rao, H. Weng, and T. Yamagata, 2007: El Niño Modoki and its possible teleconnection. *J. Geophys. Res.*, **112**, C11007.

Barnston, A. G., M. Chelliah, and S. B. Goldenberg, 1997: Documentation of a highly ENSO-related SST region in the equatorial Pacific. *Atmos.-Ocean*, **35**, 367-383.

Camargo, S.J. and A.H. Sobel, 2005: Western North Pacific tropical cyclone intensity and ENSO. *J. Climate,* **18**, 2996-3006.

Camargo, S.J., K.A. Emanuel, and A.H. Sobel, 2007a: Use of a genesis potential index to diagnose ENSO effects on tropical cyclone genesis. *J. Climate*, **20**, 4819-4834.

Camargo, S.J., A.W. Robertson, S.J. Gaffney, P. Smyth, and M. Ghil, 2007b: Cluster analysis of typhoon tracks. Part II: Large-scale circulation and ENSO. *J. Climate*, **20,** 3654–3676.

Camargo, S.J., A.H. Sobel, A.G. Barnston, and P.J. Klotzbach, 2010: The influence of natural climate variability, and seasonal forecasts of tropical cyclone activity. In: J.C.L. Chan and J.D. Kepert (Eds.), *Global Perspectives on Tropical Cyclones: from Science to Mitigation, 2nd edition*, pp. 325-360, World Scientific.

Cane, M.A., 1991: Forecasting El Niño with a geophysical model. In: M.H. Glantz, R.W. Katz, and N. Nicholls (Eds.), *Teleconnections Linking Worldwide Climate Anomalies,* pp. 345-370, Cambridge University Press, Cambridge, UK.

Chan, J.C.L., 1985: Tropical cyclone activity in the Northwest Pacific in relation to the El Nino / Southern Oscillation phenomenon. *Mon. Wea. Rev.,* **113**, 599-606.

Chan, J.C.L., 2000: Tropical cyclone activity over the western North Pacific associated with El Niño and La Niña Events. *J. Climate*, **13**, 2960-2972.

Chan, J.C.L. and W. M. Gray, 1982: Tropical cyclone movement and surrounding flow relationships *Mon. Wea. Rev.*, **110**, 1354-1374.

Chan, J.C.L. and K.S. Liu, 2004: Global warming and western North Pacific typhoon activity from an observational perspective. *J. Climate*, **17**, 4590-4602.

Chia, H.-H. and C.F. Ropelewski, 2002: The interannual variability in the genesis location of tropical cyclones and the northwest Pacific. *J. Climate*, **15**, 2934-2944.

Darling, R., 1991: Estimating probabilities of hurricane wind speeds using a large-scale empirical model. *J. Climate,* **4**, 1035-1046.

Dong, K., 1988: El Niño and tropical cyclone frequency in the Australian region and northwest Pacific. *Aust. Meteor. Mag.*, **36**, 219-255.

Drayton, M., 2000: A stochastic basin-wide model of Atlantic hurricanes, *Proc. 24th Conf. on Hurricanes and Tropical Meteorology*, Ft. Lauderdale, FL, Amer. Meteor. Soc. 17A.3.

Elsner, J.B. and K.B. Liu, 2003: Examining the ENSO-Typhoon Hypothesis. *Climate Research*, **25**, 43-54.

Emanuel, K., S. Ravela, E. Vivant, and C. Risi, 2006: A statistical deterministic approach of hurricane risk assessment. *Bull. Amer. Meteor. Soc.*, **87(3)**, 299-314.

Fedorov, A. V., S. L. Harper, S. G. Philander, B. Winter, and A. Wittenberg, 2003: How predictable is El Niño? *Bull. Amer. Meteor. Soc.*, **84,** 911–919.

Goddard, L., Y. Aichellouche, W. Baethgen, M. Dettinger, R. Graham, P. Hayman, M. Kadi, R. Martiniez, and H. Meinke, 2010: Providing seasonal-to-interannual climate information to risk management and decision-making, *Procedia Environ. Sci.* 1:81-101.

Graf, M., K. Nishijima, and M. H. Faber, 2009: A probabilistic typhoon model for the Northwest Pacific region. *Proc. The 7th Asian-Pacific Conf. on Wind Engineering*, Taipei, Taiwan, International Assoc. for Wind Eng., M2-B.

Hall, T.M. and S. Jewson, 2007: Statistical modeling of North Atlantic tropical cyclone tracks. *Tellus*, **59A**, 486-498.

Irish, J. L., D. T. Resio, and J. J. Ratcliff, 2008: The influence of storm size on hurricane surge, *J. Phys. Oceanogr.*, **38**, 2003–2013.

James, M.K. and L.B. Mason, 2005: Synthetic tropical cyclone database. *J. Waterway, Port, and Ocean Eng.*, **131(4)**, 181-192.

Kalnay, E., and Coauthors, 1996: The NCEP/NCAR 40-Year Reanalysis Project. *Bull. Amer. Meteor. Soc.*, **77**, 437–471.

Knapp, K. R., M. C. Kruk, D. H. Levinson, H. J. Diamond, and C. J. Neumann, 2010: The International Best Track Archive for Climate Stewardship (IBTrACS): Unifying tropical cyclone best track data. *Bull. Amer. Meteor. Soc.*, **91**, 363-376.

Knutson, T. R., and Coauthors, 2010: Tropical cyclones and climate change. *Nat. Geosci.,* **3,** 157–163.

Kossin, J. P., K.R. Knapp, D.J. Vimont, R.J. Murnane, and B.A. Harper, 2007: A globally consistent reanalysis of hurricane variability and trends. *Geophys. Res. Lett.*, **34**, L04815.

Lander, M., 1994: An exploratory analysis of the relationship between tropical storm formation in the Western North Pacific and ENSO. *Mon. Wea. Rev.*, **114**, 1138-1145.

Rumpf, J., H. Weindl, P. Höppe, P. E. Rauch, and V. Schmidt, 2007: Stochastic modeling of tropical cyclone tracks. *Math. Meth. Oper. Res.,* **66(3)**, 475-490.

Sabbatelli, T.A. and M.E. Mann, 2007: The influence of climate state variables on Atlantic Tropical Cyclone occurrence rates. *J. Geophys. Res.,* **112**, D17114.

Saunders, M.A., R.E. Chandler, C.J. Merchant, and F.P. Roberts, 2000: Atlantic hurricanes and NW Pacific typhoons: ENSO spatial impacts on occurrence and landfall. *Geophys. Res. Lett.*, **27**, 1147–1150.

Smith, T. M. and R. W. Reynolds, 2004: Improved extended reconstruction of SST (1854-1997). *J. Climate*, **17**, 2466-2477.

Vecchi, G. A., K. L. Swanson, and B. J. Soden, 2008: Whither hurricane activity? *Science*, **322**, 687–689.

Vickery, P.J. and L.A. Twisdale, 1995: Wind field and filling models for hurricane wind-speed predictions. *J. Struct. Eng.*, **121**, 1700-1709.

Vickery, P.J., P.F. Skerlj, and L.A. Twisdale, 2000: Simulation of hurricane risk in the US using an empirical track model. *J. Structural Eng.,* **126**, 1222-1237.

Vitart, F., 2006: Seasonal forecasting of tropical storm frequency using a multi-model ensemble. *Quart. J. Roy. Meteor. Soc*., **132**, 647.

Vitart, F., M.R. Huddleston, M. Déqué, D. Peake, T.N. Palmer, T.N. Stockdale, M.K. Davey, S. Ineson, and A. Weisheimer, 2007: Dynamically-Based Seasonal forecasts of Atlantic Tropical - Storm Activity issued in June by EUROSIP, *Geophys. Res. Lett*. **34**, L16815.

Wang, B. and J.C.L. Chan, 2002: How strong ENSO events affect tropical storm activity over the western North Pacific. *J. Climate*, **15**, 1643-1658.

Wang, B., R. Wu, and X. Fu, 2000: Pacific–East Asian Teleconnection: How Does ENSO Affect East Asian Climate?. *J. Climate*, **13**, 1517–1536.

Weinkle, J., R. Maue, and R. Pielke, Jr., 2012: Historical global tropical landfalls. *J. Clim*. doi:10.1175/JCLI-D-11-00719.1, in press.

Weisberg, R. H. and L. Zheng, 2006: Hurricane storm surge simulations for Tampa Bay. *Estuaries Coasts*, **29**, 899–913.

Yin, J., M. B. Welch, H. Yashiro, and M. Shinohara, 2009: Basinwide typhoon risk modeling and simulation for western North Pacific basin. *Proc. The 7th Asian-Pacific Conf. on Wind Engineering*, Taipei, Taiwan, International Assoc. for Wind Eng., M2-B.

Yonekura, E. and T.M. Hall, 2011: A statistical model of tropical cyclone tracks in the western North Pacific with ENSO-dependent cyclogenesis. *J. Appl. Meteor. Climatol.*, **50**, 1725-1739.

Chapter 4:

U.S. Hurricanes and Economic Damage: An Extreme Value Perspective

Emmi Yonekura[1], Daniel Chavas[2], Christina Karamperidou[3], Nicholas Cavanaugh[4], and Katherine Serafin[5]

[1] Department of Earth and Environmental Sciences, Columbia University, New York, New York, U.S.A.

[2] Program in Atmospheres, Oceans, and Climate, Massachusetts Institute of Technology, Cambridge, Massachusetts, U.S.A.

[3] Department of Earth and Environmental Engineering, Columbia University, New York, New York, U.S.A.

[4] Scripps Institution of Oceanography, University of California San Diego, La Jolla, California, U.S.A.

[5] College of Earth, Ocean and Atmospheric Sciences, Oregon State University, Corvallis, Oregon, U.S.A.

Expanded from a paper published in *Natural Hazards Review,*
doi: 10.1061/(ASCE)NH.1527-6996.0000102, 2012

Abstract

The historical record of U.S. hurricane damage is analyzed using a Peaks-Over-Threshold approach, in which the Generalized Pareto Distribution (GPD) is applied to model excesses above a specified threshold for a given damage metric. In addition to absolute hurricane damages, we define a Damage Index as the ratio of base-year economic damages to the available economic value in the affected region. We then incorporate physical covariates at the individual hurricane level into the GPD model, namely maximum wind speed and a simple yet novel measure of the mean bathymetric slope at landfall, and apply our analysis to both the Total Damage and the Damage Index.

The parameters of the GPD models with physical covariates are estimated with Maximum Likelihood Estimation. We find that for Total Damage the only useful covariate is maximum wind speed. However, for Damage Index both the mean bathymetric slope and maximum wind speed are found useful, with coefficients that are consistent with the known physics of each covariate in causing damage. Moreover, inclusion of covariates in the Damage Index reduces the maximum likelihood estimate of the shape parameter to zero, transforming the fat tail for the distribution of Total Damage to a skinny tail for the distribution of Damage Index. These results suggest that damage measured as a fraction of estimated potential damage may help to remove the local economic signal from the damage database, leaving a dataset that better captures the physical relationship between hurricanes and damage.

Finally, as an illustrative example of the potential utility of this new methodology within a risk assessment framework, we apply it first to datasets of simulated hurricane tracks corresponding to current and future IPCC A1b-scenario climate states as modeled by two different climate models: GFDL CM2.0 and ECHAM5. Secondly, we apply it to synthetic hurricanes from a model driven by variations in relative sea surface temperature.

Preface

Chapter 4 is expanded from a group project and paper with four collaborators from the NCAR ASP Summer Colloquium in 2011 on Statistical Assessment of Extreme Weather Phenomena under Climate Change. My personal contribution includes initial literature and software review, processing the raw economic damage data (including spot-checking landfall data between databases), extracting all landfall data from observations and climate models, and contributions to the model fitting. The analysis on the synthetic tracks from the fully statistical track model was all completed independently as an addition to the previously published analysis.

1. Introduction

Landfalling U.S. hurricanes are responsible for seven of the top ten costliest insured property losses due to natural disasters worldwide since 1980 (Munich Re 2011). Despite a projected decrease in the overall number of hurricanes globally, the potential for increases in the frequency and intensity of the strongest hurricanes due to climate change (Knutson et al. 2010) has raised concerns about similar increases in total economic damage in the future (Mendelsohn et al. 2012; Peduzzi et al. 2012). Moreover, 50% of total economic damage due to hurricanes in the United States during the period 1870-2005, normalized for changes in population, wealth, and in population, was caused by only eight storms (Pielke Jr. et al. 2008). Thus, our understanding of how damages may change in the future is largely predicated upon a proper accounting of the most extreme events in the landfall distribution.

The above facts have motivated recent work applying extreme value theory to historical hurricane damages with two primary foci: (a) finding appropriate models for total economic damage from hurricanes, and (b) linking total economic damage to large-scale climate signals that are known to affect Atlantic hurricane intensity and frequency. Katz (2002) employed a

compound Poisson process for the total economic damage associated with hurricanes and included the state of the El Niño-Southern Oscillation (ENSO) as a covariate. Jagger et al. (2008) and Jagger et al. (2010) utilized hierarchical Bayesian models to generate forecasts of annual insured losses, using pre-season index values of the North Atlantic Oscillation, Atlantic sea surface temperature (SST), and ENSO as predictors. While forecasting the distribution of total losses based on climatic precursors is of interest, the sensitivity of annual damages to individual extreme events implies that estimating the risk of extreme losses is more crucial for financial planning (Jaffee et al. 2008). To that end, Jagger et al. (2008) and Jagger et al. (2010) demonstrated that the family of Generalized Pareto Distributions (GPDs) is appropriate for modeling extreme events involving large economic losses such as hurricane landfalls.

To date, however, GPD analysis of hurricane damage that incorporates physical variables at the individual hurricane level has not been performed. Hurricanes inflict damage primarily via two mechanisms: wind damage to structures both directly as well as indirectly due to windborne debris impact (Lin et al. 2010), and water damage due to storm surge and precipitation (Iman et al. 2005; Rogers et al. 2009). The former is a function of the wind field, while the latter is a more complex function of the wind and pressure fields as well as near-coast bathymetry, storm translation speed, storm track and landfall angle (Irish et al. 2008; Tuleya et al. 2007). Inland flooding is additionally sensitive to both inland topography and to the magnitude and direction of vertical wind shear in the vicinity of the storm (Lonfat et al. 2007).

Furthermore, previous research has analyzed absolute damages normalized to 2005 dollars as calculated in Pielke Jr. et al. (2008) (e.g., Nordhaus 2010, Bouwer and Botzen 2011, Mendelsohn et al. 2011). However, given the large variation in economic value along the coast, analysis of absolute damage data may confound the relative roles of physical storm

characteristics and economic value at landfall in damage attribution, particularly at the extremes. As a remedy, one may instead analyze the ratio of the base-year (e.g., non-normalized) damages to an estimate of the total economic value of the region affected by the hurricane (e.g., the fraction of "available" economic value that is destroyed by the storm. This quantity, defined herein as the Damage Index and described in more detail below, is a measure of the physical "damage capacity" of a storm that seeks to remove variability in economic value at the landfall location from the damage database. Such an approach was first introduced in the context of all natural disasters at a global scale by Neumayer and Barthel (2011) and preliminarily in the context of hurricanes in an alternate form by Maina (2010).

This work seeks to fit GPD models to both absolute damages (hereafter "Total Damage") and the Damage Index using the maximum hurricane wind speed at landfall (V_{max}) and the mean slope of the continental shelf ($\bar{s}$) as covariates. Storm size, as measured by the radius of 34-knot winds (r_{34}), was also tested but lacks sufficient data in the historical record to warrant inclusion in the final analysis. This methodology is applied to both Total Damage and the Damage Index and the results are compared. Based on this comparison, we argue that, for the purposes of GPD analysis of hurricane damages, the Damage Index is a more suitable metric for the relationship between the physical characteristics of a given landfalling hurricane and the damage that it produces. We then illustrate the potential utility of this approach to assess the probability of extreme losses given historical data as well as synthetic data based on climate model projections.

This paper is organized as follows: After an account of the datasets used and their limitations, we develop the economic Damage Index approach and discuss its relation to the Total Damage. We fit GPD models of the Damage Index without and with physical covariates, and we compare the results to the corresponding models of the Total Damage. Finally, as an

illustration of the potential utility of this approach, we apply the Damage Index model to synthetic hurricane data in varying climate conditions from different models. Summary and conclusions close the paper.

2. Data

Economic damage data (in both base-year and 2005 dollars normalized based on population), household data in affected coastal counties for U.S. landfalling hurricanes (1900-2004), and annual national wealth data are taken from the analysis of Pielke Jr. et al. (2008). It should be noted that their analysis examines damages from individual hurricanes, but we are interested in individual landfall events. For our analysis, we use their disaggregated data for each landfall. Economic damages are defined as the direct losses as determined in the weeks or months after the hurricane landfall, and are often estimated based on the reported insured damages (typically taken as a 2:1 ratio since at least 1987). These damage estimates may therefore be attributed to wind, storm surge, and inland flooding. To our knowledge, a dataset of damages disaggregated by hazard type is not publicly available. Annual county household data were updated from the work of Collins and Lowe (2001) and are taken from the U.S. Census Bureau decadal survey database linearly interpolated to the year of interest.

Due to the lack of a single unambiguous landfall, the following storms are excluded: 1909 Storm 10, 1944 Storm 7, 1962 Daisy, 1965 Debbie, 1988 Beryl, and 1988 Gilbert. Due to a lack of disaggregated economic data, the following landfalls are excluded: 1960 Donna landfalls 2 and 3, 1979 David landfalls 1 and 2, and 1985 Gloria landfalls 1 and 2. Of these 12 excluded landfalls, three have normalized damages exceeding 1 billion USD, though only one exceeds 3 billion USD (1944 Storm 7: 13 billion USD, rank = 21). The result is a final dataset of 202 individual landfall events during the period 1900-2004.

Bathymetric data is extracted as grids with 30 arc second resolution from the SRTM30_PLUS v6.0 data via the SCRIPPS Institution of Oceanography's satellite geodesy research group and is based on a gravity-to-topography ratio calibrated using the Smith and Sandwell global 1-minute grid altimetry data and 298 million edited soundings (Becker et al. 2009). Landfall locations are extracted from the HURDAT Best Track dataset (Jarvinen et al. 1984), modified slightly to account for a significant change in the wind-pressure relationship used by the National Hurricane Center in 1970 (Landsea 1993; data and documentation from Kerry Emanuel: ftp://texmex.mit.edu/pub/emanuel/HURR/tracks/). An automated algorithm combines Best Track data with a coastal map database to objectively determine landfall locations, and each location is subsequently verified manually. Maximum 1-minute near-surface hurricane wind speed at landfall is taken to be the final 6-hourly value prior to landfall.

Synthetic hurricane tracks downscaled from various climate backgrounds are generated from two different hurricane models described here.

a. Statistical-deterministic hurricane model

In Section 5a, we analyze current and future climate hurricane track datasets that are generated by a statistical-deterministic hurricane model (Emanuel et al. 2006) downscaled from current (1981-2000) and future (2081-2100) IPCC AR4 A1b scenario (Nakicenovic et al. 2000) climates as simulated by the Geophysical Fluid Dynamics Laboratory (GFDL) CM2.0 model (Delworth et al. 2006) and the European Center/Hamburg Model 5 (ECHAM5; Roeckner et al. 2003).

This statistical-deterministic model has the aim of basing synthetic hurricanes on known hurricane physics while incorporating some stochastic elements. Hurricane genesis is determined by vortex seeding over the North Atlantic in locations drawn from a time-space probability density function, where an axisymmetric atmospheric model is run and a genesis event occurs if

the vortex reaches a minimum wind intensity threshold. Tracks are advected with a beta-drift model that uses stochastically derived background steering winds. Intensity is determined using the axisymmetric model that follows the track and is coupled with a one-dimensional ocean mixed layer model. The model provides the advantage of breaking from the limitations of observational data, especially in the case of long-term future climate projections. (It has even been used to make operational forecasts of hurricane intensity. In a test of intensity forecast performance for the 2002 Atlantic hurricane season, the CHIPS model has similar forecast errors to the SHIPS and GFDL models for up to 50 hrs of lead time. Then, it outperforms the other two models going out to 70 hrs of lead time.) GCMs can supply the hurricane model with atmospheric and ocean mixed layer thermodynamic information, and the hurricane model output is similar to observational databases: 2-hourly storm center positions, intensity, and radius of maximum winds. This downscaling procedure is described in more detail in Emanuel (2006). From the track output, we extract location and intensity data at landfall for our analysis.

b. Statistical tropical cyclone track model

In a second application of the Damage Index approach (Section 5b), we make use of a purely statistical model of North Atlantic (NA) tropical cyclones that can generate large ensembles of synthetic hurricanes. The NA statistical tropical cyclone track model (Hall and Yonekura 2012) is similar to the western North Pacific model described and used in the two previous chapters. The model is constructed using HURDAT best track data (Jarvinen et al. 1984) from 1950–2008, excluding storms lasting less than two days long to avoid ambiguity due to the under-sampling of short-lived storms. As with the western North Pacific model, the NA model employs local regression on independent predictor variables for genesis and track propagation. The predictor variables are relative SST (δSST) and ENSO (JASO Niño 3.4 Index). Relative SST is defined as

the difference between the North Atlantic main development region, 10°N to 20°N and 20°W to 85°W, SST for JASO and the tropical zonal average JASO SST from 20°N to 20°S. The quantity of δSST is of interest because Sobel et al. (2002) showed that the tropical mean SST controls the tropical upper-tropospheric temperature, especially in regions dominated by deep convection. It follows that δSST is a measure of the stability in the tropospheric temperature profile: a higher value of δSST implies a less stable environment which favors convection and thus higher TC potential intensity.

The intensity component of the model is different in character. HURDAT V_{max} time series are randomly sampled and placed on the simulated tracks. Sampling is weighted such that the HURDAT track of sampled V_{max} series is similar to the simulated track in genesis location, lysis location, landfall location (for TCs making landfall), and δSST state. A random perturbation is added to the selected V_{max} series in such a way that the distribution of maximum V_{max} along simulated TCs conforms to a Gumbel distribution fit to the HURDAT set of maximum V_{max}. Hall and Yonekura (2012) evaluate the model against direct HURDAT landfall rates, and show that model's landfall characteristics are unbiased.

For this study we use five sets of 10,000-year simulations, each with constant values of ENSO and δSST: neutral ENSO and δSST varying from -2 to +2 in units of standard deviation from the 1950-2008 mean. Thus, there is no reliance upon GCM output to simulate the hurricanes. The statistical track model output is in the form of 6-hourly storm positions, intensity, and radius of maximum winds. The landfall properties of these simulations are documented below and in Hall and Yonekura (2012). Again, the location and intensity at landfall is extracted from the tracks and used in our analysis.

c. Limitations of the economic data

There are a number of important limitations to these economic datasets, as discussed in both Pielke Jr. et al. (2008) and Collins and Lowe (2001). For the damage data, the true relationship between economic and insured damages is uncertain and will vary across time, due to changes in insurance utilization and practice, as well as from storm to storm, in particular in the case of extensive flood damage, which is often excluded from insurance policies. Moreover, data on insured losses were not collected prior to 1949, and so damage estimates during this period were produced by the National Oceanic and Atmospheric Administration (NOAA) based upon local post-event surveys, which may be prone to larger error without private estimates available for reference.

The county-level economic data also contains important uncertainties. First, U.S. Census data were not collected for population and households prior to 1925 and 1940, respectively, and therefore data from this period were calculated via extrapolation and thus have much greater uncertainty. Second, as originally described in Jarrell et al. (1992), the determination of which counties were "affected by the storm" was based primarily upon whether the county experienced hurricane force winds and/or storm surge at least 4 feet above climatological tide, but due to observational limitations this endeavor was ultimately highly subjective, particularly earlier in the historical record. Third, variability in the size, shape, and orientation of county borders along the U.S. Atlantic and Gulf coasts will result in modest variability in estimates of affected households and population along the coast, though large urban areas in coastal states typically lie on the coast itself, suggesting that this uncertainty may be relatively modest.

Finally, only coastal counties are included as "affected by the storm", with no accounting of inland counties that may have been subject to significant losses, particularly in the case of

inland flooding. We are unaware of any comprehensive estimate of the fraction of damage that occurs in coastal vs. inland counties for a typical storm. Thus, the model results presented below are focused primarily on damage caused by wind and storm surge.

3. The Damage Index

a. Theory

Conventional hurricane damage models use absolute economic damage as the dependent variable (Nordhaus 2010; Bouwer and Botzen 2011; Mendelsohn et al. 2011). Such models suffer from the need to normalize damages to a base-year and to adjust for population changes. In addition, absolute economic damage is highly sensitive to land-use specifics for each event, most importantly the economic value of the affected region, thereby potentially conflating the relative roles of variations in physical storm characteristics and coastal economic value in damage model predictions.

Here, we suggest a model that assumes the physical characteristics of the hurricane and the economic value at landfall location are independent. Following the approach of Neumayer and Barthel (2011), we decompose the total economic damage into the product of the damage capacity of the hurricane, denoted as the Damage Index, and the economic value at landfall location:

$$D_{yi} = I_i * E_{yi} \quad (1)$$

where D_{yi} is the economic damage for storm i reported in current-year (y) dollars, I_i is the Damage Index of storm i, and E_{yi} is the economic value of the landfall region of storm i. This equation can be rearranged to give the definition of the Damage Index:

$$I_i = \frac{D_{yi}}{E_{yi}} \quad (2)$$

Conveniently, this approach can be applied directly to base-year data and thus obviates the need to normalize economic values to a common year. We calculate the Damage Index using the raw data employed by Pielke Jr. et al. (2008). The numerator is defined as base-year (e.g., non-normalized) economic damages and is disaggregated into individual landfalls where applicable. The denominator is given by:

$$E_{yi} = H_{yi} * W_y \quad (3)$$

where H_{yi} is the number of households in those counties deemed "affected" by storm i and W_y is the national average wealth per household, calculated as the ratio of the aggregate base-year national wealth to the aggregate number of households nationally.

In theory, the Damage Index is dependent only on the physical characteristics of the hazard that cause or enhance damage, such as maximum wind speed, storm size, bathymetry, translation speed, landfall angle, and event duration, and is bounded within the interval [0, 1], where a value of 1 indicates total economic loss. In practice, though, the Damage Index has a few caveats. First, the numerous uncertainties discussed above in estimates of economic value, particularly uninsured, in both numerator and denominator, as well as the exclusion of inland counties in the denominator, muddies the strict upper bound. Second, calculating local economic value from the national average for household wealth is likely to underestimate the true economic value along the coast, particularly in localized affluent regions (e.g., vacation homes), given that coastal properties tend to be valued higher than elsewhere in the country (Collins and Lowe 2001). Finally, as noted in Neumayer and Barthel (2011), the Damage Index implicitly includes changes in vulnerability over time due to changes in building codes or other adaptive measures taken by rational individuals and governments. Despite these uncertainties, the

Damage Index should still capture the broad variability of coastal development in both space and time.

Household data for affected counties have not been compiled from 2005 onwards, and thus Damage Index values cannot be computed post-2004.

b. Damages vs. Damage Index: Basic statistics and the example of Bret (1999)

Fig. 4.1 shows the time series of Total Damage and Damage Index. The mean values (standard deviations) of the Total Damage and Damage Index are $4.73 billion ($14.1 billion) and 0.05 (0.11), respectively. An example which elucidates the stark contrast between Total Damage and Damage Index is Hurricane Bret (1999), which was a large Category 4 hurricane that made landfall in Texas in a region with a gradually sloping continental shelf favorable for high storm surge. Bret ranks first in Damage Index with a value of 0.89, indicating that it destroyed 89% of the total wealth in the affected counties. However, the absolute damage was only $76 million—well below our absolute damage threshold—because the landfall region was sparsely populated.

The linear correlation coefficient between Damage Index and the economic value at landfall is $r = -0.1$, confirming that the two quantities are nearly independent. We argue on this basis that it is more appropriate to fit a model that reflects the true intensity and destructive capacity of a hurricane like Bret (1999) rather than the absolute economic damages that it inflicted. This is especially important when one endeavors to make future projections on hurricane damages, since those are independently influenced by potential changes in the physical characteristics of hurricanes and by changes in the economic value along the coast (Pielke Jr. et al. 2008). In the following section, we fit GPDs to the Total Damage and the Damage Index, with and without physical covariates, in order to capture the aforementioned characteristics of damages caused by landfalling hurricanes.

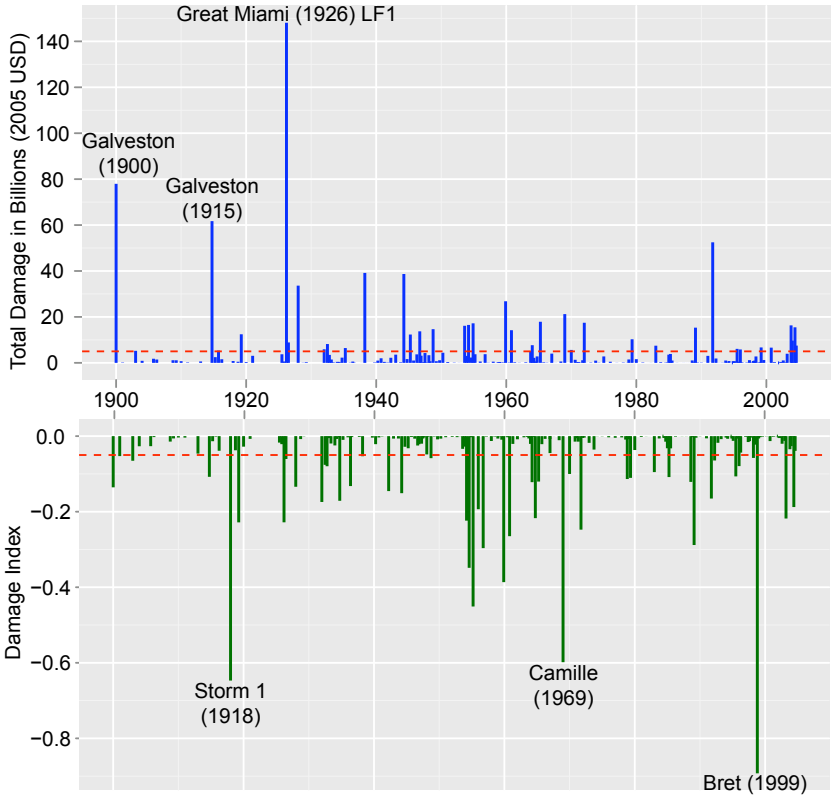

FIG. 4.1. Time series of damages caused by U.S. landfalling hurricanes as measured by Total Damage in 2005 dollars (top) and Damage Index (bottom). Red lines denote thresholds of $5 billion and 0.05, respectively. Storms with the three highest values of each are labeled (Note: `LF' denotes landfall number for multi-landfall storms.

4. Generalized Pareto Distributions

a. Theory

We are interested in the maximum extent of economic damage possible from a single landfall and thus choose a model that concerns itself primarily with the extremes in the data. The Generalized Pareto Distribution specializes in describing individual extreme events—though it does not offer information about the frequency if events—and has been previously used to model extreme insured losses from hurricane landfall (Jagger et al. 2008). In this section, extreme value

analysis is performed using a Peaks-Over-Threshold approach (Coles 2001), which models all excesses above a specified threshold value with a GPD, whose probability density function is given by:

$$P\left(x|x>\mu\right)=\begin{cases}\dfrac{1}{\sigma}\left(1+\xi\dfrac{x-\mu}{\sigma}\right)^{-1-1/\xi} & \text{if } \xi\neq 0,\\ \dfrac{1}{\sigma}\exp\left(-\dfrac{x-\mu}{\sigma}\right) & \text{if } \xi=0\end{cases} \tag{4}$$

where μ is the constant threshold, x is the Total Damage or Damage Index, σ is the scale parameter, and ξ is the shape parameter. The latter two parameters may be taken as constant or as a function of one or more covariates as shown in Eqs. (5a) and (5b) in Section 4a. The effect of each parameter is shown in Fig. 4.2. Changing the threshold parameter simply determines which extremes ("peaks") in the data will be considered, and its effect on the GDP PDF is merely to change the starting point of the distribution. The scale parameter, similar to the standard deviation in a normal distribution, determines the spread of the distribution. With higher scale parameter, the distribution of probability spreads out more evenly between outcomes. The shape parameter is particularly important in extreme value theory as it determines the behavior of the tail of the distribution, which gives the probability of the most extreme outcomes. For negative shape parameters, the distribution is bounded and behaves like a beta distribution. If the shape parameter is zero, there is a "skinny" or "light" tail—less probability density in the upper tail—that behaves like an exponential. For positive shape parameters, the tail is "heavy" or "fat" with more probability for upper tail outcomes. Physical variables, such as hurricane intensity, are usually bounded by theoretical constraints, and we expect hurricane economic damage to have a heavy tail as the damage record is dominated by extreme events in the tail (Fig. 4.1, top panel).

We first present the GPD fit without covariates, then proceed to include two physical covariates in the scale and shape parameters, namely the maximum wind speed at landfall, V_{max},

and the mean bathymetric slope, $\bar{s}$. In both cases, the input dataset is converted to standardized anomalies with zero mean and unit variance. Total Damage data are first divided by a factor of 10^9 for ease of comprehension.

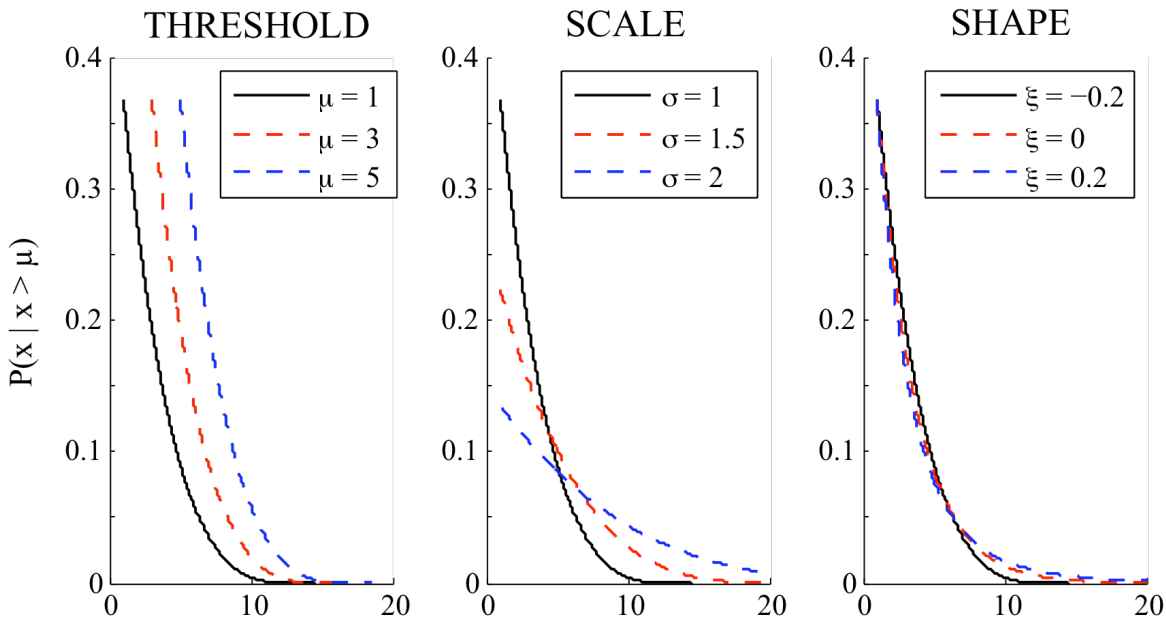

FIG. 4.2. Different Generalized Pareto Distributions with varying parameters. The black curve in each panel is the same. In the first panel, the threshold parameter is varied for each curve, showing how the distribution remains the same except for a lateral shift with each threshold. The second panel shows differences in scale parameter, which result in changes in distribution spread. The third panel shows how changes in shape parameter mostly affect the thickness of the tail.

For our analysis, following Coles (2001), we select the threshold for each dataset as the lowest value above which the dependence of the GPD parameters on this threshold is small in order to maximize the size of the subset of data used for the GPD model while still maintaining stable parameter estimates. Based on this analysis (not shown), we set the thresholds at $5 billion ($N = 39$) and 0.05 ($N = 45$), respectively, though our results are found to be robust to variations in these values over a reasonably large range of thresholds (2-6 billion USD and 0.02-0.06 for Total Damage and Damage Index, respectively). All parameter estimates and errors are based on a Maximum Likelihood Estimation (MLE) approach calculated using the "extRemes" package

(Gilleland and Katz 2011) in the R statistical software interface (R Development Core Team 2010).

b. Damages vs. Damage Index: GPD fit without covariates

Table 4.1 displays the MLE-based parameter values and standard errors for the GPD fit without covariates. The GPD of Total Damage has a statistically significant positive shape parameter, with an MLE estimate of 0.58 and standard error of 0.27, which indicates the existence of a fat upper tail. The same is not true for the GPD of the Damage Index, whose MLE estimated shape parameter is 0.14 with a standard error of 0.17, though the error range of this estimate indicates that the value is still likely positive. In order to see the actual behavior of the distribution of economic vulnerability along the U.S. coast, we fit a GPD to GDP data of all coastal counties (Yale G-Econ). Using a threshold of 2.5 billion in 2005 USD, the shape parameter is 0.64 with a standard error of 0.25. The shape parameter is positive and thus the distribution has an even fatter tail than Total Damage.

TABLE 4.1. MLE parameter values (standard errors) for GPD fit with no covariates. Thresholds for Total Damage, Damage Index, and Coastal GDP are \$5 billion ($N = 39$), 0.05 ($N = 45$), and \$2.5 billion ($N = 46$), respectively.

	σ	ξ
Total Damage	7.79 (2.34)	0.58 (0.27)
Damage Index	0.13 (0.03)	0.14 (0.17)
Coastal GDP	17.49 (4.75)	0.64 (0.25)

The respective quantile-quantile (Q-Q) plots are displayed in Fig. 4.3, which plot data versus the modeled values to show the model "goodness of fit". The model fit to the data is best if all points lie on the diagonal line. In both cases the model fits the data qualitatively well except in the highest quantiles. Quantitatively, for Total Damage the model and data match well for

D_{2005} < 30 billion USD, for 30 < D_{2005} < 80 billion USD the model diverges slightly with an average error of 7.6 billion USD, and for the most extreme case (Great Miami 1926) the model error is 44 billion USD, though this error lies well within the 95% confidence intervals and, given the numerous uncertainties in estimating damages and normalizing to 2005 dollars for a storm this early in the historical database, such an error may well be within the bounds of observational uncertainty. For Damage Index, the model error is small over a larger fraction of the dataset than for the Total Damage (I_i < 0.4), however the model fit exhibits a more pronounced divergence for the three most extreme cases, with error maximizing at 0.2 for the most extreme case of Bret (1999).

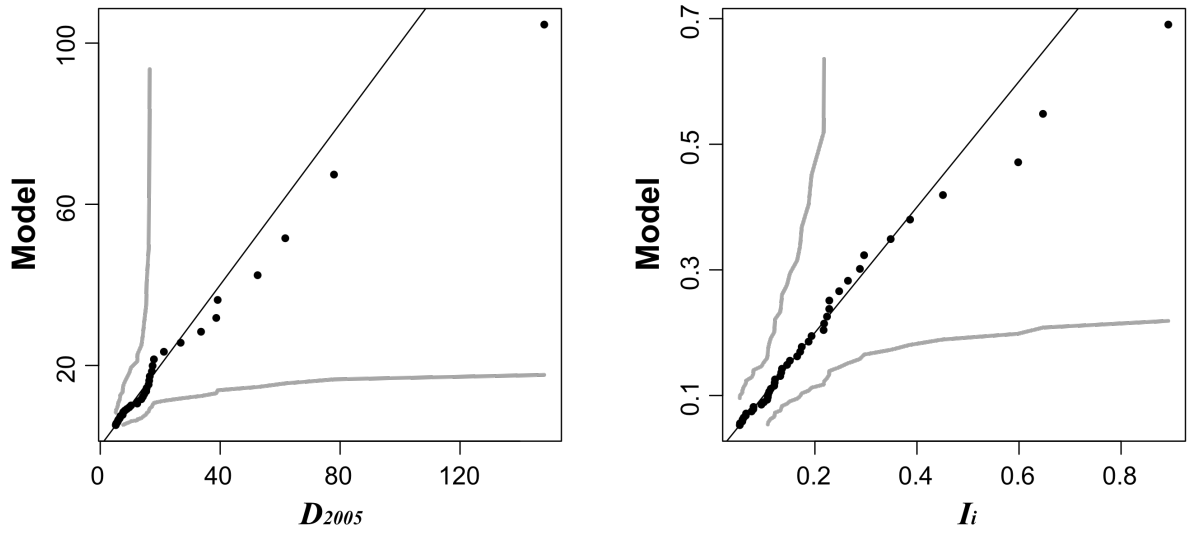

FIG. 4.3. Quantile-quantile plot for Total Damage (left) and Damage Index (right) without covariates. Gray lines represent the 95% confidence band (Doksum and Sievers 1976).

Because the Damage Index is intended to capture the effect of the physical characteristics of the storms, one might expect the tail of its distribution to exhibit skinny ($\xi = 0$) or bounded ($\xi < 0$) tail behavior given the bounds on physical quantities such as storm intensity, wind speed, shelf slope, etc. However, it is not a requirement that a physically-bounded geophysical

phenomenon produce bounded tail behavior in its resulting damage GPD because damage could be a power transformation function of the physical phenomenon (e.g., $D \sim V_{\max}^{9}$; Katz 2012). Nonetheless, this initial statistical result provides evidence that the heavy-tailed distribution that has been linked traditionally to economic damage by hurricanes may be a manifestation primarily of the strong variation of economic value along the coast rather than the physical characteristics of storms themselves.

c. Damages vs. Damage Index: GPD fit with covariates

We then add two covariates, maximum wind speed (V_{max}) and mean bathymetric slope ($\bar{s}$) at landfall, to the scale (σ) and shape (ξ) parameters in the following form:

$$\ln(\sigma) = \sigma_0 + \sigma_1 V_{\max} + \sigma_2 \bar{s} \tag{5a}$$

$$\xi = \xi_0 + \xi_1 V_{\max} + \xi_2 \bar{s} \tag{5b}$$

Recall that each input dataset is first standardized to have zero mean and unit variance. The logarithm is used on the left-hand side of Eq. (5a) to ensure that the scale parameter remains positive and thus the GPD well-defined. Covariate values for landfall intensity (V_{max}) were taken as the values at the final Best Track 6-hourly value prior to landfall.

In order to incorporate the complex effect of bathymetry on storm surge in a simple manner, we calculate as a covariate a mean bathymetric slope, $\bar{s}$, based upon the distance, r, along the shore-normal vector extending to a particular isobath of depth h. The mean slope is therefore defined as:

$$\bar{s} = \frac{h}{r} \tag{6}$$

The mean slope is calculated at 65 points along the U.S. mainland coast from Texas to Maine (Fig. 4.4). The 65 coastal points were selected to remove the effect of small-scale coastal

features, which may not be characteristic of the region as a whole. For each storm, the covariate value is taken to be the slope at the point nearest to the landfall location. Note that a low slope indicates a wide, shallow shelf, which favors higher storm surge (Irish and Resio 2009). Irish and Resio (2009) found that the distance to the h = 30m isobath is an optimal characteristic length scale for storm surge generation. Indeed, across a variety of metrics for mean slope based on distance to a given isobath, water depth at a given distance from shore, and integrated depth over either distance measure, we found that the distance to the h = 30m isobath performed best and will henceforth be the metric for r used in this work.

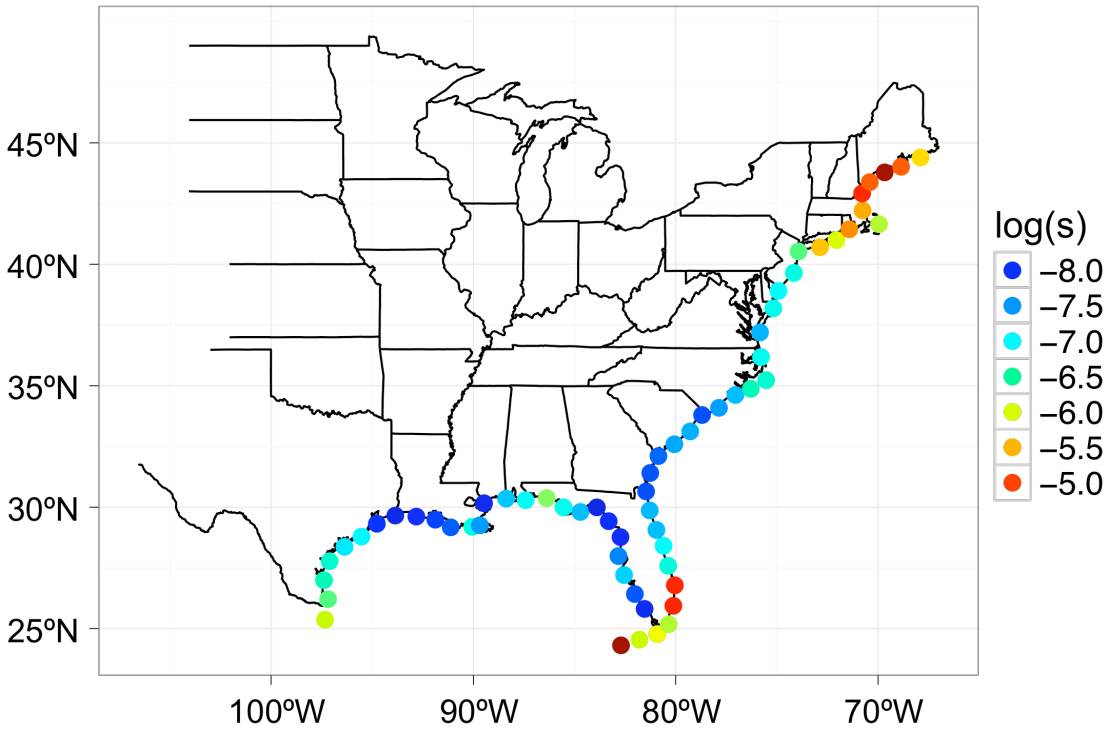

FIG. 4.4. Distribution of the logarithm of the mean slope along the U.S. coast (see text for details). Regions with low slope values (blue colors) are more vulnerable to damages due to storm surge.

We fit GPD models to Total Damage and Damage Index and then apply a deviance test to determine, based on the resulting p-value, whether the successive addition of a given covariate to the scale or shape parameter improves the model fit. We test covariates in the following order:

1. Individual covariates in the scale parameter

2. Multiple covariates in the scale parameter for those found individually useful

3. Single covariates in the shape parameter for those found useful in scale parameter

A p-value < 0.05 indicates the parameter coefficient is statistically significantly different from zero at the 95% confidence interval. For Total Damage, V_{max} is found to be a marginally useful covariate in the scale parameter (p = 0.06) while $\bar{s}$ is not (p = 0.19). On the other hand, for the Damage Index, $\bar{s}$ is the most useful individual covariate in the scale parameter (p = 0.014), while V_{max} is marginally useful (p = 0.07); indeed, adding V_{max} as a second covariate with $\bar{s}$ is also marginally useful (p = 0.07). The p-value for both covariates compared to the covariate-free case is p = 0.009. The available dataset is insufficient to determine statistically significant utility of covariates in the shape parameter in either case, and therefore it is left constant.

TABLE 4.2. MLE parameter coefficient values (standard error) for GPD fit with covariates, following Eqs. (5a) and (5b) for scale and shape parameters, respectively. Total Damage includes Vmax (p=0.06), while Damage Index includes V_{max} and $\bar{s}$ (p=0.009). Thresholds for Total Damage and Damage Index are \$5 billion (N = 39) and 0.05 (N = 45), respectively.

	σ_0	σ_1	σ_2	ξ_0
Total Damage	1.67 (0.38)	0.43 (0.23)	n/a	0.54 (0.26)
Damage Index	-2.24 (0.24)	0.28 (0.15)	-0.55 (0.17)	-0.0003 (0.15)

The resulting covariate coefficients with standard errors are displayed in Table 4.2. The GPD of Total Damage again has a statistically significant positive shape parameter, with an MLE estimate of 0.54 and standard error of 0.26. As for the GPD of the Damage Index, the MLE estimated shape parameter is now reduced to zero (-0.003) with a standard error of 0.15. The respective residual Q-Q plots (Ben and Yohai 2004) are displayed in Fig. 4.5. For Total Damage, the distribution of modeled residuals fit well for the lower quantiles but then fall slightly short of the observed residuals over the remaining quantiles, though the model does not exhibit any

pronounced divergence from the data. For Damage Index, the model distribution of residuals also fits well over the lower quantiles, but then the remainder of the residual distribution is skewed to the right relative to the model, as indicated by the model first overestimating and then underestimating residuals for higher quantiles.

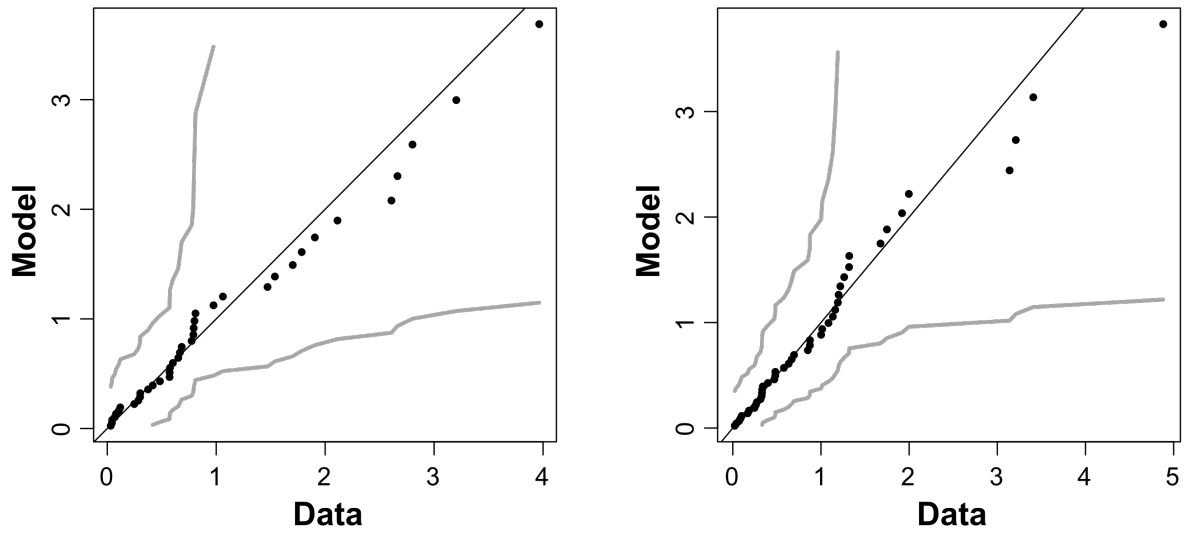

FIG. 4.5. Residual quantile-quantile plot (exponential scale) for Total Damage (left) and Damage Index (right) with covariates: Total Damage includes V_{max} and Damage Index includes V_{max} and $\bar{s}$. Gray lines as in Fig. 4.3.

Thus, in the case of the Damage Index with covariates, the maximum likelihood range for the shape parameter is shifted downwards significantly such that it is now centered at approximately zero. The Damage Index appears capable of transforming the damage distribution from fat-tailed to skinny-tailed, albeit with some uncertainty. This result provides further evidence that the fat tail in the distribution of economic damage may be primarily a result of the distribution of economic value along the coast.

Importantly, for Damage Index not only are the two covariates found useful, but the signs of their respective coefficients—positive for V_{max}, negative for $\bar{s}$—are also consistent with

physical intuition: damage should be directly proportional to V_{max} and inversely proportional to $\bar{s}$, all else being equal. Moreover, the magnitude of the coefficient of $\bar{s}$ is approximately twice that of V_{max}, indicating that the capacity of a given storm to cause damage is more sensitive to changes in (normalized) slope as compared to maximum wind speed (though they are not independent for storm surge generation). These relationships are found to be largely insensitive to variations in the threshold.

Overall, in contrast to the Total Damage, we find that the Damage Index is sensitive to both maximum wind speed and local bathymetry at landfall, giving statistical confirmation to what would be expected of the underlying physics of a landfalling hurricane. Surprisingly, our analysis suggests that, among the most destructive storms, the capacity for a storm to cause damage may be most strongly linked to the modulation of storm surge by the local bathymetry, a result that is absent in the analysis of Total Damage.

5. Potential Applications to Hurricane-Climate Questions

Finally, we provide two illustrative examples of how the Damage Index analysis approach could potentially be used to assess changes in the probability distribution of the most damaging hurricanes in varying climate states.

a. Future climate hurricane example

We apply our GPD model with covariates calculated from the historical data to two sets of approximately 5000 synthetic landfalling tracks, one downscaled from the current climate (1981-2000) and one downscaled from the future climate (2081-2100) under the IPCC A1b scenario as simulated by two GCMs: GFDL CM2.0 and ECHAM5. Comparison of the spatial and seasonal variability of the synthetic storms with the historical record is provided by Emanuel et al. (2008)

as a means of assessing the quality of each model's synthetic storm dataset. We emphasize here that, given the large range of projected changes in hurricane intensity and frequency at the regional scale across models (Knutson et al. 2010), proper assessment of changing risk profiles demands analysis of output from an ensemble of climate models; indeed the GFDL model lies on the upper end of the model range for projected increases in Atlantic hurricane activity in the future climate (Villarini et al. 2011), though this is largely a consequence of a significant increase in its projection of landfall frequency rather than in changes in the characteristics of individual storms. Moreover, it is implicitly assumed that the estimated model parameters will not change in the future, as a lack of data prohibits a robust assessment of non-stationarity. Thus, the results presented below should not be interpreted as a quantitative projection for changes in hurricane risk but rather as demonstration of the potential use of the statistical model presented here within the framework of a more comprehensive risk assessment.

For each synthetic landfall event, we compute the covariates V_{max} and $\bar{s}$ and apply them to Eq. (5a) to estimate scale parameters for each storm. The resulting GPD PDF for each storm is summed together and renormalized to a single standard PDF that integrates to unity, the result of which then represents the aggregate PDF for a given landfalling storm, irrespective of landfall frequency. Importantly, though this implicitly and incorrectly assumes that every storm is above threshold, identical application of this methodology to both current and future hurricane datasets still permits an apples-to-apples comparison that captures shifts in the probability distribution of the most extreme events.

In order to extend this approach to changes in actual economic damage, though, reliable information on changes in landfall frequency (both spatially and temporally) and economic value along the coast is needed. For the former, there is little agreement across models even on the sign

of the change in Atlantic hurricane frequency, much less landfall frequency (e.g., Knutson et al. 2010). Similarly, for the latter, regional economic change is highly uncertain (Pielke Jr. et al. 2000), though recent history indicates that development in vulnerable coastal areas will continue to proceed at rates much higher than those of much of the rest of the country (van der Vink et al. 1998). Thus, we elect to apply our methodology solely to explore changes in the PDF of the Damage Index, leaving the issues of frequency and economic value to future work.

Fig. 4.6 (top) displays the aggregate GPD PDFs for the current and the future GFDL climates as well as for the historical record. The current GFDL climate matches the historical PDF reasonably well, though with a slight skew to the left (historical $p(I_i > 0.2) = 0.27$ vs. GFDL $p(I_i > 0.2) = 0.24$), lending some confidence in the capacity of this model to project changes in the most damaging landfalling hurricanes into the future. Note that shifts in the PDF result from changes in the scale parameter, as the shape parameter does not have covariates and thus remains constant. A rightward shift in the PDF, indicative of an increased probability that a given landfalling storm will be more damaging, is evident under the A1b scenario; this is independent of landfall frequency. The mean increase in the scale parameter is 0.01, or approximately 10% of its mean value, and the probability of a storm with a Damage Index value exceeding 0.2 increases by 3.6%. The cause of this is likely the overall upward shift in the distribution of maximum wind speed (V_{max}) under this scenario but may also be due to shifts in frequency of landfalls at locations with different $\bar{s}$. Importantly, though, the increase in the scale parameter lies within the range given by the standard errors for our parameter estimates (for average values of V_{max} and $\bar{s}$, $\sigma = 0.106$ with an error range of [0.084, 0.135]), indicating that the shift in the PDF is not statistically significant.

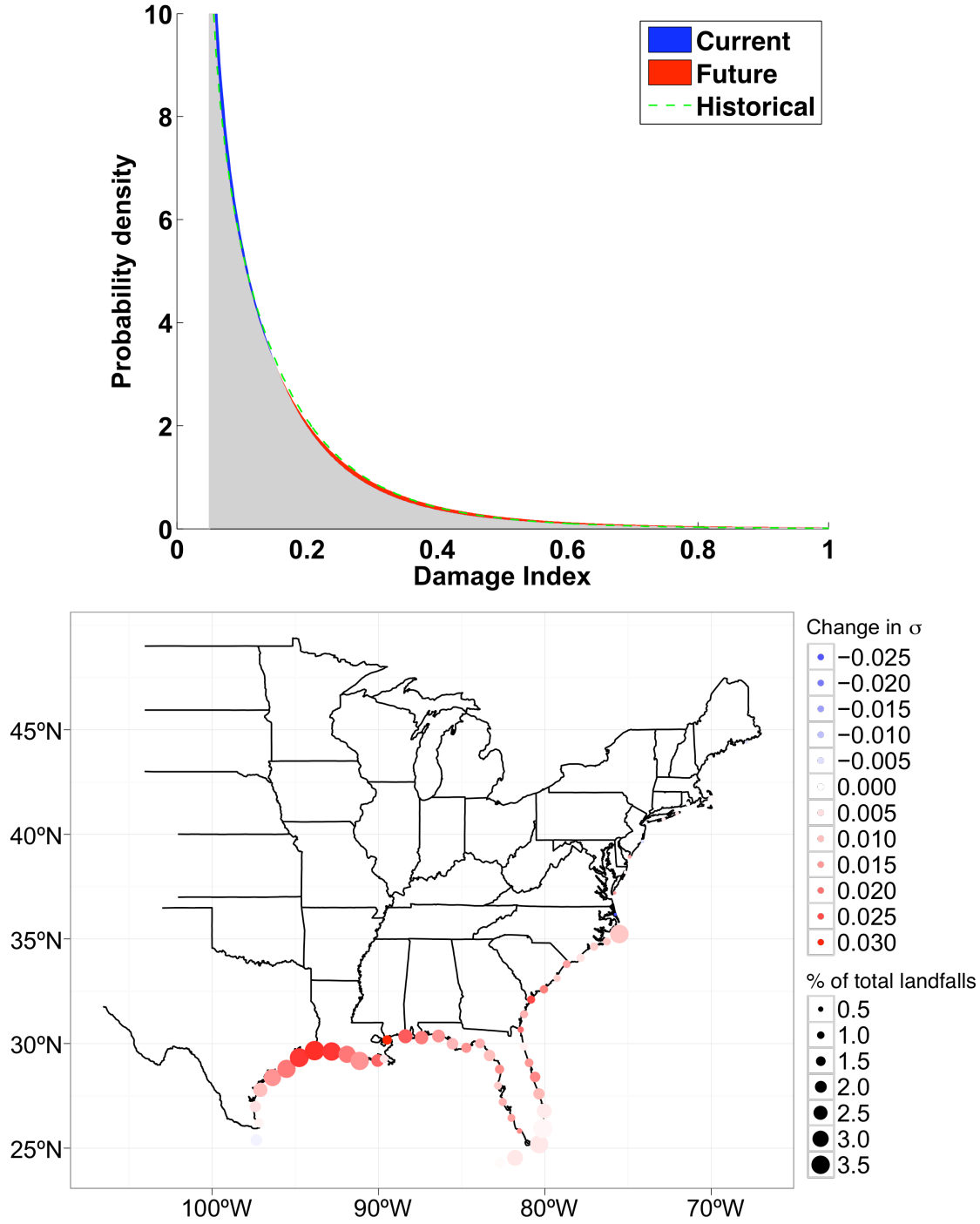

FIG. 4.6. (Top) Aggregate PDFs of the Damage Index from the GPD fit for the historical record (green dashed line; HURDAT 1851-2009) as well as for the current and IPCC A1b future climates in the GFDL model; red (blue) area indicates rightward (leftward) shift in the distribution in the future climate. (Bottom) Change in the mean scale parameter of the GPD fit with covariates of the Damage Index along the U.S. coast between the current and future climate simulations; marker size indicates relative spatial frequency of landfall for the combined datasets. Importantly, the displayed changes do not exceed the standard errors in the parameter estimates themselves and thus are likely not statistically significant.

Neglecting changes in frequency between the current and future climate scenarios, the intensity at landfall for all U.S. landfalling hurricanes shifts toward fewer low intensity storms (below 70 kts) and more high intensity storms (Fig. 4.7). This is in agreement with a suspected overall trend in tropical cyclone activity with climate change (Knutson et al. 2010). The shift is evident in both GFDL and ECHAM model simulation sets, however, the magnitude of the shift is lower for the ECHAM model. Further, the ECHAM model has a higher occurrence rate of low intensity hurricane landfalls. The change to higher landfall intensities will increase the scale parameter for both the Total Damage and Damage Index GPD models.

Shifts in the distribution are disaggregated into coastal segments and are also shown in Fig. 4.6 (bottom), which displays the distribution of the change in the mean value of the scale parameter between the current and the future GFDL climates along the United States coastline. The largest increases occur along the northern Gulf Coast (maximum increase is +0.034), where the relative landfall frequency is the highest and where coastal slopes tend to be shallow (Fig. 4.4) and thus conducive to large storm surge. Meanwhile, decreases are found along the mid-Atlantic and Northeast coasts (maximum decrease is -0.028 on Northern North Carolina coast). Again, given the standard error range for our parameters and the reduced sample size that accompanies a regional disaggregation, even the largest increases in σ are likely not statistically significant.

Given that the GFDL model lies at the upper end of the range of projections for changes in hurricane activity (though primarily due to increases in landfall frequency), we performed an identical analysis for output of the ECHAM model, which lies on the lower end of this range. The ECHAM model output exhibits virtually no shift in the aggregate GPD PDFs between the current and future climate states (Fig. 4.8), with a spatial distribution of changes in the scale

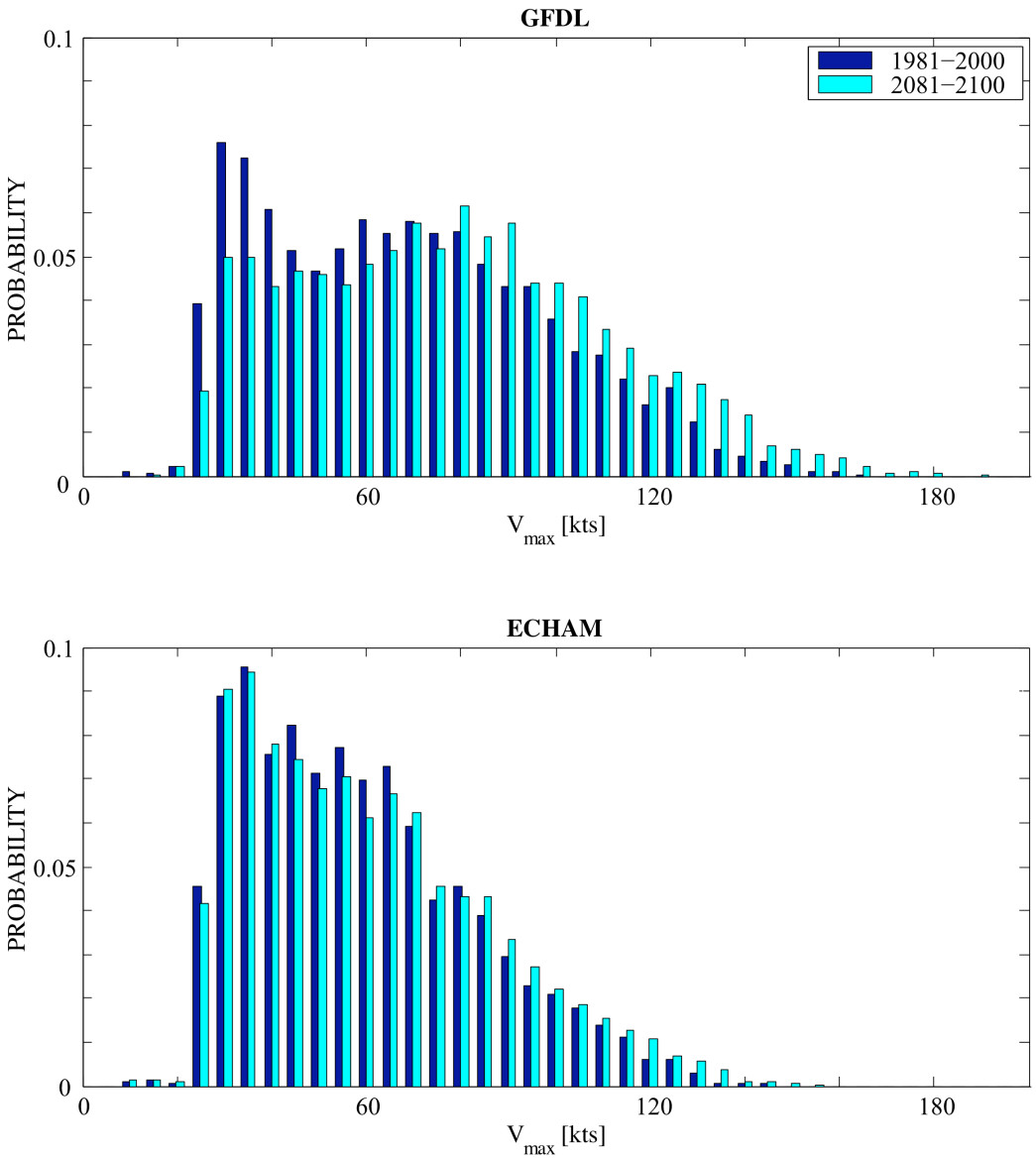

FIG. 4.7. Storm intensity (V_{max}) probability distribution for the GFDL and ECHAM downscaled hurricanes in the current and future climate scenarios. For both climate models, the distributions shift toward more high intensities, especially past 60kts.

parameter that is broadly similar to that of the GFDL model but with magnitudes that do not exceed 0.013. Notably, ECHAM does a poorer job of reproducing the historical GPD PDF, with a PDF that is skewed farther to the left than GFDL (ECHAM $p(I_i > 0.2) = 0.21$). Nonetheless, the ECHAM and GFDL model results taken in combination help to elucidate the disagreement in model projections of changes in the most damaging landfalling hurricanes and underscores the

need for a multi-model ensemble approach that also accounts for changes in landfall frequency in order to assess changes in hurricane damage risk with greater fidelity.

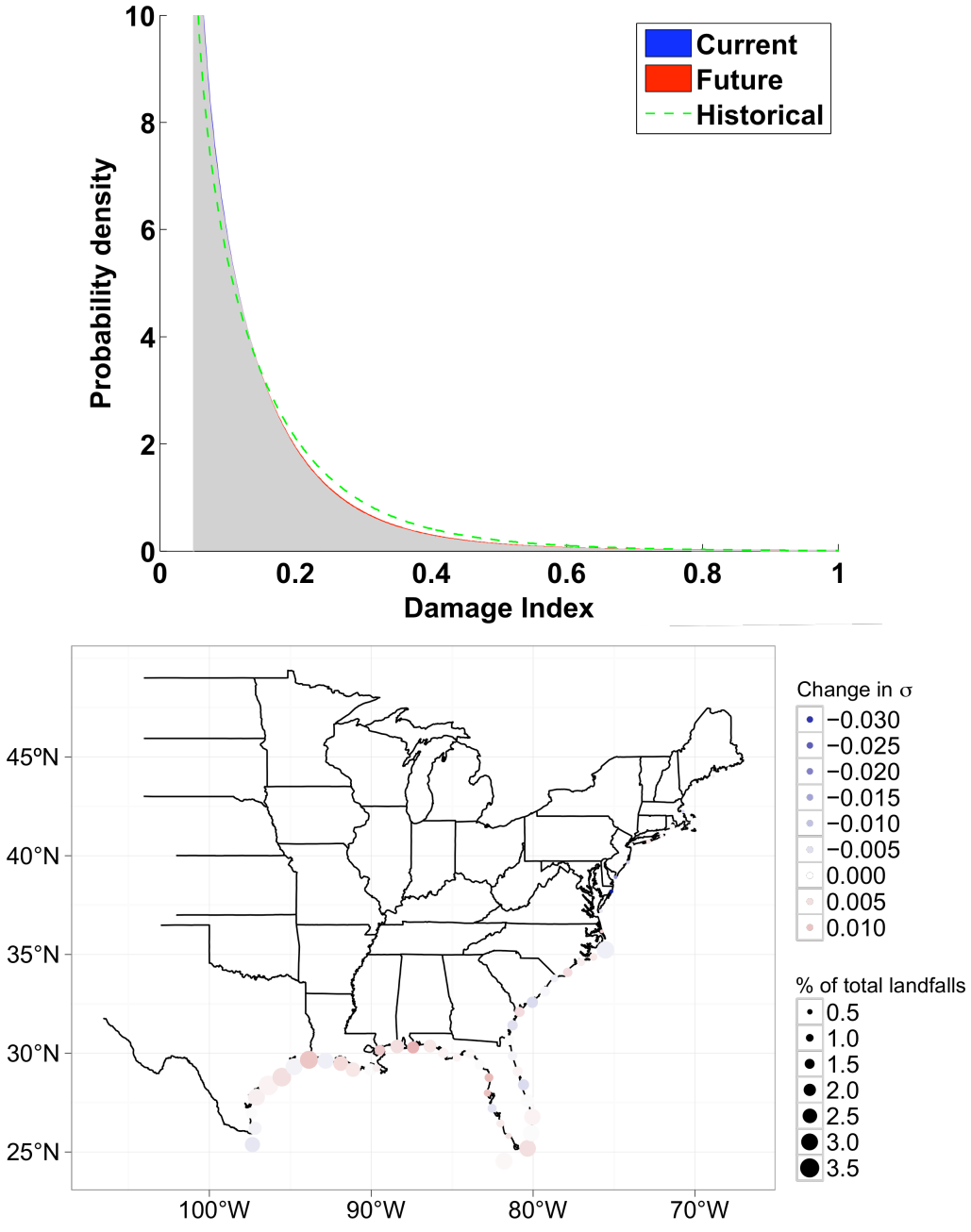

FIG. 4.8. Similar to Fig. 4.6 but for the ECHAM model climate backgrounds. Note that the bottom panel color scale has been kept the same to show that the changes in scale parameter for the ECHAM model are much smaller in magnitude than those for the GFDL model.

b. Relative sea surface temperature and hurricanes

In our second application of the GPD analysis, we estimate the impact of changes in relative SST (δSST) on hurricane damage. The relative SST analysis is motivated by Vecchi et al. (2008), who examined whether North Atlantic hurricane activity (in terms of power dissipation index) correlates more with SST or δSST. Implications of this choice of statistical predictor variable are large for forecasting future hurricane activity, as IPCC climate models project very different futures for SST and δSST. SSTs will continue to increase due to anthropogenic climate forcing. In contrast, δSST has varied historically more with natural climate variability, and future projections suggest no long-term trends. Vecchi et al. (2008) argue that observations (Swanson 2008), hurricane potential intensity theory (Vecchi and Soden 2007), and high-resolution numerical models (e.g., Knutson et al. 2008) support the δSST relationship: increased δSST leads to changes in atmospheric circulation and decreased vertical stability in the North Atlantic, both of which favor hurricane genesis and intensification.

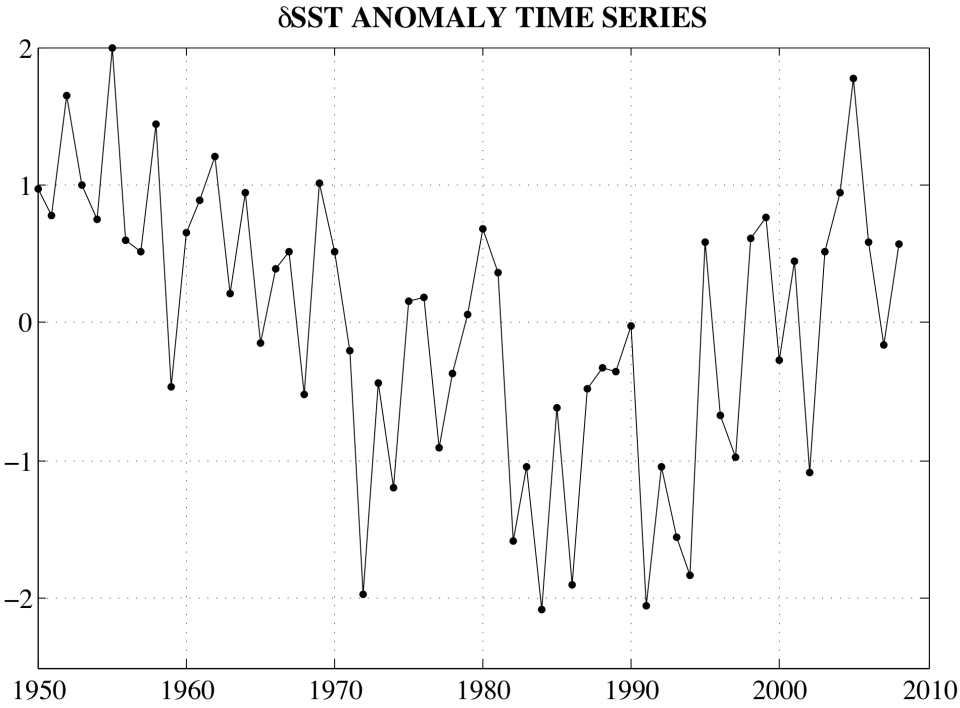

FIG. 4.9. Time series of observed relative SST as defined in this chapter.

In order to examine whether changes in δSST have an effect on the probability distribution of the most damaging storms in the U.S., we apply our GPD model of Damage Index with covariates (Table 4.2) to five different sets of 10,000-year stochastic hurricane simulations from a fully statistical track model (Hall and Yonekura 2012). Instead of taking input from GCMs, values of the statistical predictors (i.e. δSST) are specified for the annual formation rate, genesis location, track propagation, and intensity components of the track model. For each synthetic hurricane set δSST is held to one of five fixed values: -2, -1, 0, +1, +2, in units of standard deviations of δSST from the 1950-2008 mean. The observed values of this definition of δSST are shown in Fig. 4.9, where there are a couple years that near the most extreme values we examine. As Vecchi et al. (2008) state, there has been an upswing in recent δSST, but projections do not show this continuing in the long-term future. Landfall intensity and location values are extracted from the tracks.

Similar to the previous analysis in Section 5a, there is a shift in the intensity at landfall over the entire U.S. Coast (Fig. 4.10). For higher δSST, there is a shift to both more landfalls and more intense landfalls. A key difference between this study of the effect of δSST and the previous one examining future climate scenarios is that the δSST simulations account for changes in hurricane frequency. In the North Atlantic HURDAT record there is a positive correlation between δSST and the annual TC count, and this is reflected in the statistical model's simulations. The shifts in the landfall intensity distribution with δSST (Fig. 4.10) are a combination of the changes with δSST in basin-wide frequency, genesis location, intensity, and track shape. Another key difference between the analyses is the time scales over which they may be applied. The purely statistical model of Hall and Yonekura (2012) cannot be extended to values of the predictor variables (δSST and ENSO state) beyond the historical range on which

the model is constructed, limiting the application to climate states not too different than the current state. In contrast, the GCM-driven analysis can be applied to the very different climates projected for the late 21st century, as the models are physically based. For both the purely statistical and GCM-based analyses we predict that a shift toward more high intensity landfalls will occur with higher values of the scale parameter.

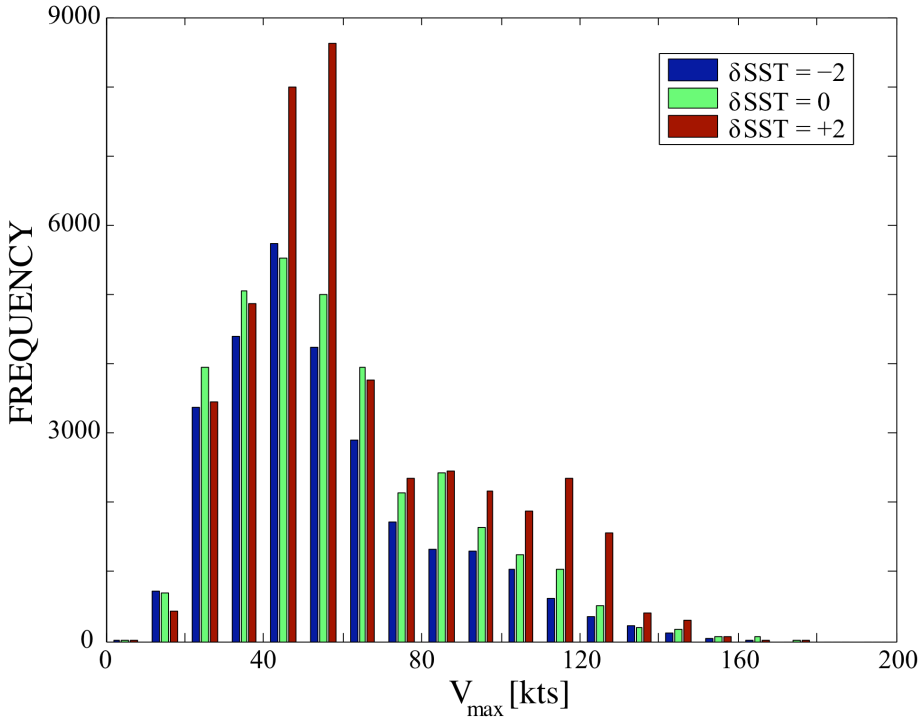

FIG. 4.10. Storm intensity (V_{max}) frequency distribution at landfall over the U.S. coast for δSST climate backgrounds of -2, 0, and +2. The distribution is kept in frequency count units to also show the effect of increased number of storms for higher δSST. For higher δSST, there are usually higher intensities.

Changes in the Damage Index depend on where along the coast landfall rates increase. If hurricane landfall rates increase on shallow sloping regions, then the potential for damage will increase more than if the landfall increase is on steep slopes. In Fig. 4.11, we examine the local changes in landfall rate for TCs (of any intensity) as a function of δSST. Overall, there is an increase in landfall frequency with δSST, which is primarily due to the increase in hurricane

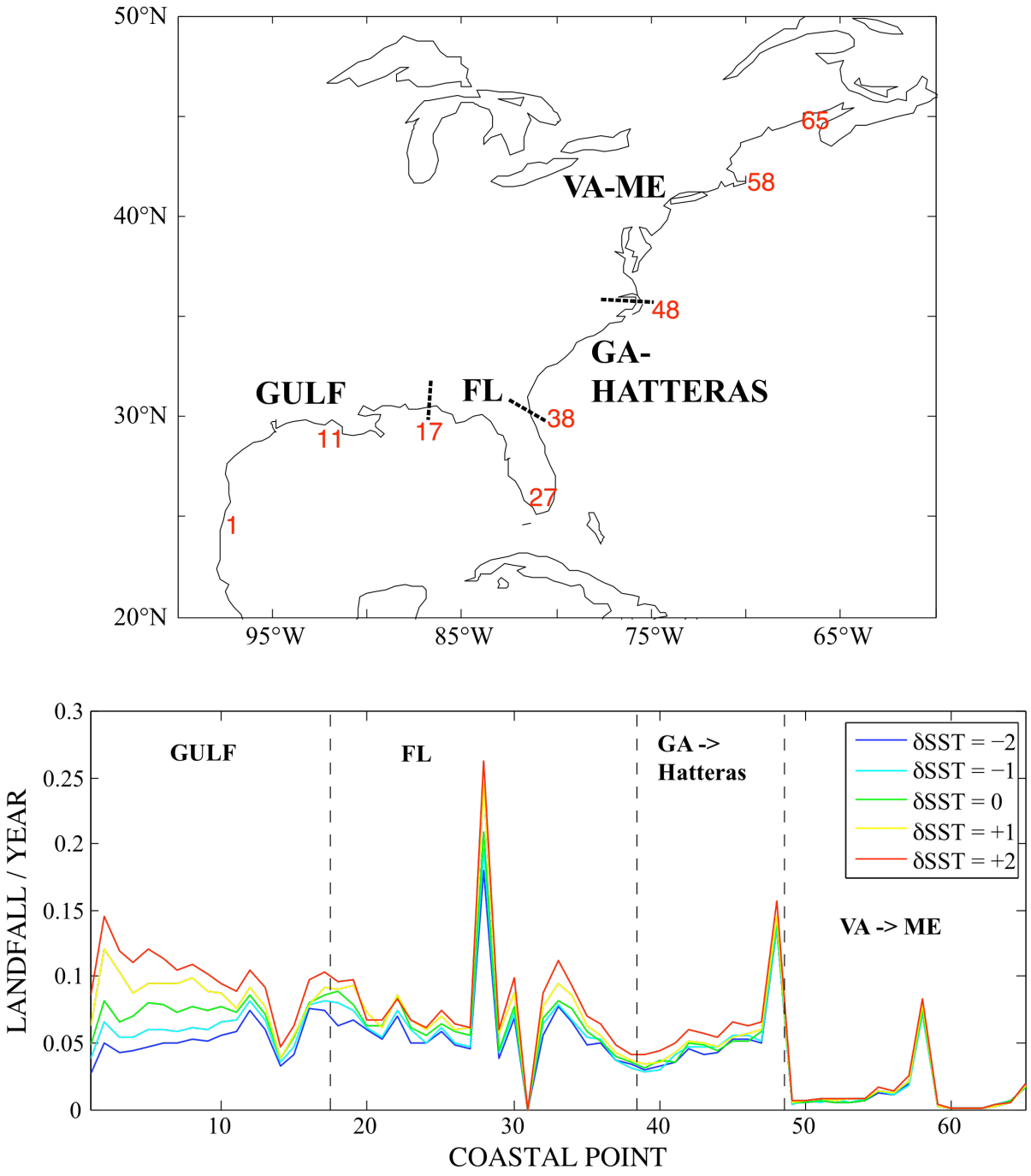

FIG. 4.11. (Top) Map of U.S. coastline divided into numbered segments as well as larger regions that are labeled and sectioned off by dashed lines coordinating with the bottom panel. (Bottom) Landfall rates in units of number of landfalls per year that occur at each point along the U.S. coastline for each δSST climate simulation of 10,000 years for all hurricanes regardless of intensity. There is a gradual increase in landfall frequency with increasing value of δSST, especially along the Gulf Coast.

genesis in the North Atlantic. However, the magnitude of the landfall frequency change varies greatly along the coast. It is largest along the Gulf Coast, especially in Texas. It is more moderate from Florida through Cape Hatteras, and it is hardly detectable north of Cape Hatteras. (In fact, Hall and Yonekura (2012) show that along the entire eastern seaboard the landfall increase with δSST is not statistically significant.) These regional variations in sensitivity to δSST are due to a complex interplay between changing genesis location, changing intensity, and changing track shapes (Hall and Yonekura 2012). Considering the local bathymetry in these areas (Fig. 4.4), higher δSST would mean more landfalls on low sloping coastlines in the Gulf and increase the likelihood of higher aggregate damage.

Every simulated landfall has a bathymetric slope and intensity value that is used to calculate a scale parameter with Eq. (5a) and the Damage Index parameters from Table 4.2. Scale parameters for landfalls on the same coastal region—regions are numbered in Fig. 4.11 (top)—are averaged for each synthetic track set to get the aggregate local scale parameter. As evident in Fig. 4.12, aggregate local scale parameter for δSST = +2 increases almost everywhere along the U.S. coast compared to δSST = -2. The only places where the opposite is true are on the western coast of the Gulf of Mexico and in latitudes above 40°N. The average change in scale parameter is 0.026, with the maximum change of 0.067 in Louisiana and a minimum change of -0.030 on the far western Gulf Coast, in Texas. The latter may be due to a reduction in the very highest V_{max} values at landfall for that point, as the moderately high bathymetric slope value at that point (Fig. 4.4) does not change with climate state. As in the GCM-driven example, the standard error range for the scale parameter and the reduced sample size from regional disaggregation renders most of the changes in Fig. 4.12 statistically insignificant.

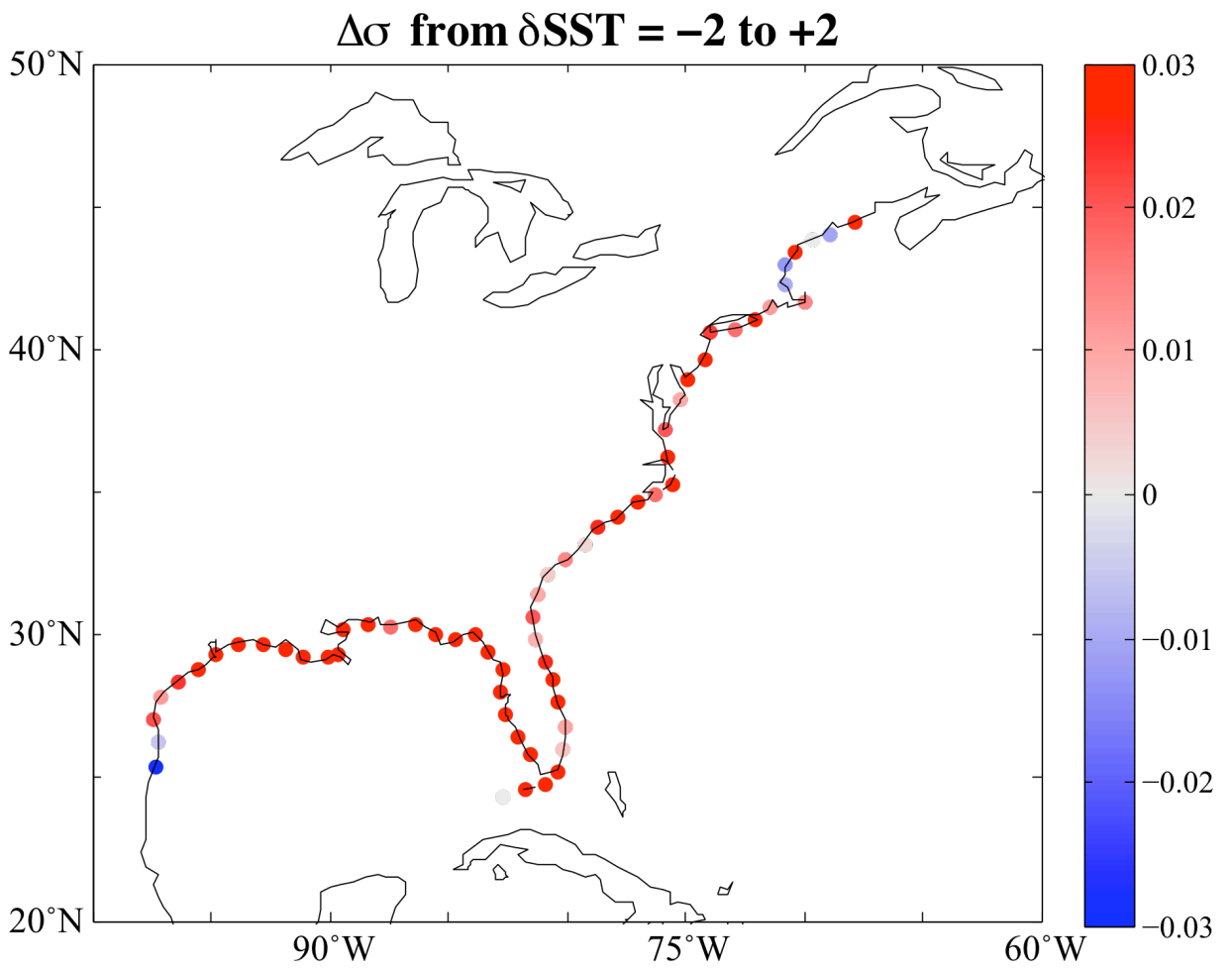

FIG. 4.12. Change in the scale parameter between a δSST value of -2 and +2 along the U.S. Coast. In nearly all regions, the scale parameter increases (red), indicating more spread in the Generalized Pareto Distribution.

Each of the local scale parameters defines a GPD along with the Damage Index shape parameter from Table 4.2, and we aggregate all of these GPDs by adding them and renormalizing. The resulting global aggregate GPDs for the +2 and -2 values of δSST are shown in Fig. 4.13. There is a small change in the PDFs between different climate states, with a larger spread for δSST=+2. Interestingly, the historical GPD has an even larger spread (dashed green). However, the historical landfalls for this GPD were taken from the HURDAT record of 1851-2009, while the statistical TC model is constructed on 1950-2008 data. When we recalculate the

aggregate GPD using only 1950-2009 HURDAT (black dashed) landfalls, the result lies between the δSST=-2 and δSST=+2 curves (red and blue). We leave to future work the exploration of the Damage Index difference between the 1851-2009 and 1950-2008 data. One possibility, which is evident in an examination of the landfall intensity distributions over time, is that the early HURDAT historical record under-represents landfalls of weak TCs, artificially increasing the relative probability that a landfalling storm is more damaging.

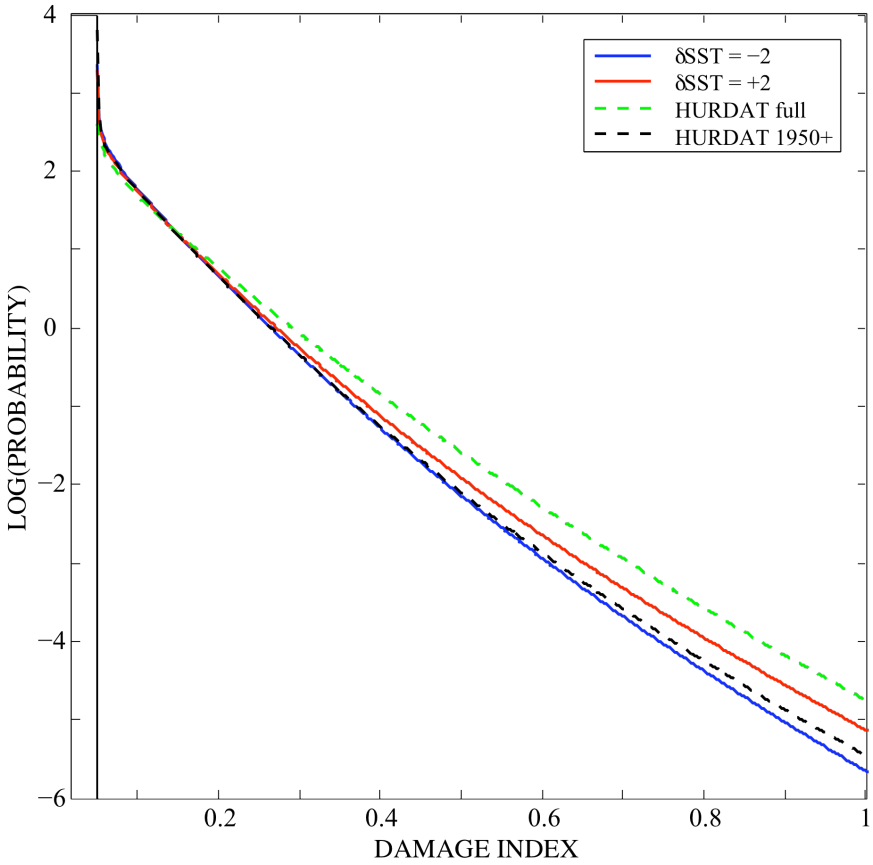

FIG. 4.13. Generalized Pareto Distributions that are aggregated from all the landfalls on the U.S. for the most extreme δSST climate states, -2 and +2. The vertical solid black line indicates the threshold at 0.05. For the majority of Damage Index values, the distributions are nearly identical, though the larger scale parameter for the +2 state (red) results in higher probability for Damage Index for values starting at 0.2 and higher. Dashed green line is as in Figs. 4.5 and 4.7 from the full historical record, and the black dashed curve is from the historical HURDAT record starting only at 1950. This curve sits between the red and blue curves.

For a more quantitative look at the different aggregate GPDs, we again calculate the probability per storm of Damage Index exceeding a value of 0.2 (Table 4.3). The values increase

with δSST, and the change from -2 to +2 results in a 11% increase in $p(I_i > 0.2)$. Consistent with Fig. 4.13, the 1851-2009 HURDAT landfalls give a higher $p(I_i > 0.2)$ than any of the simulated δSST sets. The 1950-2008 HURDAT landfalls, however, have a $p(I_i > 0.2)$ value that falls between those of +2 and -2 δSST.

TABLE 4.3. The probability that the Damage Index will be greater than 0.2 for each aggregated GPD PDF for both synthetic track landfalls as well as two periods of the HURDAT observations.

LANDFALL SET	$p(I_i > 0.2)$
δSST = -2	0.201
δSST = -1	0.202
δSST = 0	0.210
δSST = +1	0.217
δSST = +2	0.223
HURDAT 1851-2009	0.269
HURDAT 1950-2009	0.202

Overall, the statistical track model with varying relative SST further connects existing ideas of the expected changes in hurricane activity to U.S. landfall hazard and economic damage extremes. This is a crucial bridge between hurricane science and application to risk assessment.

6. Summary and Conclusions

This study employs a Peaks-Over-Threshold approach to the analysis of hurricane damages, which enables use of the Generalized Pareto Distribution to model excesses above a specified threshold. In addition to the historical database of Total Damage given in Pielke Jr. et al. (2008), we define a Damage Index as the ratio of base-year economic damages to the "available" economic value in the affected region. We then incorporate physical covariates at the individual hurricane level into the GPD, namely maximum wind speed and a simple yet novel measure of

the mean bathymetric slope at landfall, and apply our analysis to both the Total Damage and the Damage Index for the purposes of direct comparison.

We find based on Maximum Likelihood Estimation that while both Total Damage and Damage Index are sensitive to maximum wind speed, the Damage Index is additionally sensitive to the local bathymetric slope and has covariate coefficients that are consistent with the known physics of each in causing damage. Furthermore, the tail behavior of the modeled distribution of the Damage Index, particularly with covariates, suggests that the fat tail associated with the distribution of Total Damage may primarily be a consequence of the large variation in economic value along the coast.

We then provide two illustrative examples of the potential use of this new methodology. First, we apply it to datasets containing approximately 5000 synthetic landfalling tracks for current and future A1b-scenario climate states as simulated by two climate models: GFDL CM2.0 and ECHAM5. Climate models disagree strongly about how Atlantic hurricane activity will change in the future; the GFDL model lies on the upper end of this model range, primarily due to changes in landfall frequency, while the ECHAM model lies towards the lower end. Therefore, this application should not be interpreted as an assessment of hurricane risk. Comprehensive assessment of changes in the total economic damage requires analysis of output from multiple climate models that accounts for changes in both landfall intensity and frequency as well as changes in economic value at all points along the coast, a worthy task that is left to future work. The second example we show applies our GPD model to 10,000-year sets of synthetic tracks for different "relative SST" (δSST) values, the degree to which North Atlantic SST differs from global SST. There is an historical correlation between North Atlantic hurricane activity and δSST. We show that the implication of increased δSST for economic damage from

U.S. landfalling hurricanes is an increase in extreme damage risk for most of the coast.

Most importantly, this work makes three novel contributions to the field of economic damage and hurricanes:

1. Incorporation of physical quantities of individual storms as covariates in an Extreme Value Theory framework,

2. Inclusion of a simple but useful representation of the effects of local bathymetry on the damage capacity of a storm,

3. Calculation of a Damage Index and statistical comparison between Total Damage and Damage Index as metrics for the relationship between economic damage and landfalling hurricanes.

The results lend support to the ideas put forth in a global context by Neumayer and Barthel (2011): if there exists significant spatial variation in economic value that is susceptible to damage from a natural hazard such as a landfalling hurricane, efforts to attribute damages to the physical components of a natural hazard using absolute economic damage data for that disaster may confound economic and hazard variability. In its place, we find that damage measured as a fraction of potential damage can help remove the spatial economic variability from the damage database, leaving a signal that may be better representative of the physical relationship between the hazard and the damage it causes. A key limitation to this approach, though, is the availability of sufficient data that can capture the spatial distribution of economic value affected by hazard events. Moreover, it is unclear whether such a Damage Index is as easily defined in the context of more spatially- and temporally-complex hazards such as droughts and heat waves, particularly in developing countries where adequate observations of both physical storm characteristics and local economic data may not be available (UNISDR 2011; Klose 2011).

Nevertheless, this work provides an appealing alternative framework for assessing the relationship between the physical characteristics of landfalling hurricanes and the economic damage they cause, and it illustrates the potential applicability of this framework in assessing economic risk in both current and future climates. Given the statistically sparse historical record for landfalling hurricanes, choosing a proper framework for analysis is important both for optimizing the information extracted from the available data and for interpreting the results. Subsequently, these results serve as the basis for risk assessments. Thus, the approach outlined here may provide a step forward in our interpretation of, and adaptive response to, the historical record of hurricanes and economic damage.

Given the uncertainties in the input data highlighted above, though, it is important to consider the potential effects of these uncertainties on our GPD parameter estimates. In particular, the inability to account for damage due to inland flooding may result in an overestimation of the Damage Index in those cases where inland flooding accounts for a significant portion of a storm's total damage, as the economic value of the affected inland counties is not accounted for in the calculation of Eq. (3). The effect on the statistical model would therefore be a GPD PDF that skews toward higher Damage Index values—e.g., overestimates of σ, ξ, or both. If these overestimates are significant, this could potentially explain some of the discrepancy between the climate models GPD PDFs and that of the historical record. Additionally, the decrease in data quality earlier in the 20th century poses challenges given that the behavior of the upper tail is sensitive to the few storms that reside in that region of the PDF. This is particularly important for the Total Damage, for which the top three landfalls all occur prior to 1930. On the other hand, for the Damage Index, although the third largest value is associated with a storm that occurs in 1918, the top two cases, and more generally the majority

of the highest values (e.g., 80% for $I_i > 0.2$), occur post-1950 when both meteorological observations and economic data are significantly more precise. This suggests that the results for the Total Damage may be significantly less certain than for the Damage Index; however, it is unclear whether this decreased data quality would cause a high or low bias relative to the true value.

Future work seeks to extend the application of this analysis to projections of future hurricane activity across the full suite of climate models in order to gain a better quantitative assessment of how the distribution of extreme hurricane damage events may shift in the future under alternative climate states. Moreover, a more rigorous accounting of the spatial distribution of economic damage (e.g., coastal vs. inland) would serve to greatly enhance the precision of this approach. Finally, coupling of this work to models of landfall frequency and of coastal economic vulnerability may enable quantitative evaluations of absolute economic risk due to landfalling hurricanes both today and in the future, which may be of greater interest to stakeholders and policymakers alike.

Acknowledgements.

The authors would like to thank Rick Katz, Eric Gilleland, and Asuka Suzuki-Parker for their valuable help and guidance as part of the National Center for Atmospheric Research (NCAR) 2011 Advanced Study Program (ASP) Summer Colloquium on the Statistical Assessment of Extreme Weather Phenomena under Climate Change. We also thank the NCAR ASP for inviting us to the workshop that afforded us the opportunity to meet one another and to learn the techniques applied in this work. We gratefully acknowledge Prof. Roger Pielke, Jr., who provided the economic damage and coastal economic value datasets, Prof. Kerry Emanuel and his company, WindRiskTech LLC, who provided hurricane tracks from his model, as well as Tim Hall, who also provided hurricane tracks from his model. We thank three anonymous reviewers for providing valuable feedback that significantly improved this work. We also thank Kevin Sharp at ICAT Managers LLC for help obtaining damage data and both ICAT and StormPulse.org for their useful web interfaces for exploring hurricane landfall data.

References

Becker, J. J., Sandwell, D. T., Smith, W. H. F., Braud, J., Binder, B., Depner, J., Fabre, D., Factor, J., Ingalls, S., and Kim, S.-H., 2009: Global bathymetry and elevation data at 30 arc seconds resolution: SRTM30 PLUS. *Marine Geodesy*, **32(4)**, 355-371.

Ben, M. G. and Yohai, V. J., 2004: Quantile-quantile plot for deviance residuals in the generalized linear model. *Journal Of Computational And Graphical Statistics*, **13**, 36-47.

Bouwer, L. and Botzen, W., 2011: How sensitive are U.S. hurricane damages to climate? *Climate Change Economics*, **2(1)**, 1-7.

Coles, S., 2001. *An Introduction to Statistical Modeling of Extreme Values*, Vol. 97. Springer.

Collins, D. and Lowe, S., 2001: A macro validation dataset for U.S. hurricane models. *Casualty Actuarial Society Winter Forum*, 217-252.

Delworth, T. L., Broccoli, A. J., Rosati, A., Stouer, R. J., Balaji, V., Beesley, J. A., Cooke, W. F., Dixon, K. W., Dunne, J., Dunne, K. A., Durachta, J. W., Findell, K. L., Ginoux, P., Gnanadesikan, A., Gordon, C. T., Gries, S. M., Gudgel, R., Harrison, M. J., Held, I. M., Hemler, R. S., Horowitz, L. W., Klein, S. A., Knutson, T. R., Kushner, P. J., Langenhorst, A. R., Lee, H.-C., Lin, S.-J., Lu, J., Malyshev, S. L., Milly, P. C. D.,Ramaswamy, V., Russell, J., Schwarzkopf, M. D., Shevliakova, E., Sirutis, J. J., Spelman, M. J., Stern, W. F., Winton, M., Wittenberg, A. T., Wyman, B., Zeng, F., and Zhang, R., 2006: GFDL's CM2 global coupled climate models. Part I: Formulation and simulation characteristics. *J. Climate*, **19(5)**, 643-674.

Doksum, K. A., and Sievers, G. L., 1976: Plotting with confidence: Graphical comparison of two populations. *Biometrika*, **63**, 421-434.

Emanuel, K., 2006: Climate and tropical cyclone activity: a new model downscaling approach. *J. Climate*, **19**, 4797-4802.

Emanuel, K., Ravela, S., Vivant, E., and Risi, C., 2006: A statistical deterministic approach to hurricane risk assessment. *Bulletin of the American Meteorological Society*, **87(3)**, 299-314.

Emanuel, K., Sundararajan, R., and Williams, J., 2008: Hurricanes and global warming: Results from downscaling IPCC AR4 simulations. *Bulletin of the American Meteorological Society*, **89(3)**, 347-367.

Gilleland, E. and Katz, R. W., 2011: New software to analyze how extremes change over time. *Eos*, **92(2)**, 1314.

Hall, T. M., and Yonekura, E., 2012: North-American Hurricane Landfall and SST: A Statistical Model Study, *submitted.*

Iman, R. L., Johnson, M. E., and Watson, C. C., 2005: Sensitivity analysis for computer model projections of hurricane losses. *Risk Analysis*, **25(5)**, 1277-1297.

Irish, J. L. and Resio, D. T., 2009: A hydrodynamics-based surge scale for hurricanes. *Ocean Engineering*, **37(1)**, 69-81.

Irish, J. L., Resio, D. T., and Ratcli, J. J., 2008: The influence of storm size on hurricane surge. *Journal of Physical Oceanography*, **38(9)**, 2003-2013.

Jaffee, D., Kunreuther, H., and Michel-Kerjan, E., 2008: Long term insurance for addressing catastrophe risk. *National Bureau of Economic Research Working Paper Series*, No.14210.

Jagger, T., Elsner, J., and Burch, R., 2010: Climate and solar signals in property damage losses from hurricanes a ecting the United States. *Natural Hazards*, **58(1)**, 541-557.

Jagger, T., Elsner, J., and Saunders, M., 2008: Forecasting U.S. insured hurricane losses. *Climate Extremes and Society*, H. Diaz and R. Murnane, eds., Cambridge University Press,189-208.

Jarrell, J., Hebert, P., and Mayeld, M., 1992: Hurricane experience levels of coastal county populations from Texas to Maine. *NOAA Tech. Memo*., NWS-NHC-46.

Jarvinen, B. R., Neumann, C. J., and Davis, M. A. S., 1984: A tropical cyclone data tape for the North Atlantic basin, 1886-1983, contents, limitations, and uses. *NOAA Tech. Memo.,* NWS NHC 22.

Katz, R., 2012: Economic impact of extreme events: An approach based on extreme value theory. *Extreme Events: Observations, Modeling and Economics*, J. U.-F. M. Ghil and M. Chavez, eds., American Geophysical Union. *In press*.

Katz, R. W., 2002: Stochastic modeling of hurricane damage. *Journal of Applied Meteorology*, **41(7)**, 754-762.

Klose, C. D., 2011: Evidence for higher tropical storm risks in Haiti due to increasing population density in hazard prone urban areas. *Environmental Research Letters*, **6(4)**, 044020.

Knutson, T., Sirutis, J., Garner, S., Vecchi, G., and Held, I., 2008: Simulated reduction in Atlantic hurricane frequency under twenty-first-century warming conditions. *Nature Geosci.*, **1**, 359–364.

Knutson, T. R., McBride, J. L., Chan, J., Emanuel, K., Holland, G., Landsea, C., Held, I., Kossin, J. P., Srivastava, A. K., and Sugi, M., 2010: Tropical cyclones and climate change. *Nature Geoscience*, **3(3)**, 157-163.

Landsea, C. W., 1993: A climatology of intense (or major) Atlantic hurricanes. *Monthly Weather Review*, **121(6)**, 1703-1713.

Lin, N. E., Vanmarcke, E., and Yau, S. C., 2010: Windborne debris risk analysis: Part II. Application in structural vulnerability modeling. *Wind and Structures*, **13**, 207-220.

Lonfat, M., Rogers, R., Marchok, T., and Marks, F. D., 2007: A parametric model for predicting hurricane landfall. *Monthly Weather Review*, **135(9)**, 3086-3097.

Maina, S. N., 2010: Developing a hurricane damage index. UCAR SOARS Summer Project.
Mendelsohn, R., Emanuel, K., and Chonabayashi, S., 2011: The impact of climate change on hurricane damages in the United States. *World Bank Policy Research Working Paper Series*, No. 5561.

Mendelsohn, R., Emanuel, K., Chonabayashi, S., and Bakkensen, L., 2012: The impact of climate change on global tropical cyclone damage. *Nature Climate Change***, 2(1)**, 1-5.

Munich Re, 2011: Significant natural catastrophes 1980 - 2011: 10 costliest events worldwide ordered by insured losses (NATCAT)., <http://www.munichre.com/en/reinsurance/business/non-life/default.aspx>.

Nakicenovic, N., Alcamo, J., and Davis, G., 2007. *IPCC Special Report on Emissions Scenarios (SRES)*. Cambridge University Press.

Neumayer, E. and Barthel, F., 2011: Normalizing economic loss from natural disasters: A global analysis. *Global Environmental Change*, **21(1)**, 13-24.

Nordhaus, W. D., 2010: The economics of hurricanes and implications of global warming. *Climate Change Economics*, **1(1)**, 1-20.

Peduzzi, P., Chatenoux, B., Dao, H., De Bono, A., Herold, C., Kossin, J., Mouton, F., and Nordbeck, O., 2012: Global trends in tropical cyclone risk. *Nature Climate Change*, **2(4)**, 289-294.

Pielke Jr., R. A., Gratz, J., Landsea, C., Collins, D., Saunders, M., and Musulin, R., 2008: Normalized hurricane damages in the United States: 1900-2005. *Natural Hazards Review*, **9(1**), 29.

Pielke Jr., R. A., Klein, R., and Sarewitz, D., 2000: Turning the big knob: Energy policy as a means to reduce weather impacts. *Energy and Environment*, **11(3)**, 255-276.

R Development Core Team, 2010: R: A Language and Environment for Statistical Computing. R Foundation for Statistical Computing, <http://www.r-project.org>.

Roeckner, E., Buml, G., Bonaventura, L., Brokopf, R., Esch, M., Giorgetta, M., Hagermann, S., Kirchner, I., Kornbleuh, L., Manzini, E., et al., 2003: The atmospheric general circulation model ECHAM5. *Max Planck Institute for Meteorology*, 349(DKRZ Tech. Report No. 6), 1-140.

Rogers, R., Marks, F. D., and Marchok, T., 2009: Tropical cyclone rainfall. *Encyclopedia of Hydrological Sciences.*

Sobel, A. H., I. M. Held, and C. S. Bretherton, 2002: The ENSO signal in tropical tropospheric temperature. *J. Climate*, **15,** 2702–2706.

Swanson, K. L., 2008: Nonlocality of Atlantic tropical cyclone intensities. *Geochem. Geophys. Geosyst.,* **9**, Q04V01.

Tuleya, R. E., DeMaria, M., and Kuligowski, R. J., 2007: Evaluation of GFDL and simple statistical model rainfall forecasts for U.S. landfalling tropical storms. *Weather and Forecasting*, **22(1)**, 56-70.

UNISDR, 2011: 2011 global assessment report on disaster risk reduction revealing risk, redefining development. *Development*.

van der Vink, G., Allen, R. M., Chapin, J., Crooks, M., Fraley, W., Krantz, J., Lavigne, A. M., LeCuyer, A., MacColl, E. K., Morgan, W. J., Ries, B., Robinson, E., Rodriguez, K.,Smith, M., and Sponberg, K., 1998: Why the United States is becoming more vulnerable to natural disasters. *Eos Trans*. *AGU*, **79(44)**, 533-537.

Vecchi, G. A., and Soden, B. J., 2007: Effect of remote sea surface temperature change on tropical cyclone potential intensity. *Nature*, **450**, 1066–1070.

Vecchi, G. A., Swanson, K. L., and Soden, B. J., 2008: Whither hurricane activity? *Science*, **322**, 687.

Villarini, G., G. A. Vecchi, T. R. Knutson, M. Zhao, and J. A. Smith, 2011: North Atlantic tropical storm frequency response to anthropogenic forcing: Projections and sources of uncertainty. *J.Climate*, **24(13)**, 3224-3238.

Chapter 5:

Conclusions and Future Work

5.1 Summary and Conclusions

Tropical cyclone (TC) landfall is one of the largest natural hazards on Earth that presents a threat every year, placing densely populated and increasingly developed coastal regions in harm's way. In this thesis, known physical relationships of TCs with climate have been modeled statistically to provide tools that link large-scale climate changes to the societally relevant quantities of TC landfall and economic damage risk. Two statistical modeling methods have been presented, a track model based on local regression and a damage index distribution, and together they can help provide a more complete picture of tropical cyclone risk assessment.

Each body chapter of this thesis is based on results published in, or submitted to, a peer-reviewed journal. The achievements and conclusions presented in each chapter of this thesis are summarized below.

Chapter 2

Construction of a statistical TC track model in the western North Pacific (WNP) using objectively defined averaging length scales for all components. This model provides a tool to connect different TC activity (e.g., frequency) to regional landfall risk. Further, the genesis component uses local Poisson regression to incorporate the dependence on ENSO state. This method successfully captures the known genesis region shift and projects the shift onto landfall rates along the coast. The model synthetic tracks are compared to observations to show that this model is able to simulate realistic TCs according to several diagnostics. (Yonekura and Hall 2011)

Chapter 3

Addition of further complexity into the WNP TC track model by including seasonally varying statistical predictors as well as ENSO dependence in the track propagation

component. We find that there are changes in tracks due to ENSO independent of changes in genesis, which impact regional landfall rates in China, Vietnam, Korea, and Japan. We confirm that ENSO has a statistically significant influence on landfall (Yonekura and Hall 2012).

The large advantage that our statistical model brings in comparison to observational studies of TC landfall is the increased resolution. For example, all the observed near misses are factored into the model construction, and with a large ensemble of stochastic tracks, there may be a track that makes landfall. Smoothing of observed landfall rates along the coast to minimize the noise could account for misses in the sense of missing one coastal segment and hitting one adjacent. However, it would not account of the observed TCs that pass by over the ocean. Further, when the analysis focuses down from climatological risk to risk at a specific ENSO state, our model has more advantages. All observational studies specify El Niño and La Niña events based on some threshold of ENSO index, however, our model is able to select a specific magnitude of ENSO event to look at separately. That aside, only looking at the observed landfalls for specific ENSO states further limits the data such that any smoothing to reduce noise along the coast would also smooth out the expected landfall rate variance from coastal geometry with respect to mean tracks and coastal proximity to high TC activity regions.

Chapter 4

Construction and application of a damage index that conveniently normalizes economic damage data from U.S. hurricane landfalls in a way that emphasizes the damage capacity of each TC, rather than the vulnerability of the landfall location. We show through

> extreme value analysis that the TC intensity and local bathymetric slope at landfall are important physical covariates in generalized Pareto distributions of damage. Then, in two separate analyses of synthetic TC tracks, we provide a framework for estimating extreme damage distributions that can be applied to future climate projections. (Chavas et al. 2012)

5.2 Future Work

In moving forward, there are ways that the tools I have used in this thesis may be improved and expanded upon. I have also found that there are many ways in which the methodologies in this thesis could be applied to other questions. Below I have listed some of these.

Adding components to the WNP track model

Intensity component in track model. The most important missing component to the current WNP TC track model is the storm intensity. The model cannot provide complete TC hazard analysis without TC intensity. In addition, ultimately intensity would be used to determine lysis using an intensity threshold, which is more consistent with the physical TC life cycle. My initial work on intensity proved it to be one of the more difficult components of a TC to model statistically. The difficulty in creating an intensity model is that it is a statistical model for climatological risk assessment, which means that climatological predictors are used as input, not operational (hourly) variables. Thus, it is difficult to create a model that matches well with the observations of TC intensity over a lifetime. The observations available to use as predictors are also limited. When looking at a climatological time scale, the predictors that are normally used in operational intensity models become less useful in explaining the variance in intensity evolution. The idea behind my current efforts is to take the important relationships from the operational

forecast models to inform the construction of a risk model. Two possible approaches are described here.

One approach is to use local regression step by step along a TC track to model 6-hourly V_{max} , increments in V_{max}, or V_{max}/MPI (where MPI is maximum potential intensity; Bister and Emanuel 1998). The use of MPI would provide physicality to the simulations. The independent variables tested for this model would be measures of persistence and the climate predictors used for the STIPS model (Statistical Typhoon Intensity Prediction Scheme; Knaff et al. 2005). Note that operational variables are not available in a risk model. All variables are obtained from the NCEP/NCAR Reanalysis (Kalnay et al. 1996) from 1949-2004, except for MPI, which will be calculated as in Bister and Emanuel (1998). Intensity will be determined right after the track model simulates the next storm location. The location will determine the values of predictors, and the local regression coefficients will be predetermined in a look-up table.

Another approach is to use time series resampling, where a time series from the set of historical V_{max} time series is randomly selected and assigned to a simulated track. The selection is weighted on similarities in location, track shape, time, and possibly climate state. If the number of 6-hourly points does not match exactly in the two tracks, the historical time series is stretched and interpolated to fit the synthetic track. This is the approach taken by Hall and Yonekura (2012).

Diagnostics will be performed on all of the models to determine which model has better skill. First, the spatial distribution of intensity over the entire basin, at landfall, seasonally, and at different ENSO states will be examined in comparison to observations. Second, intensity simulations over a historical TC track will be compared. Third, a cross-validation will be performed by constructing the intensity model on a set of observed years and then checking its

performance on the observations for the out-of-sample years. Once an intensity model is incorporated into the track model for the WNP, the track model can be used to examine climate effects on TC intensity.

Size component in track model. Modeling of the TC size (e.g., radius to maximum wind or largest closed isobar) is also crucial for hazard modeling, as it determines the coastal area affected by high winds and rainfall. In addition, having a measure of TC size will provide a better idea of what coastal areas are affected by near misses, where the storm center does not actually cross over land. There is a decade of outer radius and radius of vanishing winds data for the WNP and NA from QuikSCAT that can be analyzed to build the size component (Chavas and Emanuel 2010). As there is little change in radius of vanishing winds throughout a TC's lifetime, it would be set at or shortly after genesis based on predictors such as potential intensity. Then, the variation for the remainder of the track would follow according to observed TC lifetime radius variations. There is also radius of maximum winds data in the IBTrACS database, which can be used to create a regression model including TC intensity as a predictor.

Other hazard components. Aside from intensity in terms of maximum wind speed, there are several other hazards that TCs pose at landfall that can also be modeled. Chief among them are storm surge and rainfall. For landfalls on specific regions of interest, the storm surge that would occur for a set of stochastic TC tracks can be modeled using either the SLOSH (Sea, Lake, and Overland Surges from Hurricanes) or ADCIRC (Advanced Circulation hydrodynamic model; Luettich and Westerink 2004) models. In this way, a spectrum of the possible storm surge outcomes can be evaluated. This is similar to the work performed by Lin et al. (2010).

Rainfall may also be modeled. Rainfall data from TCs has been extracted (Lonfat et al. 2004) from the Tropical Rainfall Measuring Mission (TRMM; Simpson et al. 1988) Microwave

Imager (Kummerow et al. 1996), and this type of data could be used to construct a statistical rainfall model along the tracks with predictors such as storm size, intensity, and location. Alternatively, rainfall could be modeled just over land with respect to TC location and other TC characteristics such as size and intensity. For example, Lee et al. (2006) used weather station rain data to create a pdf of possible rainfall given a TC in at a given proximity to each weather station, and they can use this to make stochastic simulations of rainfall for nearing or landfalling TCs.

Another further direction to pursue would be to model the economic damage. If TC winds and storm surge can be simulated separately, they can be used as input for a damage model such as the FEMA HAZUS-MH MR3 model (Klima et al. 2011). The output is in the form of damages and aggregate total losses. A range of different landfalling TCs can be input into this model to calculate the range of resulting damage possibilities. This type of modeling in the North Atlantic especially could be used to compare to the Damage Index GPD modeling that we performed in Chapter 4.

Further analyses

Examine influence of other predictors. Other predictors and covariates are worth using in both the statistical track model and the GPD models. For the former, it could prove useful to condition components of the WNP model on other large-scale climate variables such as SST and relative SST. This would allow a similar investigation of how these predictors affect TC tracks and landfall risk. Further, it would allow for input from GCMs that simulate these variables for past, current, and future climates. TC simulations using these inputs could provide a landfall risk assessment for these different times. With regard to the GPD models, there are other damage-

causing predictors that could be tested for their usefulness, including storm translational speed, angle of storm track with respect to the coast, and storm size. For the latter, we have already experienced data limitations, however it may be worth further examination.

Infer landfall risk from ENSO projections and reconstructions. Both modeling and paleoclimate reconstructions have been used to reconstruct past ENSO behavior, and many models have simulated future climate scenarios that include ENSO. Our WNP track model could then be used to infer TC behavior and landfall risk in past and future climates given the respective ENSO state. This could be used to compare to any paleotempestological efforts or recorded storm records for East Asian regions from the past millennia as well as make predictions of future TCs.

Expand extreme value analysis. In order to make a full assessment of future hurricane damage in the U.S., we plan to expand our analysis using the different GCM projections from the CMIP5 models. The statistical-deterministic hurricane model will then be run for a set number of years (on the order of hundreds to thousands) for each model's current and future climates, and the resulting landfalls will be analyzed using our GPD model of Damage Index. This will allow for us to account for projected changes in hurricane frequency as well as changes in storm characteristics at landfall across a fuller range of models. In addition, if data on the changes in economic value along the U.S. coast can be acquired, the analysis can then convert from Damage Index to actual monetary units.

Comparison of track models. There are now a number of different models that are being used to simulate TC tracks in large ensembles in order to make some type of risk assessment, for example, the two hurricane models used in Chapter 4. In moving forward, an in-depth comparison of their skill would be useful to pinpoint the strengths and weaknesses of each. This

would entail a careful analysis of diagnostics that evaluate modeled tracks against observations (similar to the model diagnostics of Chapter 2) as well as weighing attributes such as utility in answering specific questions and accessibility for public interpretations. Once the comparison is performed, multiple modeling methods can more strategically implemented in concert, and new modeling methods that combine each model's strengths can be used.

References

Bister, M. and K. A. Emanuel, 1998: Dissipative heating and hurricane intensity. *Meteorol. Atmos. Phys.*, **50**, 233-240.

Chavas, D. R., and K. A. Emanuel, 2010: A QuikSCAT climatology of tropical cyclone size. *Geophys. Res. Lett.*, **37**, L18816.

Chavas, D. R., E. Yonekura, C. Karamperidou, N. Cavanaugh, K. Serafin, 2012: US Hurricanes and economic damage: an extreme value perspective. *Natural Hazards Review*, *in press.*

Hall, T. M. and E. Yonekura, 2012: North-American Hurricane Landfall and SST: A Statistical Model Study*, submitted.*

Kalnay, E. et al., 1996: The NCEP/NCAR 40-Year Reanalysis Project. *Bull. Amer. Meteor. Soc.*, **77**, 437-471.

Klima, K., N. Lin, K.A. Emanuel, M.G. Morgan, and I. Grossmann, 2011: Hurricane modification and adaptation in Miami-Dade County, Florida. *Environmental Science and Technology*, **45**, 636-642.

Knaff, J. A., C. R. Sampson, and M. DeMaria, 2005: An Operational Statistical Typhoon Intensity Prediction Scheme for the Western North Pacific. *Wea. Forecasting*, **20**, 688–699.

Kummerow, C., W. S. Olson, and L. Giglio, 1996: A simplified scheme for obtaining precipitation and vertical hydrometeor profiles from passive microwave sensors. *IEEE Trans. Geosci. Remote Sens*, **34,** 1213–1232.

Lee, C.-S., L.-R. Huang, H.-S. Shen, and S.-T. Wang, 2006: A climatology model for forecasting typhoon rainfall in Taiwan. *Natural Hazards*, **37**, 87-105.

Lin, N., K.A. Emanuel, J.A. Smith, and E. Vanmarcke, 2010: Risk assessment of hurricane storm surge for New York City. *Journal of Geophysical Research-Atmospheres*, **115**, D18121.

Lonfat, M., F. D. Marks, and S. S. Chen, 2004: Precipitation Distribution in Tropical Cyclones Using the Tropical Rainfall Measuring Mission (TRMM) Microwave Imager: A Global Perspective. *Mon. Wea. Rev.*, **132**, 1645–1660.

Luettich, R.A., Jr. and J.J. Westerink, 2004: Formulation and numerical implementation of the 2D/3D ADCIRC finite element model version 44.xx. <www .adcirc.org>.

Multi-hazard Loss Estimation Methodology Hurricane Model, HAZUS-MH MR3 Technical Manual; Department of Homeland Security, Federal Emergency Management Agency, Hardening Division: Washington, DC, 2009.

Simpson, J., R. F. Adler, and G. R. North, 1988: Proposed tropical rainfall measuring mission (TRMM) satellite. *Bull. Amer. Meteor. Soc*, **69,** 278–295.

Yonekura, E. and T.M. Hall, 2011: A statistical model of tropical cyclone tracks in the western North Pacific with ENSO-dependent cyclogenesis. *J. Appl. Meteor. Climatol.*, **50**, 1725-1739.

Yonekura, E. and T.M. Hall, 2012: ENSO effects on tropical cyclone tracks and genesis in the western North Pacific, *submitted.*